RIJKSUNIVERSITEIT GRONINGEN

Size effects in cellular solids

Proefschrift

ter verkrijging van het doctoraat in de
Wiskunde en Natuurwetenschappen
aan de Rijksuniversiteit Groningen
op gezag van de
Rector Magnificus, dr. F. Zwarts,
in het openbaar te verdedigen op
vrijdag 5 januari 2007
om 16:15 uur

door

Cihan Tekoğlu

geboren op 17 januari 1976
te Ankara, Turkije

Promotor:	Prof. dr. ir. E. van der Giessen
Copromotor:	Prof. dr. ir. P. R. Onck
Beoordelingscommissie:	Prof. dr. ir. M. G. D. Geers Prof. dr. ir. F. van Keulen Prof. dr. S. Forest

Size effects in cellular solids

Cihan Tekoğlu

Netherlands Institute
for Metals Research

This research was carried out under project number 01EMM02 as part of the FOM ("Stichting voor Fundamenteel Onderzoek der Materie", which is financially supported by "Nederlandse Organisatie voor Wetenschappelijk Onderzoek (NOW)") / NIMR (the Netherlands Institute for Metals Research) programme entitled "Evolution of the microstructure of materials".

MSC PhD thesis series 2007-02
ISSN 1570-1530
ISBN 90-367-2897-5

Contents

1

Introduction

When modern man builds large load-bearing structures, he uses dense solids; steel, concrete, glass. When nature does the same, she generally uses cellular materials; wood, bone, coral. There must be good reasons for it.

M .F. Ashby

1.1 Cellular solids

Natural materials, such as wood, cork and cancellous bone, and man-made materials such as metal honeycombs and foams, are well-known examples of cellular solids. Common to all of them is a microstructure consisting of an interconnected network of struts (open cells) or plates (closed cells). Figure 1.1.a-c show three examples of cellular solids, namely, a hexagonal honeycomb, an open and a closed cell foam, respectively.

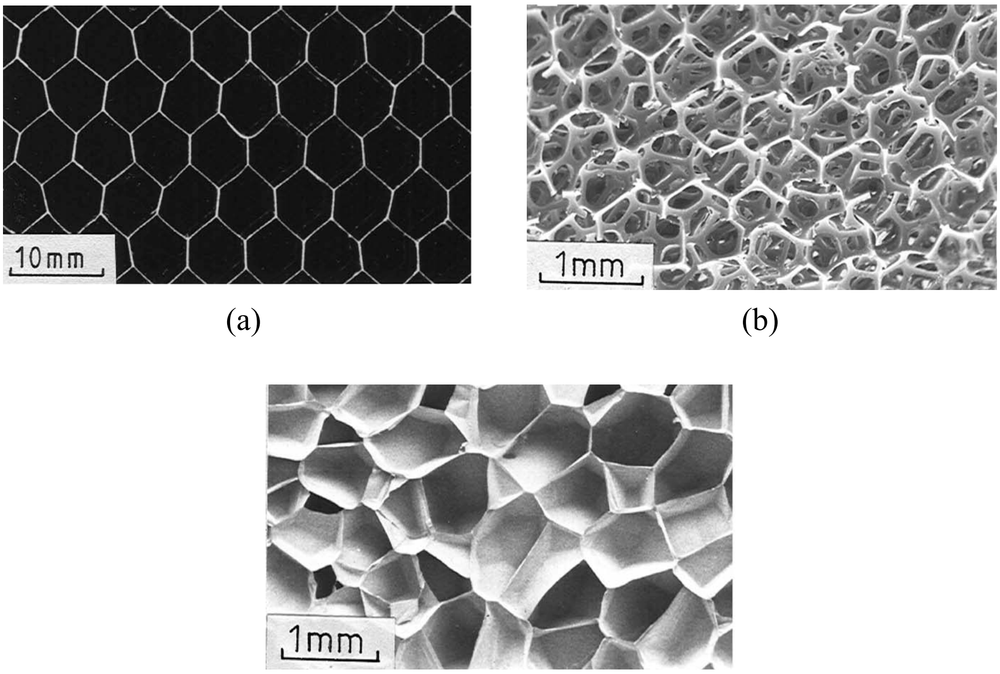

(a) (b)

(c)

Figure 1.1: Examples of cellular solids: (a) Aluminium honeycomb. (b) Open cell polyurethane foam. (c) Closed cell polyethylene foam. (Reproduced, with permission, from Gibson and Ashby [1997]).

Theoretical attempts to understand the geometry and the fundamental principles of the mechanics of cellular solids dates back to the celebrated geometrician Leonard Euler (see De Boor [1998]). Since then, a large literature developed on the geometric, mechanical, thermal and electrical characteristics of these solids. An extensive record on the structure and the properties of cellular solids is given by Gibson and Ashby [1997]. In this thesis, we focus on the mechanics of metal honeycombs and foams, yet, most of our conclusions are applicable to other cellular solids as well.

The high specific bending stiffness is an important structural property, which, among others, has made metal foams a competitive engineering material in the last decades. They are often used in sandwich panels, where they are laminated between two dense solids to increase the moment of inertia, owing to their low density and good shear and fracture strength. Their damping capacity is up to 10 times that of the solid metals, and they have exceptional ability to absorb energy at almost constant strain, which makes them attractive for impact absorption systems. Open cell foams, with a large accessible surface area, have a very good heat transfer ability. A more extensive list of multifunctional features and application areas for a number of commercially available metal foams are given by Ashby *et al.* [2000]. Metal foams have already a profitable market, which is growing rapidly due to the improvements in the production technology and engineering design.

1.2 Objective

The mechanical properties of metal foams (and other cellular solids) depend on the properties of the metal that they are made from, on their relative density, and on the cell topology (i.e., cell size, cell shape, open or closed cell morphology, etc.). The cell size of commercially available metal foams is about 1 to 10 mm. This is on the order of the smallest structural length of specimens in many applications. In such cases, the individual response to a load differs significantly from one cell to another, and the fundamental assumption of the classical continuum theory that the (physical, chemical, mechanical, etc.) properties of a material are uniformly distributed throughout its volume fails. Another situation where the classical continuum theory loses its accuracy is when the characteristic wavelength of loading is comparable to the cell size. An important technological consequence of this is the occurrence of size effects. The term "size effect" designates the effect of the macroscopic (sample) size, relative to the cell size, on the mechanical behaviour. In the last decade evidence of this appeared in a number of experimental studies (see section 1.4). To theoretically account for size effects, one may take the cellular morphology into account by discretely modelling each cell wall and/or cell face. This allows for an accurate representation of the microstructural deformation mechanisms, the bending and stretching of cell walls and faces. Such a microstructural model can predict how the overall (macroscopic) response is related to the microstructural parameters. In view of size effects, the most important feature is that it incorporates, in a physically sound manner, the material length scale in the problem, i.e. the cell size. However, such a discrete model can become computationally expensive for complex (random) microstructures, especially in three dimensions. Another approach is to use a generalized continuum theory in which many microstructural details are averaged out, but in which a "characteristic" length scale is retained. The goal of this thesis is twofold:

1) To explore the microstructural mechanisms that are responsible for the size-dependent elastic behaviour of cellular solids by using a discrete microstructural model.

2) To assess the capability of generalized continuum theories to capture size effects through a careful comparison with the discrete simulations.

In section 1.3, we give a historical overview of generalized continuum theories. We discuss two of them in more detail, Eringen's micropolar theory and Toupin-Mindlin's strain gradient elasticity. In section 1.4, we summarize the experimental work performed to detect the size effects in the mechanics of cellular solids. Finally, in section 1.5, we outline the contents of this thesis.

1.3 Generalized continuum theories: a historical overview

A natural generalization of the classical continuum theory is to model the interaction between two material points, not only via a force vector, but also via a couple vector. The origin of this evolution can be traced back to the early Euler-Bernoulli beam theory, where the displacement and the rotation vectors are independent kinematic quantities, and the usual force tractions and couples are independent internal loads. The idea of having independent couple-stresses in an elastic continuum is further explored by several scientists in the 18'th century (MacCullagh (1839), Lord Kelvin (1882, 1884, 1890), Voigt (1887))[1]. In 1909, E. and F. Cosserat (the Cosserat brothers) developed a (non-linear) theory of elasticity for bars, surfaces and bodies; they introduced a "rigid triad" at every material point of the continuum, which can rotate independently from the local rotation of the medium in the course of deformation (Cosserat and Cosserat [1909]). By this way, a "Cosserat continuum" fully accounts for the effects of couple stresses in the deformation of an elastic continuum. In their work, however, the Cosserat brothers did not give any specific constitutive relations.

The work of the Cosserat brothers did not get the attention it deserved for a long time. In the early 1960s, the subject of the theory of elasticity with couple stresses is reopened and Cosserat-type theories are discussed independently by several authors. Among them, Grioli [1960], Rajagopal [1960], Truesdell and Toupin [1960], Aero and Kuvshinskii [1961], Eringen [1962], Mindlin and Tiersten [1962] and Koiter [1964] investigated a special case of the Cosserat continuum theory where the rotation of the rigid Cosserat triad is not an independent kinematic variable but is defined in the usual sense as given in classical elasticity and fluid dynamics. In the

---

[1] See Cosserat and Cosserat [1909] and the references therein.

literature, this theory is referred to with a variety of names, such as, “Cosserat theory with constrained rotation” (e.g. Toupin [1964]), “Couple stress theory” (e.g. Koiter [1964]), “Indeterminate couple stress theory” (e.g. Eringen [1968]), “Cosserat pseudo-continuum” (e.g. Nowacki [1986]), or simply as “Cosserat theory” (e.g. Mora and Waas [2000]). In the following, we will refer to it as the couple stress theory (see Table 1.1). In the couple stress theory, only the gradient of the rotation vector enters into the strain energy density function, that is, eight of the eighteen components of the first gradient of strain. Subsequently, all the components of the first gradient of the strain were introduced into the strain energy density function, in a non-linear form, by Toupin [1962, 1964]). This theory is referred to as the “strain gradient theory” in the literature. The linear version of the strain gradient theory was given by Mindlin [1964]. Green and Rivlin [1964] established the basis of a very general case including all higher-order gradients of the strain, referred to as the “multipolar” theory. Mindlin [1965] derived a theory where both the first and the second gradient of the strain are taken into account, termed the second strain gradient theory, which is a special case of the multipolar theory. All these theories, associating energy to the spatial gradients of strain, are referred to in the literature as “higher grade theories” (see Table 1.1).

Another way of extending classical elasticity to include the effects of the deformations of the underlying microstructure is by inserting new degrees of freedom into the continuum. These degrees of freedom are specified to be independent from the usual displacement degrees of freedom. These kinds of theories can be referred to as “higher order theories” (see Table 1.1). The (non-linear) micromorphic theory, introduced by Eringen and Şuhubi [1964], and the (linear) micro-structure theory of Mindlin [1964] fall into this category. The linear form of the micromorphic theory (see Eringen [1999]) coincides with the micro-structure theory of Mindlin. In the micromorphic theory, a material point possesses three deformable directors that introduce nine additional degrees of freedom, ψ_{ij}, which are strain-like dimensionless quantities. This corresponds to a “micro-element” embedded in the continuum that can rotate and deform independently from the local deformation of the “macro-element” (material particle), in the language of Mindlin. Two special cases of the micromorphic theory are the microstretch (Eringen [1971, 1990]) and the micropolar (Eringen [1965, 1966]) theories. In the microstretch continuum, there are four additional degrees of freedom: three for the rotation (ϕ_i) and one for the stretch (χ) of the directors. In the case of the micropolar continuum, the directors are rigid and there are only three rotational degrees of freedom (ϕ_i) in addition to the three classical displacement degrees of freedom. If the directors are taken to be fully coupled to the material point, the rotational degrees of freedom of the micropolar theory become equal to the classical rotations, $\phi_k = \in_{ijk} u_{j,i}/2$, and the micropolar theory reduces to the couple stress theory. As can be observed from Table 1.1, the couple stress theory is a special case of strain gradient theory as well. Another connection between the higher order and higher grade theories is that the micromorphic theory reduces to the strain gradient theory if ψ_{ij} are defined to be equal to the gradient of displacement $u_{i,j}$, for which case the micro-medium merges with the macro-medium.

In the last few decades, a huge literature has been built up on the topic of generalized media, including elasto-plastic higher order/grade continuum theories (see e.g., Aifantis [1987], Fleck and Hutchinson [1993, 1997, 2001], Forest and Sievert [2006], etc.). The references listed here are by no means complete, but they point out the main directions followed in the field of generalized continuum theories. Table 1.1 summarizes (some of) the higher order/grade continuum theories and the contacts among them. Starting point for the higher order and the higher grade theories in this thesis are Eringen's micropolar theory and Toupin-Mindlin's strain gradient elasticity. Therefore, we will briefly state the fundamentals of these theories in the following subsections.

1.3.1 Theory of micropolar elasticity

In this section we will review the fundamental equations of the linear micropolar continuum. For a more general account of the theory, the reader is referred to Eringen [1999]. Note that the names micropolar theory and Cosserat theory are used interchangeably by many authors in the literature.

The kinematic description of the micropolar theory includes the microrotations ϕ_i as independent degrees of freedom in addition to the usual displacements u_i (see Table 1.1). Consequently, the transfer of loading between neighbouring material points is achieved both through the couple stresses m_{ij} and the classical Cauchy stresses σ_{ij}. In the absence of body forces and body couples, the equilibrium equations of the micropolar theory are given as

$$\begin{aligned} &\sigma_{ji,j} = 0, \\ &m_{ji,j} + \in_{ijk} \sigma_{jk} = 0, \end{aligned} \tag{1.1}$$

where $\in_{ijk}$ is the antisymmetric Levi-Civita permutation tensor. Equation (1.1) implies that the Cauchy stress tensor σ_{ij} is not necessarily symmetric and its antisymmetric part is determined by the divergence of the couple stress tensor m_{ij}. The principal of virtual work reads

$$\int_V (\sigma_{ij}\delta\gamma_{ij} + m_{ij}\delta k_{ij})\, \mathrm{d}V = \int_S (t_i\delta u_i + Q_i\delta\phi_i)\, \mathrm{d}S, \tag{1.2}$$

where t_i is the surface traction, and Q_i is the surface couple. The boundary conditions to be specified on the bounding surface S of a micropolar solid are

Table 1.1

Higher order/grade continuum theories and the contacts among them.

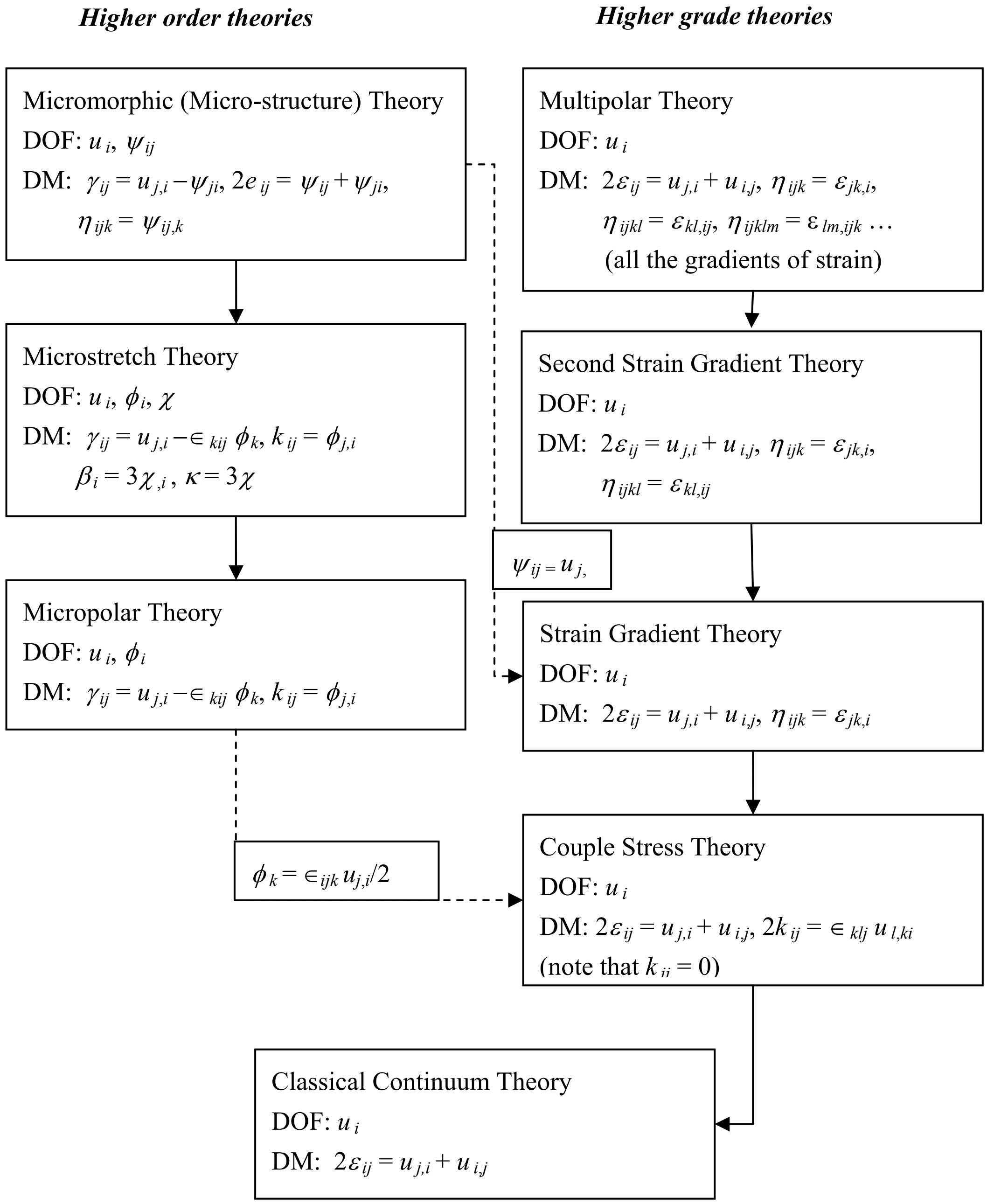

DOF: degree of freedom, DM: deformation measure,

ψ_{ij}: degree of freedom tensor for the deformable triad (micro-element),

u_i: displacement vector, ϕ_i: rotation vector for the rigid triad

$$\begin{aligned} n_j\sigma_{ji} &= t_i^* \text{ or } u_i = u_i^*, \\ n_j m_{ji} &= Q_i^* \text{ or } \phi_i = \phi_i^*, \end{aligned} \tag{1.3}$$

where n_j is the unit outward normal to the surface S, and * denotes a prescribed quantity on the surface. The (small) strain tensor γ_{ij} and the curvature tensor k_{ij} are defined as

$$\begin{aligned} \gamma_{ij} &= u_{j,i} - \in_{kij} \phi_k, \\ k_{ij} &= \phi_{j,i}. \end{aligned} \tag{1.4}$$

We can decompose the Cauchy stresses and strains into their symmetric and antisymmetric parts

$$\sigma_{ij} = s_{ij} + \tau_{ij} \text{ and } \gamma_{ij} = \varepsilon_{ij} + \beta_{ij}, \tag{1.5}$$

where

$$\varepsilon_{ij} = \frac{1}{2}(\gamma_{ij} + \gamma_{ji}) = \frac{1}{2}(u_{j,i} + u_{i,j}) \text{ and } \beta_{ij} = \frac{1}{2}(\gamma_{ij} - \gamma_{ji}) = \in_{ijk}(\omega_k - \phi_k). \tag{1.6}$$

Note that the antisymmetric part of the strain β_{ij} is related to the difference between the classical macrorotations $\omega_k = (\in_{ijk} u_{j,i})/2$ and the microrotations ϕ_k.

For a linear elastic, anisotropic micropolar solid, a strain energy density function (i.e. including only the quadratic terms in the kinematic variables) can be given as

$$w(\gamma_{ij}, k_{ij}) = \frac{1}{2} C_{ijkl}\gamma_{ij}\gamma_{kl} + B_{ijkl}\gamma_{ij}k_{kl} + \frac{1}{2} D_{ijkl}k_{ij}k_{kl}. \tag{1.7}$$

In (1.7) the linear terms in γ_{ij} and k_{ij} are omitted to have zero stress in the undeformed state. Note that k_{ij} is a pseudo-tensor (i.e., a tensor whose components reverse sign under an inversion of the coordinate system); to be able to have an objective strain energy density w, the tensor B_{ijkl} must be a pseudo-tensor as well. The independence of the stiffness coefficients of a medium with respect to an inversion of the coordinate system is called *central symmetry*, in which case B_{ijkl} vanish and the constitutive equations read

$$\begin{aligned} \sigma_{ij} &= \frac{\partial w}{\partial \gamma_{ij}} = C_{ijkl}\gamma_{kl}, \\ m_{ij} &= \frac{\partial w}{\partial k_{ij}} = D_{ijkl}k_{kl}, \end{aligned} \tag{1.8}$$

where the fourth order stiffness tensors C_{ijkl} and D_{ijkl} possess the symmetries

$$C_{ijkl} = C_{klij} \text{ and } D_{ijkl} = D_{klij}. \tag{1.9}$$

For the case of an isotropic material, C_{ijkl} and D_{ijkl} are isotropic tensors, and the constitutive equations read (see e.g. Nowacki [1986])

$$\begin{aligned} \sigma_{ij} &= \frac{\partial w}{\partial \gamma_{ij}} = (\mu+\alpha)\gamma_{ij} + (\mu-\alpha)\gamma_{ji} + \lambda\gamma_{kk}\delta_{ij}, \\ m_{ij} &= \frac{\partial w}{\partial k_{ij}} = (\xi+\upsilon)k_{ij} + (\xi-\upsilon)k_{ji} + \rho k_{kk}\delta_{ij}, \end{aligned} \tag{1.10}$$

where δ_{ij} is the Kronecker-delta. Equation (1.10) shows that the micropolar theory has four new constants, α, ξ, υ, and ρ in addition to the classical Lamé constants, λ and μ. The requirement of positive definiteness of the strain energy density places some restrictions on the micropolar constants:

$$\begin{aligned} &\mu > 0, \quad 3\lambda + 2\mu > 0, \quad \xi > 0, \quad 3\rho + 2\xi > 0, \\ &\mu + \alpha > 0, \quad \xi + \upsilon > 0, \quad \alpha > 0, \quad \upsilon > 0. \end{aligned} \tag{1.11}$$

If the microrotations ϕ_i are constrained to be equal to the macrorotations ω_i, the micropolar theory reduces to the couple stress theory. This corresponds to the case $\alpha \to \infty$, for which the antisymmetric part of the strain tensor, β_{ij}, and the spherical part of the curvature tensor, k_{ii}, go to zero. Consequently, the antisymmetric part of the Cauchy stress, τ_{ij}, and the first invariant of the couple stress, m_{kk}, disappear from the virtual work principle, as well as from the constitutive equations:

$$\begin{aligned} s_{ij} &= \lambda\varepsilon_{kk}\delta_{ij} + 2\mu\varepsilon_{ij}, \\ m_{ij} &= (\xi+\upsilon)k_{ij} + (\xi-\upsilon)k_{ji}. \end{aligned} \tag{1.12}$$

The first invariant of the couple stress, m_{kk}, remains indeterminate in the theory, and it is taken to be equal to zero (see Koiter [1964]). The antisymmetric part of the Cauchy stress, τ_{ij}, can still be obtained from the equilibrium equations (see Eq. 1.1). For a discussion of the couple stress theory, the reader is referred to Koiter [1964].

1.3.2 Strain gradient elasticity

In this section we will review the fundamental equations of the strain gradient elasticity. For a more general account of the theory, the reader is referred to Mindlin [1964].

The kinematic variables in the strain gradient elasticity theory are given as

$$\begin{aligned} \varepsilon_{ij} &= \frac{1}{2}(u_{j,i} + u_{i,j}) = \text{strain tensor}, \\ \eta_{ijk} &= \varepsilon_{jk,i} = \eta_{ikj} = \text{strain gradient tensor.} \end{aligned} \tag{1.13}$$

The strain energy density function, for a linear elastic, isotropic strain gradient material with central symmetry can be written as

$$\begin{aligned} w(\varepsilon_{ij}, \eta_{ijk}) = \frac{\lambda}{2}\, \varepsilon_{ii}\varepsilon_{jj} + \mu\varepsilon_{ij}\varepsilon_{ij} + a_1\eta_{iik}\eta_{kjj} + a_2\eta_{ijj}\eta_{ikk} \\ + a_3\eta_{iik}\eta_{jjk} + a_4\eta_{ijk}\eta_{ijk} + a_5\eta_{ijk}\eta_{kji}. \end{aligned} \tag{1.14}$$

Note that the eighteen additional kinematic variables in the strain energy density function, η_{ijk}, can be defined in three different forms: I, the eighteen components of the second gradient of displacement; II, the eighteen components of the first gradient of strain; III, the eight components of the first gradient of the rotation and the ten components of the fully symmetric part of the second gradient of the displacement (or of the gradient of the strain) as shown by Mindlin [1964]. The one that we show here corresponds to the second form.

The constitutive equations (for the second form) are given as

$$\begin{aligned} \sigma_{ij} &= \frac{\partial w}{\partial \varepsilon_{ij}} = \lambda\varepsilon_{kk}\delta_{ij} + 2\mu\varepsilon_{ij}, \\ \tau_{ijk} &= \frac{\partial w}{\partial \eta_{ijk}} = \frac{1}{2}\, a_1(\delta_{ij}\eta_{kpp} + 2\delta_{jk}\eta_{ppi} + \delta_{ki}\eta_{jpp}) + 2a_2\delta_{jk}\eta_{ipp} \\ &\quad + a_3(\delta_{ij}\eta_{ppk} + \delta_{ik}\eta_{ppj}) + 2a_4\eta_{ijk} + a_5(\eta_{kij} + \eta_{jki}). \end{aligned} \tag{1.15}$$

In (1.15) the constants a_1 to a_5 are new material parameters with dimensions of force, σ_{ij} are the classical Cauchy stresses and τ_{ijk} are the so-called double stresses, with dimensions force per unit length. The positive definiteness of the strain energy density requires (see Mindlin and Eshel [1968])

$$\begin{aligned} &\mu > 0, \quad 3\lambda + 2\mu > 0, \quad -\bar{d}_1 < \bar{d}_2 < \bar{d}_1, \quad \bar{a}_2 > 0, \\ &5\bar{a}_1 + 2\bar{a}_2 > 0, \quad 5\bar{f}^2 < 6(\bar{d}_1 - \bar{d}_2)(5\bar{a}_1 + 2\bar{a}_2), \end{aligned} \tag{1.16}$$

where

$$\begin{aligned} &18\bar{d}_1 = -2a_1 + 4a_2 + a_3 + 6a_4 - 3a_5, \\ &18\bar{d}_2 = 2a_1 - 4a_2 - a_3, \quad 3\bar{a}_1 = 2(a_1 + a_2 + a_3), \\ &\bar{a}_2 = a_4 + a_5, \quad 3\bar{f} = a_1 + 4a_2 - 2a_3. \end{aligned} \tag{1.17}$$

The principal of virtual work for a volume V bounded by a smooth surface S, in the absence of body forces, reads

$$\int_V (\sigma_{ij}\delta\varepsilon_{ij} + \tau_{ijk}\delta\eta_{ijk})\,\mathrm{d}V = \int_S (t_j \delta u_j + r_j \delta D u_j)\, d\mathrm{S}, \tag{1.18}$$

where t_j and r_j are the surface traction and the surface double traction, respectively, on the surface S. The equilibrium equations and the boundary conditions are

$$\sigma_{jk,j} - \tau_{ijk,ij} = 0, \tag{1.19}$$

and

$$\begin{aligned} &n_j(\sigma_{jk} - \tau_{ijk,i}) - D_j(n_i\tau_{ijk}) + (D_l n_l) n_i n_j \tau_{ijk} = t_k^* \ \text{ or } \ u_k = u_k^*, \\ &n_i n_j \tau_{ijk} = r_k^* \ \text{ or } \ Du_k = Du_k^*, \end{aligned} \tag{1.20}$$

where n_j is the unit outward normal to the surface S. For a certain combination of the higher grade material constants, the strain gradient theory reduces to the couple stress theory:

$$\begin{aligned} &a_1 \to \xi - \upsilon, \quad a_2 \to -\frac{\xi - \upsilon}{2}, \quad a_3 \to -\frac{\xi - \upsilon}{2}, \\ &a_4 \to \xi, \quad a_5 \to -\xi. \end{aligned} \tag{1.21}$$

1.4 A brief summary of experiments on size effects

A considerable amount of experiments have been performed to capture the size effects in the mechanical behaviour of cellular solids. In this section, we will visit some of these studies, which establish the experimental basis and an important motivation for this thesis.

The first experiments associated with size effects, to the knowledge of the author, were performed in the mid 1960s to obtain the couple stress constants of conventional engineering dense solids, such as aluminium and steel. Schijve [1966] measured the bending rigidity of aluminium sheets, but could not observe any size effects, as opposed to the couple stress theory which predicts an enhanced bending rigidity with decreasing plate thickness. Similarly, Ellis and Smith [1967] conducted bending tests on aluminium and low-carbon steel sheets, and they did not reveal any couple stress effects. They concluded that couple stress effects would be active only for much smaller sample sizes, where the plate thickness is approximately equal to the grain size. Then, experiments on micro-featured materials (such as reinforced composites) were conducted, which are expected to show higher-order effects for larger samples due to the larger microstructural length scales. Gauthier and Jahsman [1975] developed a novel composite material to measure its micropolar elastic constants. The composite consisted of an epoxy matrix reinforced by uniformly distributed aluminium shots, with a Young's modulus 20 times that of the matrix. The much stiffer aluminium shots represented rigid microelements embedded in a deformable medium (i.e. the epoxy matrix). They performed torsion tests on circular cylindrical samples, but the samples behaved according to the classical theory. They concluded: "Possible micropolar behaviour is masked by material property variations (from one sample to another with a different size) due to inhomogeneity". Gauthier [1982], however, was able to fit the wave propagation experiments on the same reinforced composite by using micropolar theory, with a characteristic length very close to the radius of the aluminium shots, 0.7 mm. Lakes and co-authors performed several experiments on different micro-featured solids, such as human bones. Yang and Lakes [1981], conducted quasi-static torsion tests on circular cylindrical compact bones, and showed that the couple stress theory can capture the enhancement in torsional rigidity with decreasing sample radius. They found the couple stress characteristic length to be around 0.15-0.25 mm, which is comparable to the diameter of the major structural element in compact bones, the osteon.

The early experiments on cellular solids to observe the dependence of the macroscopic material properties on the specimen size dates back to the 1980's. Lakes [1983, 1986] measured the bending and torsional rigidities of two polymeric foams and a syntactic foam, as a function of diameter. He concluded that the micropolar elasticity is a suitable model to pick-up the enhanced bending and torsional rigidities with decreasing diameter of the polymeric foams, whereas the syntactic foam behaves as a classical solid. Opposed to these results, however, some others indicated a decreasing bending and torsional stiffness/strength with decreasing sample size. For example, Brezny and Green [1990] measured the Young's modulus and the bending strength (by three-point bending experiments) of a reticulated vitreous carbon foam consisting of relatively isotropic open cells, and found that both the modulus and the strength of this material decrease dramatically with decreasing specimen size. The weakening effects in both bending and torsion were detected for closed cell polymethacrylimide foam and open cell copper foam as well (Anderson *et al.* [1994], Anderson and Lakes [1994]).

Size effects in foams under uniaxial compression are also experimentally investigated. Bastawros *et al.* [1999] measured the Young's modulus and the compressive strength of closed cell Alporas aluminium foam, by changing the area under compression while keeping the length of the samples in the compression direction constant. Andrews *et al.* [2001], on the other hand, conducted uniaxial compression tests on square prisms of both closed cell Alporas and open cell Duocel foams, where the samples had identical geometry but different absolute size. Both sets of experiments, similar to the observations of Brezny and Green, showed that the Young's modulus and the compressive strength of the samples decrease dramatically with decreasing specimen size. The common conclusion to all of these studies showing a weakening in the (bending, torsional or compressive) stiffness and strength was that these size effects are actually "edge effects". The edge effects were related to an incomplete cell layer located at the surface of the specimens, which is included in the total specimen volume but contribute very little to the mechanical properties. Surface damage introduced by cutting or machining of specimens enhances these edge effects. Anderson and Lakes [1994] argued that the edge effects and the micropolar effects are usually both present and it is possible to observe weakening or strengthening behaviour depending on which one is more dominant.

Shear experiments on metal foams were also reported. These studies indicated an enhanced shear strength with decreasing sample thickness (e.g. Andrews *et al.* [2001], Chen *et al.* [2002]). In these experiments, the shear load is applied through face sheets that are perfectly bonded to the metal foam. As a result, the surface cells that are perfectly bonded to the top and the bottom face sheets are much more constrained compared to those located in the bulk. This gives rise to a gradient in deformation, so that "strong" boundary layers are formed adjacent to the face sheets; the volume fraction of these boundary layers increase with decreasing thickness and it leads to a higher shear strength. Kesler and Gibson [2002], conducted three point bending experiments on sandwich panels with an Alporas foam core, of varying size, with the panels designed to fail by core shear. By accounting for the size effects in the foam core shear strength, they were able to give a good estimate of the failure load of the panels.

Stress/strain concentrations due to notches, holes and inclusions in cellular solids are other topics of essential interest for experimental investigation. The effect of the notch size (relative to the cell size), is examined on aluminium closed cell foams (Antoniou *et al*. [2004]). They observed that under uniaxial compression, the net section strength of double-edge-notched specimens is larger when the net section width is smaller, whereas it is insensitive to the net section width in the case of single-edge-notched specimens. Mora and Waas [2000] performed uniaxial compression tests on a plate of polycarbonate honeycomb with circular cells, containing a cylindrical hole and a rigid inclusion, respectively. They could not detect any size effects in the case of the hole, but were able to fit the strain fields near the circular inclusion with the couple stress theory, for a variety of inclusion sizes.

1.5 Outline of this thesis

The aim of this thesis is to explore the microstructural origin of the size effects in the mechanical behaviour of cellular solids, in particular of metallic foams, and to investigate/propose generalized continuum theories that can capture these size effects.

In chapter 2, we use two-dimensional beam networks to mimic real (three-dimensional) foams, which allow us to account for the discreteness of their microstructure. We perform simple shear, uniaxial compression, and pure bending tests on a large variety of samples, and calculate the change in the macroscopic mechanical properties corresponding to a change in size. We close the chapter with a summary of the size effects that we observed in our calculations and discuss the possible mechanisms behind these size effects.

Chapter 3 uses the micropolar theory to capture the size effects observed in chapter 2. We fit the elastic constants of the micropolar continuum theory by comparing the analytical solution of the simple shear problem with the discrete analyses, in terms of the best agreement in the macroscopic shear stiffness of the samples. We develop a strain mapping procedure and evaluate the performance of the fitted micropolar constants in predicting the local deformation fields, the microrotations and shear strains. Finally, we solve the pure bending problem analytically for the micropolar theory and close the chapter with a discussion on the limitations of the Cosserat-type theories.

In chapter 4, we propose a generalized continuum theory (strain divergence theory), which associates energy to the divergence of strain. We derive the equilibrium equations and the boundary conditions for the strain divergence continuum, and develop a finite element implementation of the theory. We solve the simple shear and the pure bending problems analytically and compare the solutions with the discrete calculations, as well as with the analytical solutions for the couple stress theory.

Chapter 5 explores the strain concentration problem around a cylindrical hole in a field of uniaxial tension. First, we perform discrete calculations on samples with different hole sizes and show the effect of the hole size on the strain distribution near the hole. Then we compare the discrete analyses with the analytical solutions for the classical, couple stress and strain divergence theories.

Finally, in Chapter 6, we summarize the size effects that we observed in the mechanical behaviour of the two dimensional cellular solids, and we compare the different generalized continuum theories with respect to their ability in capturing size effects.

2 Discrete Analysis of Size Effects

In this chapter, we analyze size effects in the mechanical behaviour of cellular solids. For this purpose, we perform simple shear, uniaxial compression and pure bending tests on two-dimensional cellular materials, having regular (squares, hexagons) and irregular (perturbed hexagons, Voronoi tessellations) microstructures. We change the size of the samples gradually and measure the corresponding change in the overall elastic response.

2.1 Introduction

In Chapter 1, we gave an overview of the experimental work investigating the effects of the specimen size, relative to the cell size, on the measured mechanical properties of cellular solids (see Section 1.3). Experiments indicate that when the specimen size (and/or the loading wavelength) and the cell size are of the same order of magnitude, the individual response of cells varies considerably throughout the specimen. This leads to differences in the macroscopic response from one specimen to another with a different size. Classical continuum theory does not incorporate a length scale, and therefore cannot capture size-dependent behaviour. One approach to account for size effects, which will be followed in this chapter, is to explicitly account for the cellular morphology by modelling individual cell walls (or cell faces) by using the finite element method (see e.g. Andrews *et al.* [2001], Onck *et al.* [2001], Chen and Fleck [2002], Diebels and Steeb [2002]).

Our aim in this chapter is to investigate the size effects (and their physical grounds) in the mechanical behaviour of foams. To mimic the behaviour of real foams, we use two-dimensional microstructures (honeycombs), with both regular (square, hexagons) and irregular (perturbed hexagons, Voronoi tessellations) microstructures. In section 2.2, we introduce the mechanical properties and the deformation mechanisms of some two-dimensional microstructures, including the ones used in here. We discuss the effect of imperfections (such as cell wall misalignments, cell wall waviness, cell size variations, etc) on the mechanical behaviour of cellular solids, and modify our models accordingly to be able to represent metal foams more realistically. In section 2.3, we perform simple shear, uniaxial compression and pure bending tests on specimens with different microstructures. We change the specimen size gradually to detect the size effects. Finally, section 2.4 summarizes the size effects observed for each boundary value problem and comments on the underlying mechanisms.

2.2 Two-dimensional cellular solids

In this section, we discuss the mechanical behaviour of regular and irregular two-dimensional cellular solids and analyze their usefulness in representing real three-dimensional foam structures.

2.2.1. Regular cellular solids

Regular two-dimensional cellular solids (also referred to as lattices or honeycombs) are often used as two-dimensional representations of more complex three-dimensional foams. They enable closed-form expressions for the macroscopic in-plane properties as a function of the cell wall thickness t and length l, and the properties of the cell wall material (subscript s), the Young's modulus E_s, the Poisson's ratio ν_s, and the yield stress σ_{ys}. The three simplest lattice structures are the hexagonal structure, the square structure and the fully triangulated structure (see Fig. 2.1). Due to six-fold (hexagonal) symmetry (i.e. a structure has the same appearance six times in a 360° rotation around its centre), the triangulated and hexagonal structures are isotropic in

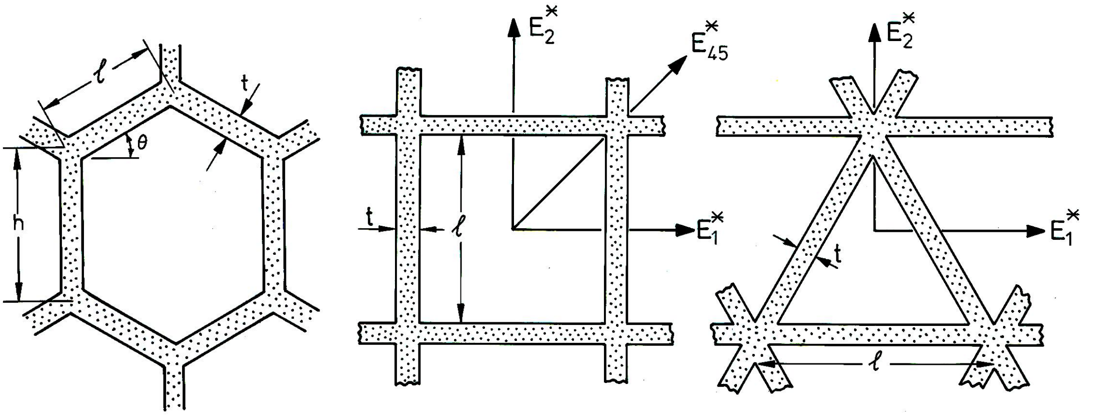

(a) (b) (c)

Figure 2.1: Regular two-dimensional cellular solids. (a) Regular hexagonal structure. (b) Square structure. (c) Triangular structure. (Reproduced, with permission, from Gibson and Ashby [1997]).

the plane (see e.g. Wang and Stronge [1999], Warren and Byskov [2002]), while the square structure, with four-fold symmetry, is orthotropic (see e.g. Ostoja-Starzewski *et al.* [1996]). For the low density isotropic structures, the Young's modulus can be written as

$$\frac{E^*}{E_s} = \frac{4}{\sqrt{3}} \left(\frac{t}{l} \right)^3 \tag{2.1}$$

for the hexagons[1] (Gibson *et al.* [1982]), and

$$\frac{E^*}{E_s} = \frac{2}{\sqrt{3}} \frac{t}{l} \tag{2.2}$$

for the triangles (Christensen [1995]). The square structure has two stiff directions, parallel to the cell walls,

---

[1] Neglecting shear deformations.

$$\frac{E_1^*}{E_s} = \frac{E_2^*}{E_s} = \frac{t}{l}, \tag{2.3}$$

and two compliant directions at 45° (Gibson and Ashby [1997]),

$$\frac{E_{45}^*}{E_s} = 2\left(\frac{t}{l}\right)^3. \tag{2.4}$$

The difference in stiffness between these structures is clearly exemplified by plotting Young's modulus as a function of the loading direction with respect to the microstructural orientation (see Fig. 2.2). The triangular and hexagonal structures are isotropic with the former being much stiffer than the latter. The underlying reason for this behaviour is the difference in the deformation mechanisms for different cell

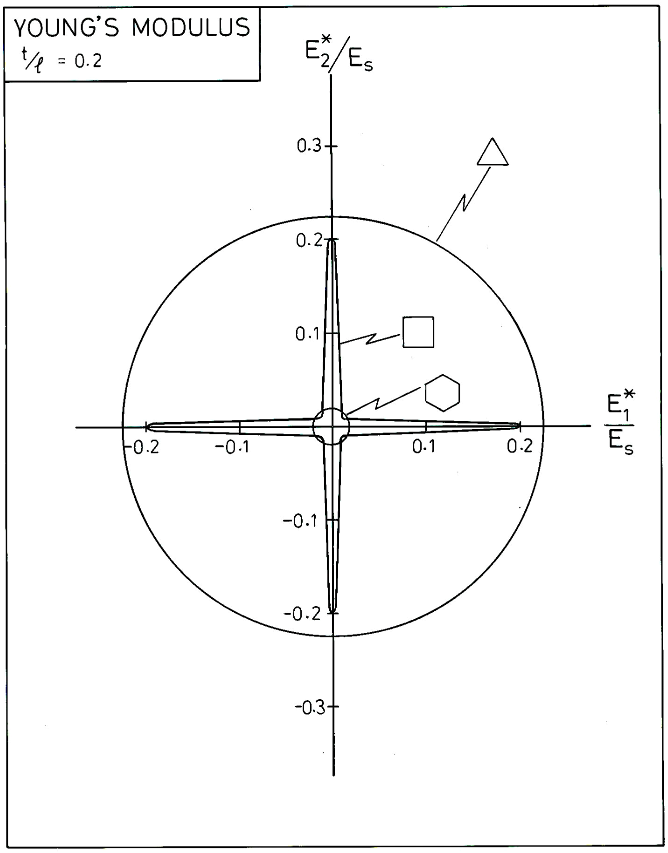

Figure 2.2: Young's modulus as a function of loading direction for triangular, square and hexagonal cells. The square structure is orthotropic with a low stiffness at 45° and a high stiffness at 0° and 90°. The hexagonal and triangular structures are isotropic, having a low and high stiffness, respectively. (Reproduced, with permission, from Gibson and Ashby [1997]).

topologies: cell wall bending versus cell wall stretching (see Grenestedt [1999], Deshpande *et al.* [2001a, b]). The hexagons and squares-at-45° (i.e. loaded in the diagonal direction) deform by cell wall bending, leading to a cubic dependence on t/l (see Eqs. 2.1 and 2.4), while the triangular structure and the square structure loaded parallel to the cell walls deform by cell wall stretching, leading to a linear dependence on t/l (see Eqs. 2.2 and 2.3). The uniaxial plastic properties of these structures show a comparable dependence on t/l (quadratic when bending-dominated and linear when stretching-dominated). Note that Fig. 2.2 is plotted for the same t/l value for all three microstructures, which means that the relative density is slightly different for each case.

A similar difference in bending versus stretching response is observed for three-dimensional models of perfect (i.e. without imperfections) cellular solids (Gibson and Ashby [1997]). A more suitable scaling quantity of the mechanical properties of three-dimensional foams is the relative density ρ. The relative density is the density of the cellular material divided by the density of the cell wall material, and it scales with $(t/l)^2$ for open-cell foams and with t/l (here t is the thickness of the cell faces) for closed-cell foams. Open-cell foams deform by bending, yielding a quadratic dependence on ρ for stiffness and a power 3/2 dependence for plastic strength. Closed-cell foams, on the other hand, deform by stretching of the cell faces, giving a linear dependence on ρ for both stiffness and strength. Table 2.1 summarizes these scaling relations for cellular solids having a perfect cellular structure.

Table 2.1

Scaling relations for perfect cellular solids.

	Relative density	Stiffness	Plastic strength
2D cellular solids	$\rho \propto t/l$		
1. bending-dominated		$E^*/E_s \propto \rho^3$	$\sigma^*_{pl}/\sigma_{ys} \propto \rho^2$
2. stretching-dominated		$E^*/E_s \propto \rho$	$\sigma^*_{pl}/\sigma_{ys} \propto \rho$
3D open-cell foams	$\rho \propto (t/l)^2$	$E^*/E_s \propto \rho^2$	$\sigma^*_{pl}/\sigma_{ys} \propto \rho^{3/2}$
3D closed-cell foams¶	$\rho \propto t/l$	$E^*/E_s \propto \rho$	$\sigma^*_{pl}/\sigma_{ys} \propto \rho$

¶Assuming all material is in the cell faces (having a thickness t).

Experiments on closed-cell metal foams, however, show a scaling that closely resembles that of open-cell foams, owing to the fact that imperfections in the cell faces (such as curvatures, corrugations and cracks) reduce their mechanical contribution, promoting bending of the cell edges to be the dominant deformation mechanism (Sugimura *et al.* [1997], Simone and Gibson [1998b], Bart-Smith *et al.* [1998], Andrews *et al.* [1999]). Analytical and finite element models of closed cell foams accounting for such imperfections are in good agreement with these experiments (Simone and Gibson [1998a], Grenestedt [1998]). Due to the random distribution of cell size and shape, the overall mechanical properties of three-dimensional foams are isotropic. Since the two-dimensional hexagonal structure is isotropic and deforms by cell wall bending as well, it is an attractive model material for the elastic and plastic behaviour of real three-dimensional foams in case of uniaxial loading.

2.2.2 Irregular cellular solids

Although hexagons are useful as a model material under uniaxial stress states, under multiaxial stress states, however, the mechanical behaviour of regular hexagons diverges from that of real metal foams. When hexagons are loaded equi-biaxially (macroscopic normal stresses $\sigma_1=\sigma_2$), all internal bending moments in the structure vanish, causing cell wall stretching to be the dominant deformation mechanism. As a result, the yield strength under hydrostatic loading (i.e. in-plane equi-biaxial compression) is much higher than under deviatoric loading (such as uniaxial compression), making the yield surface elongated in the $\sigma_1=\sigma_2$ direction, see Fig. 2.3.

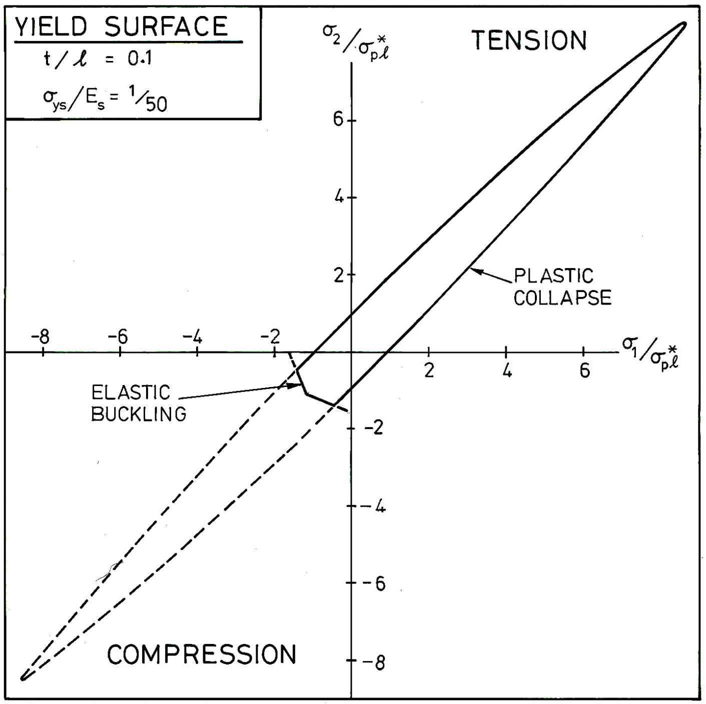

Figure 2.3: The yield surface for a regular hexagonal structure for $t/l=0.1$. Stresses are normalized with the uniaxial plastic strength $\sigma^*_{pl}=2/3\ (t/l)^2$. (Reproduced, with permission, from Gibson and Ashby [1997]).

A similar conclusion can be drawn for the elastic properties in terms of the bulk modulus versus Young's modulus. Experimentally-obtained yield surfaces of real foams, however, are approximately circular in the deviatoric-hydrostatic stress space (e.g. Gioux *et al.* [2000], Deshpande and Fleck [2000], Doyoyo and Wierzbicki [2003]), demonstrating that the yield strength under hydrostatic loading is approximately the same as under uniaxial loading. This can be traced to the fact that under both stress-states, plastic bending is the dominant deformation mode, due to the presence of imperfections. In two-dimensional structures this behaviour can be mimicked by introducing imperfections such as wiggles, missing cell-walls and cell-wall misalignments in the regular hexagonal structure, or by using Voronoi tessellations which account for the cell size variations (Grenestedt [1997], Triantafyllidis and Schraad [1998], Chen *et al.* [1999]). This causes a much bigger knock-down in the hydrostatic properties than in the uniaxial properties, leading to a circular yield surface.

Cell wall misalignments are introduced in the regular hexagonal microstructures by displacing all triple junctions with coordinates (x_1, x_2) in a random direction θ and over a random distance b, chosen from a uniform distribution $[0, \alpha l]$, where α is a constant and l is the cell wall length (see Fig. 2.4a). Then the new coordinates (x_1', x_2') can be written in terms of the old ones as

$$\begin{aligned} x_1' &= x_1 + b\cos\theta, \\ x_2' &= x_2 + b\sin\theta. \end{aligned} \tag{2.5}$$

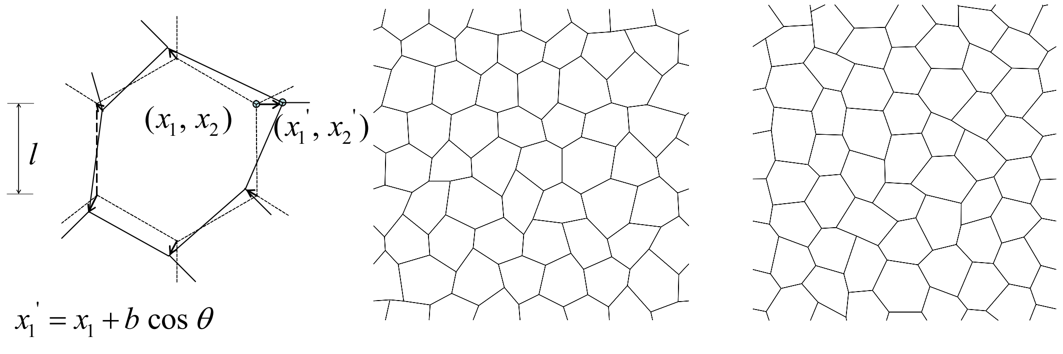

(a) (b) (c)

Figure 2.4: (a) Sketch illustrating the introduction of cell wall misalignments into a regular hexagonal microstructure. (b) Perturbed hexagonal microstructure in the default orientation for α=0.4. (c) Perturbed hexagonal microstructure in the rotated orientation for α=0.4.

These structures, called ‘perturbed hexagons’, will be adopted as one of the two-dimensional structures to study size-effects in Section 2.3. Although the perturbed hexagonal microstructures are produced in a random manner, they still might carry the underlying topological foot-print of the hexagonal “close-packed” ordering. To analyze this, two orientations of the perturbed hexagonal microstructures with respect to the loading direction will be investigated, termed the ‘default orientation’ (Fig. 2.4b) and the ‘rotated orientation’ (Fig. 2.4c), using $\alpha = 0.4$.

To account for a fully random distribution of cell sizes and shapes, we use Voronoi [1908] tessellations. The Voronoi tessellation technique is akin to a foaming process, where bubbles nucleate at random sites and expand in the liquid material. The final space-filling packing of cells is identical to a Voronoi tessellation if the following assumptions are made (see also Zhu *et al.* [2001a] and the references therein):

1. All nuclei appear simultaneously.
2. All nuclei remain fixed in location throughout the growth process.
3. For each nucleus, the growth occurs at the same rate in all directions.
4. The linear grow rate is the same for each cell associated with a nucleus
5. Growth ceases for each cell whenever and wherever it comes into contact with a neighbouring cell.

Based on these assumptions, the final shape and the size of the cells are uniquely determined by the initial distribution of the nuclei. Even though a foaming process is more complicated than the model suggested here[2], the experimentally measured topology parameters (e.g. average number of struts per cell face, average number of faces per cell, etc.) of many foams are in close agreement with those of Voronoi tessellations (see Gibson and Ashby [1997]).

To create two-dimensional Voronoi diagrams, a set of nuclei is generated in a rectangular box with area A. For a fully random tessellation (often referred to as a Γ-Voronoi), the coordinates of the nucleation points are chosen randomly (i.e. from a uniform distribution). Once all the nucleation points are created, adjacent points are connected to each other by straight lines (see the dashed lines in Fig. 2.5), resulting in a triangulation of the area, known as a Delaunay [1934] triangulation. Voronoi polygons are then generated by drawing normals that divide the dashed connector lines (i.e. the sides of the Delaunay triangles) into two and finally trimming these normals where they meet (see Fig. 2.5). We use the commercial software Matlab to create Voronoi diagrams.

---

[2] Typical for closed-cell metal foams is cell coalescence, as a result of which the one-to-one correspondence between nucleus and cell is lost.

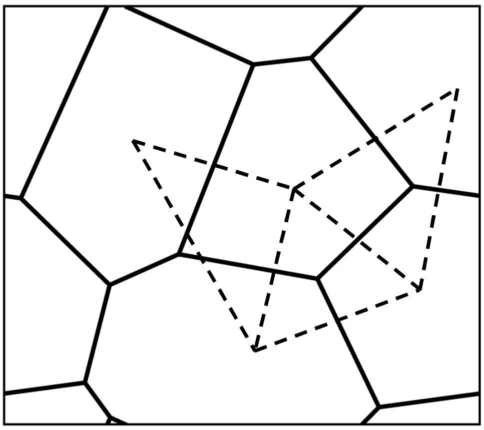

Figure 2.5: Construction of a Voronoi diagram. Adjacent nucleation points are connected to each other by straight lines (dashed). Drawing normals that divide these connector lines into two and trimming these normals where they meet generate Voronoi polygons (solid lines).

In a Γ-Voronoi the nucleation sites can be arbitrarily close together, leading to a wide distribution of cell sizes. Many open-cell foams, however, have a much narrower cell-size distribution. This can be straight-forwardly accounted for by imposing a constraint on the distribution of nuclei. One way of imposing such a constraint is to start from a distribution of nuclei corresponding to a regular hexagonal microstructure and then to displace each nucleus in a restricted area around the initial position (see e.g., Van der Burg *et al.* [1997], Fazekas *et al.* [2002]). Another method, the one employed here, is to randomly place n nucleation points in the area A such that the separation between any two nuclei must be larger than a minimum allowable distance, s (e.g. Zhu *et al.* [2000, 2001a, b]). The resulting structure is called a δ-Voronoi, to be distinguished from the fully random Γ-Voronoi. To classify the randomness, the separation distance can be normalized by a reference length r, defined as

$$r = \sqrt{\frac{2A}{\sqrt{3}n}}, \tag{2.6}$$

being the distance between any two adjacent nuclei if the n nucleation points (i.e. number of cells) in the area A, would have been distributed in a closed-packed manner so as to generate a regular hexagonal packing. The measure of randomness, $\delta = s/r$ ranges from $\delta = 1$, the regular case of perfect hexagons, to $\delta = 0$, the fully random case of a Γ-Voronoi.

Depending on the boundary value problem analyzed, we used either periodic or displacement boundary conditions in the following. The periodicity of the Voronoi diagrams is achieved by dividing the two-dimensional plane into nine equal rectangles, the one in the middle being an RVE (Representative Volume Elements) with area A. For each nucleation point created in A, a corresponding point is created in each of the eight surrounding areas. Each subsequent nucleation point is accepted only if it is located at a distance greater than δ from the points already present. Once all nucleation points are created, the Voronoi tessellation is generated, which accounts for full periodicity of the middle area A. Finally, the periodic RVE is obtained by cutting the middle area A from the centre of the nine rectangles. Figure 2.6 shows three Voronoi structures with different levels of randomness, $\delta = 0$, 0.4 and 0.7, with periodicity being accounted for.

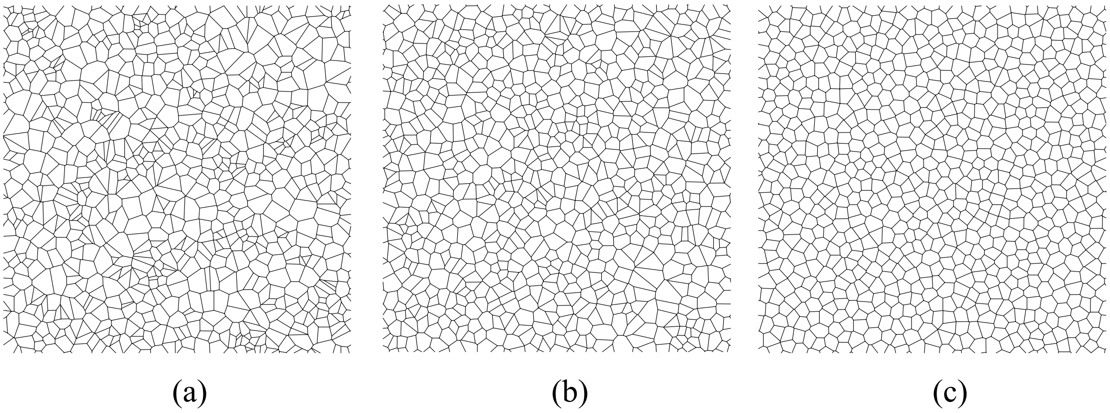
(a) (b) (c)

Figure 2.6: Voronoi tessellations: (a) $\delta=0$. (b) $\delta=0.4$. (c) $\delta=0.7$. Periodicity is accounted for.

2.2.3 The effect of imperfections in Voronoi structures

As stated in the previous section, Voronoi tessellations have a less elongated yield surface than regular hexagons, due to their non-uniform cell size distribution. However, to represent real foams, a further knockdown of the hydrostatic yield strength, relative to the uniaxial strength, is needed. For this purpose, we introduced two types of imperfections in the Voronoi structures. The first one consists of cell wall misalignment as also applied on the hexagonal structures, see Fig. 2.4. In the case of the Voronoi tessellations, the lengths of the cell walls that meet at a junction are not the same. To avoid convex shaped cells, we pick the random displacement of a junction node from a uniform distribution in the range 0 to αl_{m}, where l_{m} is the minimum of the cell wall lengths among those connected to this junction. The second imperfection is cell wall waviness. To introduce cell wall waviness, we impose a lateral displacement on cell walls, in such a way that it turns a straight cell wall into a sinusoidal-shaped cell wall, according to

$$y(x) = q \sin\left(\frac{\pi x}{l}\right), \tag{2.7}$$

where q is a random number chosen from a uniform distribution $[0, \beta l]$, with β a constant, which defines the amplitude of the cell wall waviness, l is the cell wall length and x and y are the coordinates on a local Cartesian frame with x being the coordinate along the end-to-end distance. By comparing the morphology of the generated microstructures with the electron microscope images of real cellular solids, it was concluded that for α larger than 0.2 or β larger than 0.06, the microstructures are not realistic. To illustrate the morphological changes introduced by the imperfections, Fig. 2.7a shows a fully random ($\delta = 0$) Voronoi diagram (i.e. $\alpha = 0$, $\beta = 0$, in red) on top of which the same structure is plotted having the triple points randomly displaced ($\alpha = 0.2$, $\beta = 0$, in green). Then, in Fig. 2.7b, cell wall wiggles are imposed on the perturbed structure (in green), resulting in a ($\alpha = 0.2$, $\beta = 0.06$) microstructure, in blue.

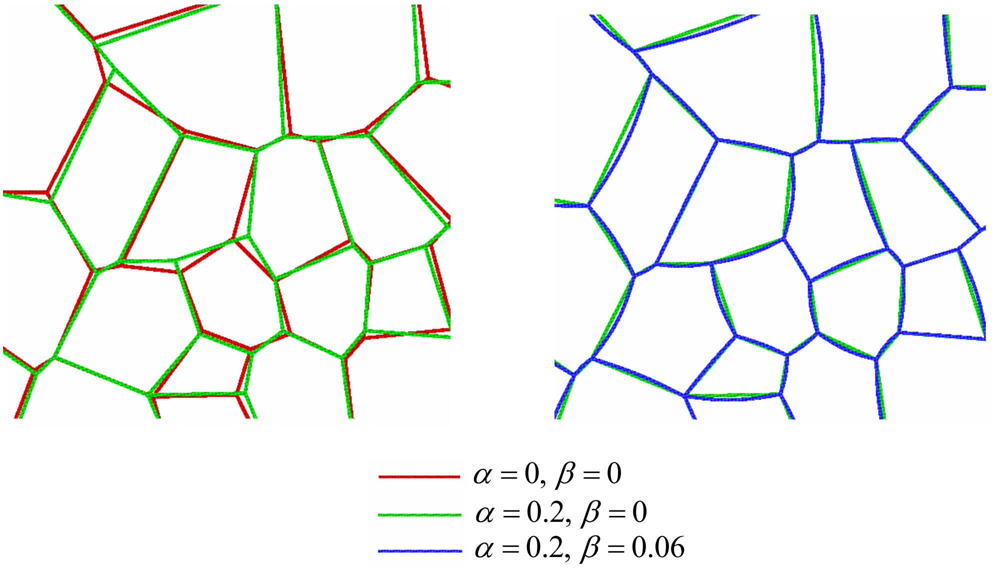

(a) (b)

Figure 2.7: (a) Fully random (δ=0) Voronoi diagram (i.e. α=0, β=0, in red) on top of which the same structure is plotted with α=0.2, β=0 (in green). (b) Fully random (δ=0) Voronoi diagram with triple points perturbed (α=0.2, β=0, in green) on top of which cell wall wiggles are imposed (α=0.2, β=0.06, in blue).

To evaluate the effect of the imperfections on the yield surface of the Voronoi tessellations, we performed uniaxial compression and hydrostatic loading tests on periodic RVE's (Representative Volume Elements) with different levels of imperfections, each containing 800 cells. We assume that all the cell walls in a microstructure have the same, uniform thickness t. For two dimensional structures, the relative density ρ reduces to the area fraction of solid material; it is directly proportional to the cell wall thickness t and is given by

$$\rho = \frac{t\sum_{i=1}^{k} l_i}{L_1 L_2}, \tag{2.8}$$

where k is the total number of cell walls within the microstructure and L_1 and L_2 the side lengths of the rectangular area analyzed. To discretise the cell walls, we use quadratic Timoshenko beam elements (B22 element in ABAQUS element library). Some cell walls in random microstructures (perturbed hexagons and Voronoi tessellations) are too short to be modelled as beam elements, and their percentage increases with increasing randomness. To decrease the contribution from these stocky cell walls, we remove those with a thickness to length ratio larger than 1/2 for a relative density 0.1. One of the end nodes of any removed cell wall is deleted, and the cell walls that were connected to this deleted node are reconnected to the undeleted one. There still remain some stocky cell walls in the microstructures, with a thickness to length ratio larger than 1/3, but their percentage, even in fully random tessellations, is less than 5 percent and the error due to modelling them as beam elements is expected to be small (Chen *et al.* [1999]). To ensure that the relative density is the same for different random realizations due to the removal of stocky cell walls, we redefine the cell wall thickness after the removal process. Silva *et al.* [1995] reported that the effective stiffness of a microstructure increases with decreasing percentage of stocky cell walls, due to the decrease in the total number of degrees of freedom in the microstructure. We observe an opposite tendency, i.e., both the effective stiffness and the plastic yield strength decreases with decreasing percentage of stocky cell walls. This trend is related to the fact that after the removal of stocky cell walls the average cell wall length in the cellular materials increases (and therefore the thickness decreases to ensure a constant density), making the material more compliant.

In case of elastic deformation, only a single beam element per cell wall is sufficient for a converged solution. To investigate mesh sensitivity in case of plastic deformation, we used two different discretisation methods. The first method is to discretise each cell wall with the same number of beam elements, resulting in 16 to 20 elements per cell wall for a converged solution. The second method is to keep the length of a beam element constant and equal to the cell wall thickness t, in which case the number of beam elements used to model a cell wall is given by the ratio of the length of this cell wall, l_i, to the cell wall thickness t. This number can be 30 to 40 for relatively long cell walls, and this increases the computational time excessively. Therefore, we limited the maximum number of beam elements used to model a cell wall and change this limit to see its effect. A converged solution is obtained when the limit is set to be 10, which required much less computational time than the first method. The second method, with the maximum number of beam elements set to 10, was used for all calculations reported.

The cell wall material is assumed to be elastic-plastic with a Young's modulus of $E_s = 70$ GPa, a Poisson's ratio of $\nu_s = 0.33$, and a yield stress of $\sigma_{ys} = 130$ MPa. The relative density of the samples is chosen to be $\rho = 0.1$, which is high enough to avoid premature elastic buckling of the cell walls for the material properties used. To avoid numerical problems for the finite element calculations, we employ linear isotropic hardening using a relatively low hardening slope of $H = d\sigma/d\varepsilon =$ 100 MPa. We apply periodic boundary conditions on pairs of nodes J and I, located at the same position but on the opposite edges of the boundary, by describing

$$u_p^{\mathrm{J}} - u_p^{\mathrm{I}} = \varepsilon_{pq}(x_q^{\mathrm{J}} - x_q^{\mathrm{I}}), \quad \phi_3^{\mathrm{J}} - \phi_3^{\mathrm{I}} = 0, \quad p,q = 1,2. \tag{2.9}$$

The corresponding macroscopic stresses read

$$\sigma_{pq} = \frac{1}{2L^2} \sum ((x_p^{\mathrm{J}} - x_p^{\mathrm{I}})F_q^{\mathrm{J}} + (x_q^{\mathrm{J}} - x_q^{\mathrm{I}})F_p^{\mathrm{J}}), \tag{2.10}$$

where L is the length of the square Voronoi diagram, ϕ_3 is the rotation of the cell walls in the x_1-x_2 plane, F_p^{J} are the reaction forces in nodes J (periodicity corresponds to $F_p^{\mathrm{I}} = -F_p^{\mathrm{J}}$), and the summation is carried out over all the boundary nodes J. The shear strain ε_{12} is taken to be zero. In the case of uniaxial loading, ε_{11} (ε_{22}) is incremented while letting the edges with a surface normal parallel to the x_2 (x_1) direction traction free. For the case of hydrostatic loading, ε_{11} is kept equal to ε_{22}. Similar boundary conditions were employed by Chen *et al.* [1999].

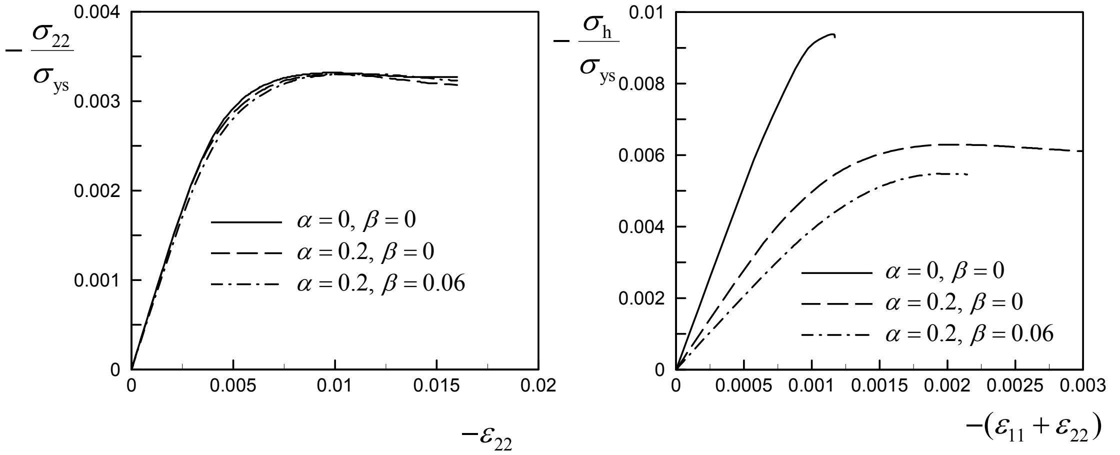

(a) (b)

Figure 2.8: (a) The calculated compressive stress σ_{22} normalized by the yield stress σ_{ys} plotted against the compressive uniaxial strain ε_{22} for $\delta = 0$ Voronoi tessellations. (b) The calculated hydrostatic tress σ_h normalized by the yield stress σ_{ys} plotted against the hydrostatic strain ($\varepsilon_{11} + \varepsilon_{22}$).

Figures 2.8a and b demonstrate the results for the uniaxial and hydrostatic compressive loadings, respectively, for fully random Voronoi tessellations (δ = 0). The hydrostatic stress is defined as $\sigma_{\mathrm{h}} = \sigma_{pp}/2$, as in (Chen *et al.* [1999]), and the yield strength is defined by the peak of these stress strain curves. We see that either cell wall misalignments or cell wall waviness have a negligible effect on the compressive uniaxial yield strength (Fig. 2.8a). The hydrostatic yield strength, on the other hand, is highly reduced by the existence of cell wall misalignments ($\alpha = 0.2$, $\beta = 0$, Fig. 2.8b). The additional effect on the hydrostatic yield strength associated with cell wall waviness is relatively small ($\alpha = 0.2$, $\beta = 0.06$, Fig. 2.8b). Table 2.2 shows an overview of the ratio of the Young's modulus to the bulk modulus, E/κ, and the compressive yield strength to the hydrostatic yield strength, $\sigma_{\mathrm{u}}/\sigma_{\mathrm{h}}$, for Voronoi tessellations, with different δ, α and β values. It can be observed that the ratio $\sigma_{\mathrm{u}}/\sigma_{\mathrm{h}}$ is smaller for more regular structures, which is in accordance with the conclusions of Chen *et al.* [1999]. The same tendency holds for the ratio E/κ as well. Note that κ and σ_{h} scale linearly with the relative density, while σ_{u} scales quadratically and E cubically.

Table 2.2

The ratio of the Young's modulus to the bulk modulus, E/κ, and the compressive yield strength to the hydrostatic yield strength, $\sigma_{\mathrm{u}}/\sigma_{\mathrm{h}}$, for Voronoi tessellations, with different δ, α and β values.

δ	0	0	0	0.4	0.4	0.4	0.7	0.7	0.7
α	0	0.2	0.2	0	0.2	0.2	0	0.2	0.2
β	0	0	0.06	0	0	0.06	0	0	0.06
E/κ	0.071	0.128	0.174	0.064	0.120	0.156	0.058	0.128	0.152
$\sigma_{\mathrm{u}}/\sigma_{\mathrm{h}}$	0.35	0.53	0.60	0.30	0.49	0.50	0.19	0.43	0.44

2.3 Size effects

In this section we investigate the effect of specimen size on the elastic response of regular (square and hexagonal lattices) and irregular (perturbed hexagons and Voronoi tessellations) cellular structures. We will explore simple shear (section 2.3.1), uniaxial compression (section 2.3.2) and pure bending (section 2.3.3) boundary value problems. All the calculations are performed assuming the strains to be small.

2.3.1 Simple shear

Figures 2.9a and b show the boundary conditions for a simple shear test on a sandwich panel having a perfect hexagonal microstructure (in the default orientation) and a Voronoi microstructure as a core, respectively. Here and in the rest of this thesis, we will focus on Voronoi tessellations with $\delta = 0.7$, $\alpha = 0.2$ and $\beta = 0$ (see section 2.2.3). For all microstructures we use one beam element per cell wall, take a relative density $\rho = 0.1$ and use a Poisson's ratio $\nu_s = 0.33$. The results shown are normalized by the Young's modulus of the cell wall material, E_s. To have a common measure for the cell size *d*, both for the hexagonal microstructures (regular and perturbed) and the Voronoi tessellations, we take $d \approx 1.82l$, equal to the diameter of a circle with the same area as a regular hexagonal cell with a cell wall length *l*. Note that for the Voronoi structures the average cell wall length l_{av} can be deduced from the area *A* and the number of nuclei *n*, through $l_{av} = r/\sqrt{3}$, with *r* defined in equation 2.6. For the square microstructures, $d = l$ (see Fig. 2.1c). To avoid the edge effects common to the shear problem, we take an infinitely long material in the x_1 direction. Consequently, in case of regular microstructures such as perfect hexagons and squares, it suffices to analyze only one column of cells and to apply periodic boundary conditions on both sides of the unit cell (see the indicated region in Fig. 2.9a). For irregular microstructures, on the other hand, due to the stochastic imperfections, the unit cell is enlarged to $L \approx 143d$, still featuring periodic boundary conditions (see Fig. 2.9b).

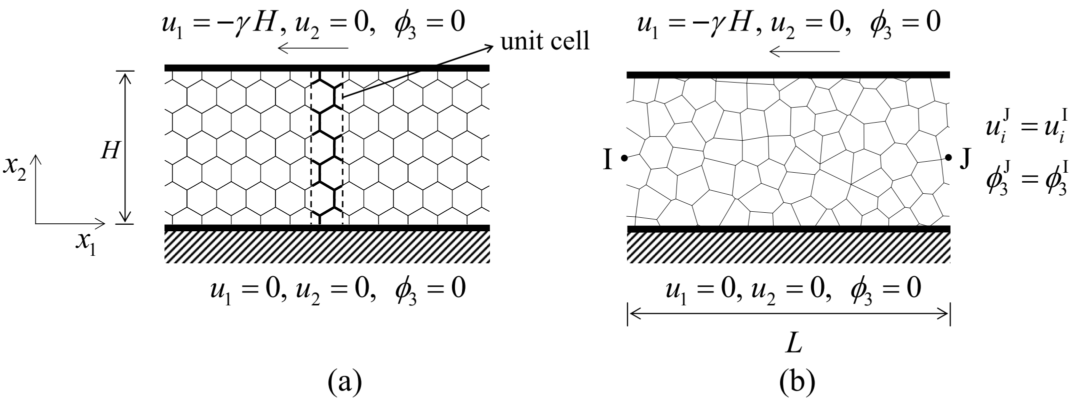

Figure 2.9: Boundary conditions for a simple shear test on a sandwich panel: (a) Perfect hexagonal microstructure in the default orientation. (b) Voronoi microstructure.

The face sheets are assumed to be rigid and perfectly bonded to the cellular material. This allows applying the boundary conditions directly to the cellular structure. At the bottom all degrees of freedom are constrained ($u_i = \phi_3 = 0$, $i = 1,2$). Note that the u_i and ϕ_3 are the displacements and rotations of the cell walls at the locations were they are connected to the face sheets. At the top a horizontal displacement is applied, $u_1 = -\gamma H$, consistent with a shear strain γ, while the other degrees of freedom are constrained, $u_2 = \phi_3 = 0$. The macroscopic shear stress is obtained by dividing the sum of the reaction forces at the top nodes by the area of the unit cell, $L\,b$, where *b* is the out of plane thickness and *L* is the length of the unit cell in the x_1 direction. The ratio of the shear stress to the applied shear strain gives the macroscopic shear stiffness, $F/(L\gamma)$, with F the total shear force per unit out-of-plane thickness.

The value of the macroscopic shear stiffness depends not only on the relative specimen height H/d, but also on the length and the orientation of the cell walls at the boundaries, to which we refer to as the boundary configuration. To consistently check the dependence on the boundary configuration, we also analyze the regular and perturbed hexagons in a 90° rotated orientation (termed the rotated orientation), as compared to the default orientation shown in Fig. 2.9a. For the same reason, we analyze different possibilities of "cutting specimens" for each value of H/d. As an example, Figure 2.10 shows two different cuts from a perfect hexagonal microstructure in the default orientation, with the same height, but with different boundary configurations. In the case of regular microstructures, only a limited amount of cuts (6 and 8 for the default and the rotated orientation of the regular hexagonal microstructures, respectively, and 5 for the square microstructures) are sufficient to cover almost all possible boundary configurations. For irregular microstructures (perturbed hexagons and Voronoi tessellations), we take 100 different cuts. Each new sample is made by shifting the sample window (corresponding to one specific value of H/d) over a certain distance with respect to the previous sample. This distance is called the cutting step size (CSS). For the irregular calculations performed here we use CSS = $d/10$. By performing convergence tests for $H/d = 1, 2, 3$, and 5 on perturbed hexagonal microstructures, we found that for more than 100 cuts, the average and standard deviation of the macroscopic shear stiffness did not change anymore. Note that for each specimen cut, the thickness of the cell walls is adjusted to ensure that all specimens have the same relative density.

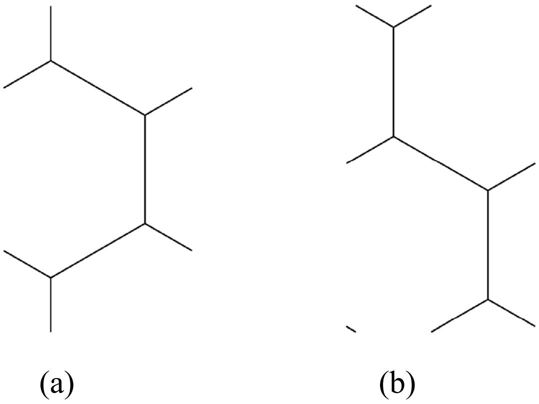

Figure 2.10: Two different cuts with the same height for the regular hexagonal microstructure in the default orientation.

Figure 2.11 shows the macroscopic shear stiffness, $F/(L\gamma)$, normalized by the shear modulus, G, plotted against the relative specimen size, H/d, for the microstructures analyzed. Each dot in Fig. 2.11 corresponds to one finite element calculation. For each microstructure, G corresponds to the effective shear stiffness of an infinitely large block with the corresponding microstructure. For the square structure in its current orientation (see the inset of Fig. 2.11a) it is given by

$$G = \frac{1}{2} E_{\mathrm{s}} (t / l)^3 \frac{1}{1 + (2.4 + 1.5\nu_s)(t / l)^2}, \tag{2.11}$$

and for the regular hexagonal microstructures, irrespective of the orientation, it is given by

$$G = \frac{1}{\sqrt{3}} E_{\mathrm{s}} (t / l)^3 \frac{1}{1 + (3.30 + 1.75\nu_s)(t / l)^2}, \tag{2.12}$$

where E_{s} is the Young's modulus and ν_{s} is the Poisson's ratio of the solid material from which the cellular structure is made (see also Gibson and Ashby [1997]). For irregular microstructures, the shear modulus is found by performing a convergence test while continuously increasing the thickness of the specimens. We found that for the irregular microstructures analyzed the value of the shear modulus is approximately 10–15 percent larger compared to the regular hexagons. A comparable enhanced stiffness was found by Silva *et al.* (1995) for a δ-Voronoi structure.

For the square microstructures, we observe a large scatter in data, especially in the small H/d regime, which decreases with increasing height (see Fig. 2.11a). The overall shear stiffness increases with decreasing height, and it converges to the shear modulus with increasing H/d, given in Eq. 2.12. This stiffening behaviour, $F/(LG\gamma) > 1$, is associated with the constrained rotations of the cell walls bound to the top and bottom face sheets. It is interesting to see that weakening, i.e. $F/(LG\gamma) < 1$, is also possible for some boundary configurations for small values of H/d. This is related to the fact that we keep the density constant for all specimens, leading to thinner cell walls for some configurations. On average, nevertheless, there is a stiffening behaviour in the small H/d regime.

For the regular hexagons in the default orientation we observe weakening behaviour for some boundary configurations as well (see Fig. 2.11b), but this is absent for the hexagons in the rotated orientation (Fig. 2.11c). For the irregular microstructures (perturbed hexagons and Voronoi tessellations, Figs. 2.11d-f), the effect of the constrained boundary layers (leading to stiffening) is always dominant over the effect of the lower cell wall thickness (leading to weakening). The scatter in data for small H/d is less in case of irregular microstructures and tends to zero with

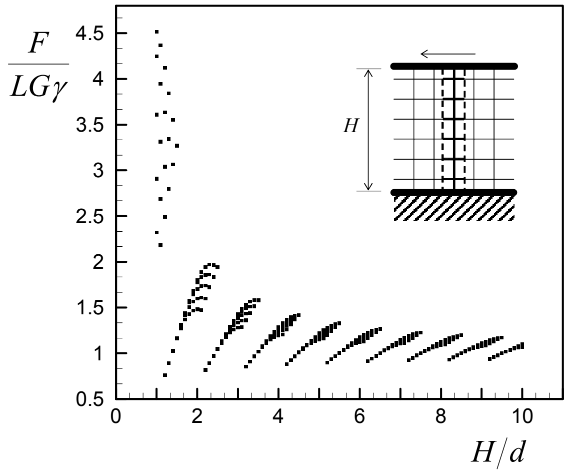
$\frac{F}{LG\gamma}$
4.5
4
3.5
3
2.5
2
1.5
1
0.5
0
2
4
6
8
10
H/d
H

(a)

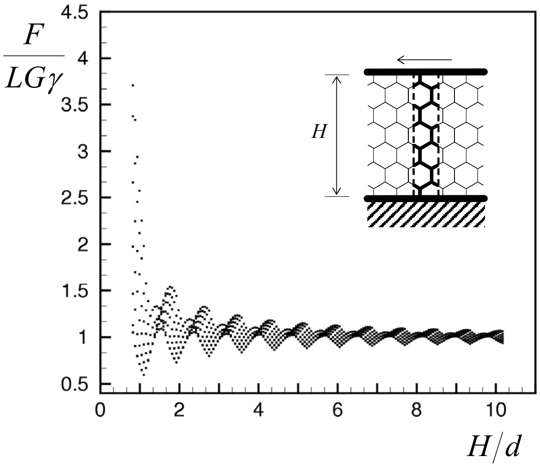
$\frac{F}{LG\gamma}$
4.5
4
3.5
3
2.5
2
1.5
1
0.5
0
2
4
6
8
10
H/d
H

(b)

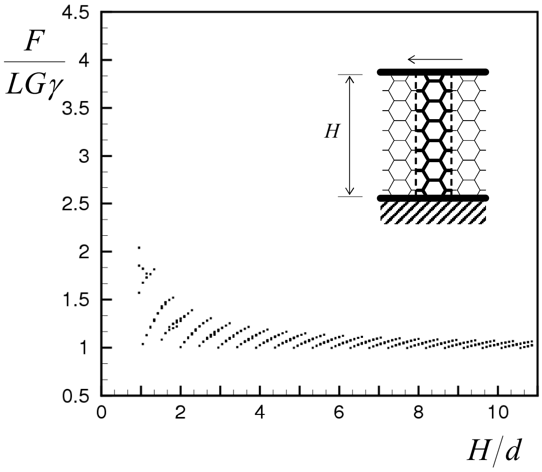
$\frac{F}{LG\gamma}$
4.5
4
3.5
3
2.5
2
1.5
1
0.5
0
2
4
6
8
10
H/d
H

(c)

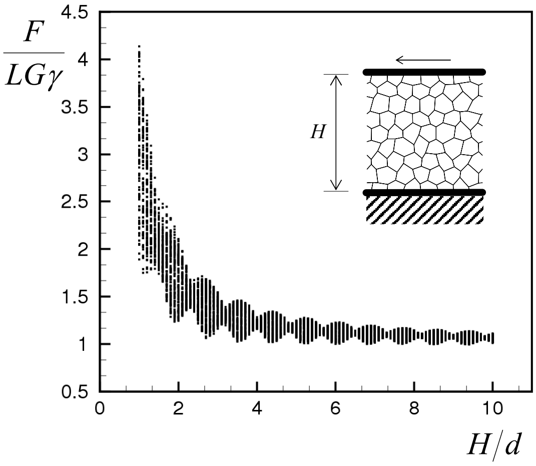
$\frac{F}{LG\gamma}$
4.5
4
3.5
3
2.5
2
1.5
1
0.5
0
2
4
6
8
10
H/d
H

(d)

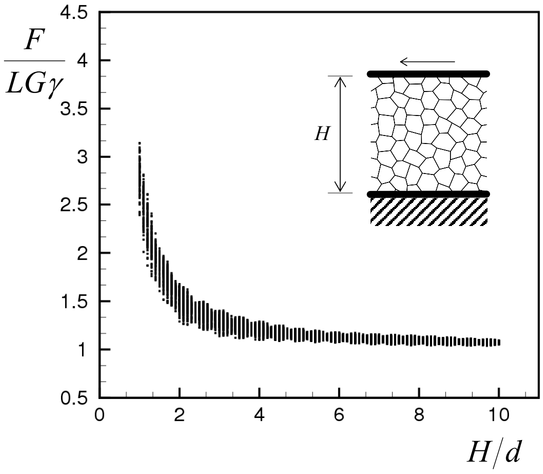
$\frac{F}{LG\gamma}$
4.5
4
3.5
3
2.5
2
1.5
1
0.5
0
2
4
6
8
10
H/d
H

(e)

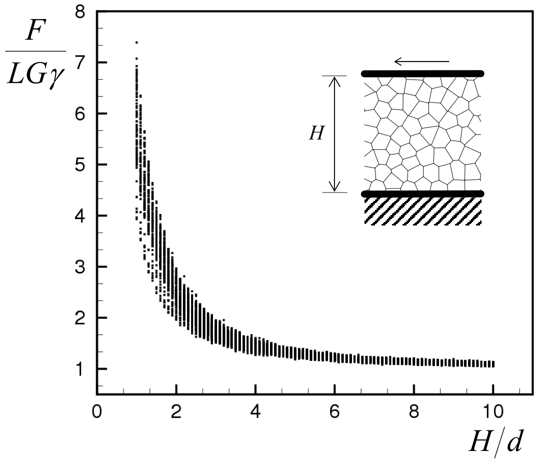

(f)

Figure 2.11: The macroscopic shear stiffness, $F/(L\gamma)$, normalized by the shear modulus, G, plotted against the relative specimen size, H/d, for the: (a) Square microstructure. (b) Perfect hexagonal microstructure in the default orientation. (c) Perfect hexagonal microstructure in the rotated orientation. (d) Perturbed hexagonal microstructure in the default orientation. (e) Perturbed hexagonal microstructure in the rotated orientation. (f) Voronoi microstructure.

increasing height. The stiffening effect is larger than it is for the regular hexagons, being largest for the Voronoi tessellations (see Fig. 2.11f).

The system parameters that determine the overall elastic response to a shear deformation are t, d, H, E_s and ν_s. From the three length scales two dimensionless quantities can be constructed: t/d (that is proportional to the relative density) and H/d. For the size effects we explored the effect of H/d for one value of the relative density. To explore the effect of t/d we repeated the calculations for values of t/d in the range 0.001–0.15. No effect was found on the $F/(GL\gamma)$ versus H/d curves, indicating that the effect of the relative density only enters through the definition of the shear stiffness G. In other words, the overall stiffness S $(=F/(L\gamma))$ can be written in terms of the system parameters (neglecting the effect of shear deformation of the cell walls) as

$$S\left(t, d, H, E_s\right) = G f\left(\frac{H}{d}\right), \tag{2.13}$$

with

$$G = cE_s\left(\frac{t}{d}\right)^3, \tag{2.14}$$

with the dimensionless constant c and the function f being specific for the cellular microstructure under consideration.

2.3.2 Uniaxial compression

We performed uniaxial compression tests for the irregular microstructures (perturbed hexagons and Voronoi tessellations) only. Figure 2.12 shows the boundary conditions for a uniaxial compression test in the x_1 direction on a perturbed hexagonal microstructure in the default orientation. We apply periodic boundary conditions on the left and the right boundaries of the structure, to imitate an infinitely long material in the x_1 direction, $u_1^J - u_1^I = \varepsilon_{11}(x_1^J - x_1^I)$, $u_2^J - u_2^I = 0$ and $\phi_3^J - \phi_3^I = 0$. J and I are pairs of nodes on opposite edges of the mesh (see Fig. 2.12). The top and bottom boundary nodes are prescribed to be force and moment free. The compressive stress is calculated by dividing the sum of the reaction forces on the boundary nodes by the area under compression, *Hb*. The uniaxial compressive stiffness is calculated from the ratio of the compressive stress and the compressive strain, and is given by $F/(H\varepsilon_{11})$, with F being the force per unit out-of-plane thickness. The length of the specimens relative to the cell size is taken to be large enough ($L/d = 150$) to ensure that the uniaxial compressive stiffness is independent of L/d. We increase the height of the block, taking 100 different cuts for each H/d value.

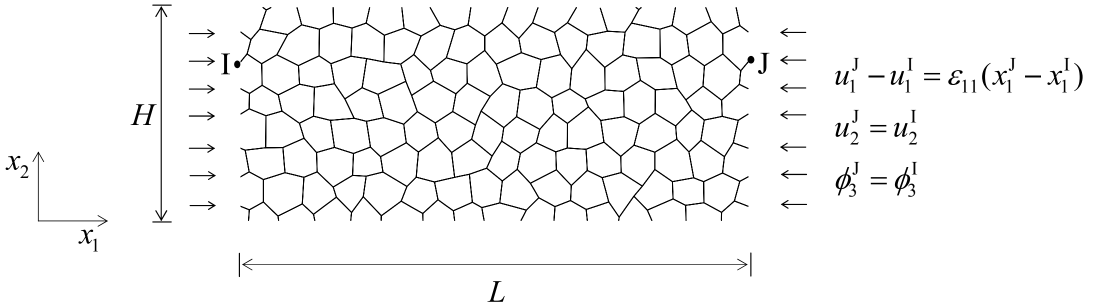

Figure 2.12: Boundary conditions for a uniaxial compression test on a perturbed hexagonal microstructure in the default orientation.

Figure 2.13 shows the calculated uniaxial stiffness, $F/(H\varepsilon_{11})$, normalized by the Young's modulus E, plotted against H/d, for different microstructures. Since the the Young's modulus of the irregular structures differs by only a few percent from that of the regular hexagonal structure we used Young's modulus of the hexagonal structure to normalize all calculations:

$$E = \frac{4}{\sqrt{3}} E_s (t/l)^3 \frac{1}{1 + (5.4 + 1.5\nu_s)(t/l)^2}, \tag{2.15}$$

see also Gibson and Ashby [1997]. We detect a severe weakening in the small H/d regime for all microstructures, with the scatter being much larger for the rotated hexagonal microstructures (Fig. 2.13b) compared to the hexagons in the default orientation (Fig. 2.13c) and the Voronoi structures (Fig. 2.13a). Due to the boundary conditions, the cell walls located at the boundaries with a normal perpendicular to the direction of compression are stress free. In addition, the cells next to these stress free boundary layers are also less constrained than those away form the boundaries. The area fraction of this weak boundary layer, consisting of both the stress free cell walls and the less-constrained cells, is large when the height of the specimen is small, resulting in a decrease in the macroscopic stiffness. While the specimen size increases, the contribution of this weak boundary layer to the macroscopic stiffness

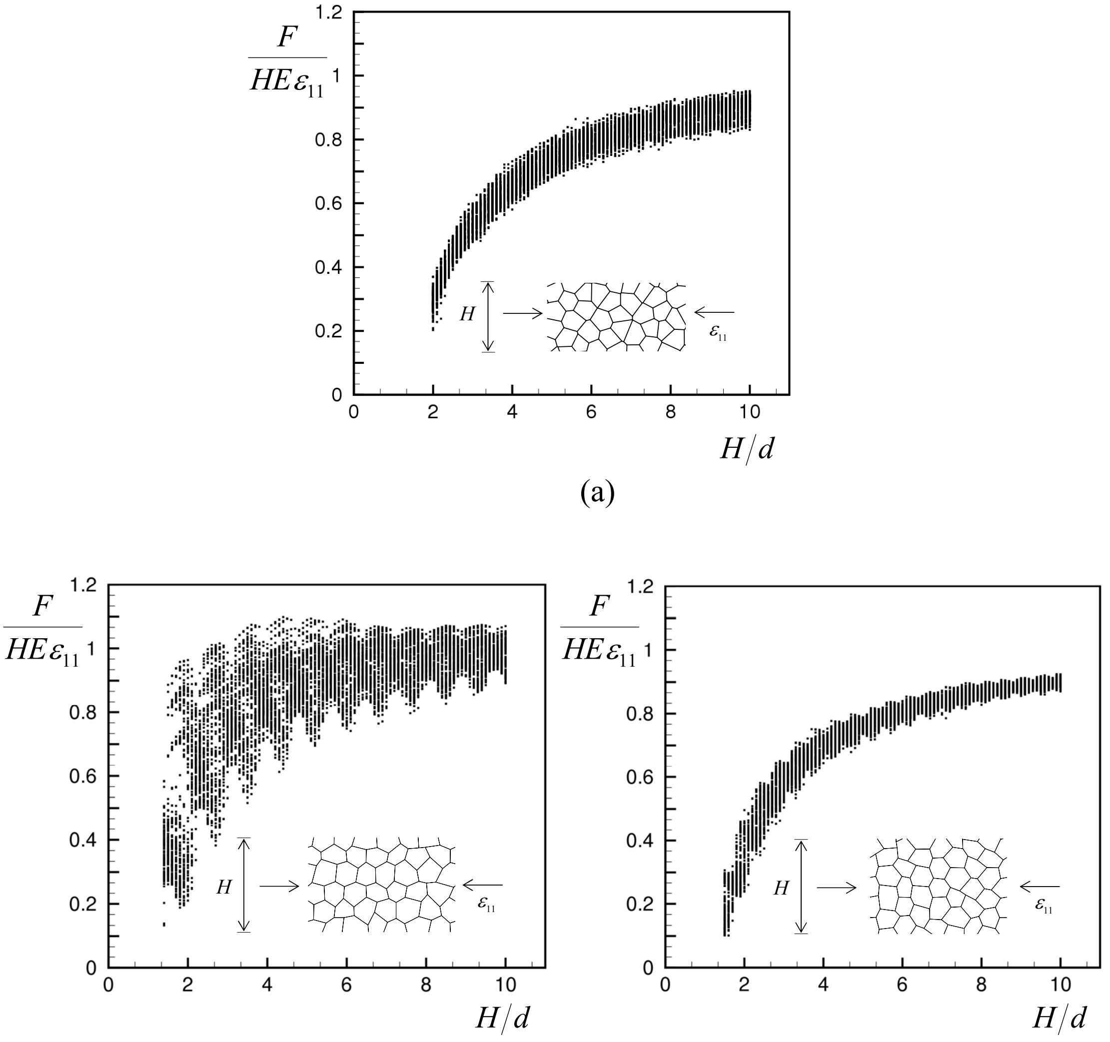

(a)

(b)

(c)

Figure 2.13: The calculated uniaxial compressive stiffness, $F/(H\varepsilon_{11})$, normalized by the Young's modulus *E*, plotted against *H*/*d*, for the: (a) Voronoi microstructure. (b) Perturbed hexagonal microstructure in the default orientation. (c) Perturbed hexagonal microstructure in the rotated orientation.

diminishes and the compressive stiffness converges to the classical (bulk) value. The number of load carrying cell wall members differs from one cut to another for the same height, which is the reason for the scatter in data. The largest possible distance between two subsequent load carrying cell edges is larger for the default orientation, and therefore the scatter in data is larger as well. In the case of Voronoi microstructures, we see that the scatter is relatively low, but it shows a tendency to slightly increase with increasing *H/d*, which is the opposite of what would be expected. The reason for this is explored below.

As mentioned before, taking a long structure ($L \approx 143d$) ensures that we have enough cells in the samples so that they represent the average characteristics of the microstructure analyzed, even for small *H/d* values. On the other hand, when the samples have a large aspect ratio, there is a small additional contribution of macroscopic bending to the overall compliance. Therefore, we also analyzed the effect of the aspect ratio on the stiffness. On one side we constrain the horizontal displacements, $u_1(x_1=0)=0$ (and the vertical displacements of one node to avoid rigid body translations), while we apply a horizontal displacement on the other side, $u_1(x_1=L)= -\varepsilon_{11}L$. Calculation of the overall stresses proceeds in a similar fashion as before. Figure 2.14a shows the calculated uniaxial stiffness, $F/(H\varepsilon_{11})$, normalized by the Young's modulus *E*, plotted against the aspect ratio *L*/*H*, for Voronoi microstructures with $H/d=3$. The solid line in Figure 2.14a passes through the average value for each aspect ratio. We see that the scatter in data is very large for small aspect ratios, whereas it converges for aspect ratios larger than 10. The sensitivity of the average value to the aspect ratio is much smaller; for aspect ratios of 1 and 5 the difference is about 10 percent, and for 2 and 5 it is about 5.5 percent. For aspect ratios larger than 5 the average value is almost the same. The average stiffness is always smaller than the corresponding bulk value (weakening behaviour) irrespective of the aspect ratio of the samples. The increase of the scatter in data for large thicknesses in case of Voronoi tessellations (see Fig. 2.13a) is associated with the fact that the length $L \approx 143d$ is kept constant while changing the thickness *H*, resulting in a decreasing aspect ratio with increasing thickness. Figure 2.14a clearly shows that a decreasing aspect ratio leads to an increasing scatter. Figures 2.14b, c and d show the calculated uniaxial stiffness, $F/(H\varepsilon_{11})$, normalized by the Young's modulus *E*, plotted against *H*/*d*, for structures with a fixed aspect ratio $L/H=2$ for Voronoi structures, perturbed hexagons in the default and the rotated orientations, respectively. By comparing Fig. 2.13 with Figure 2.14, we see that the conclusions drawn for structures with a fixed length ($L \approx 143d$, Fig. 2.13) still holds for structures with a fixed aspect ratio $L/H=2$ (Fig. 2.14), with the difference between the two being that for the latter case the scatter is larger and the average value is slightly shifted upwards.

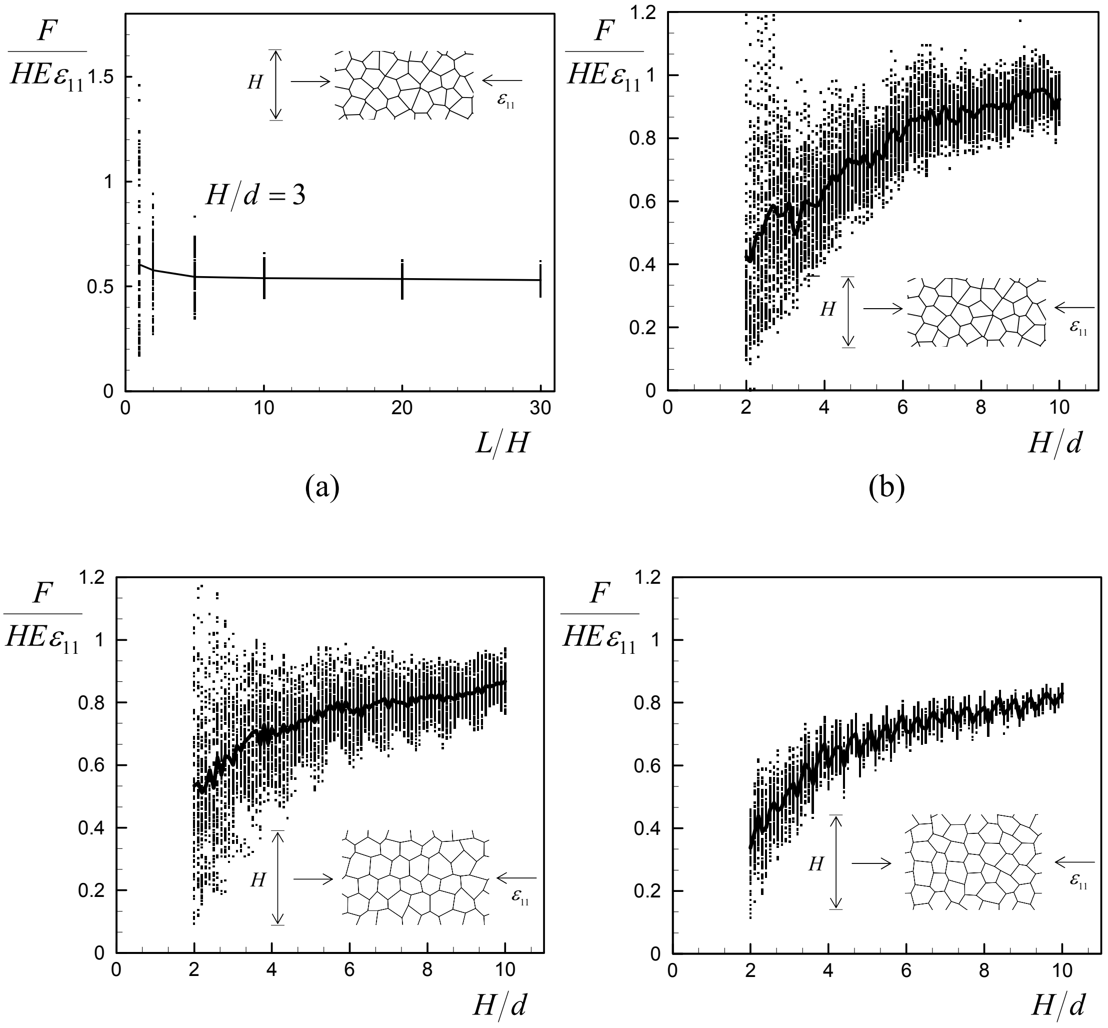

(a) (b)

(c) (d)

Figure 2.14: (a) The calculated uniaxial compressive stiffness, $F/(H\varepsilon_{11})$, normalized by the Young's modulus E, plotted against L/H, for the Voronoi microstructure with $H/d=3$. The calculated uniaxial compressive stiffness, $F/(H\varepsilon_{11})$, normalized by the Young's modulus E, plotted against H/d, for $L/H=2$, for the: (b) Voronoi microstructure. (c) Perturbed hexagonal microstructure in the default orientation. (d) Perturbed hexagonal microstructure in the rotated orientation.

2.3.3 Pure bending

The final boundary value problem that we solve is pure bending. The samples analyzed are similar to the one shown in Fig. 2.12. A pure bending state is achieved by fixing the left end and applying a macroscopic rotation at the right end. The

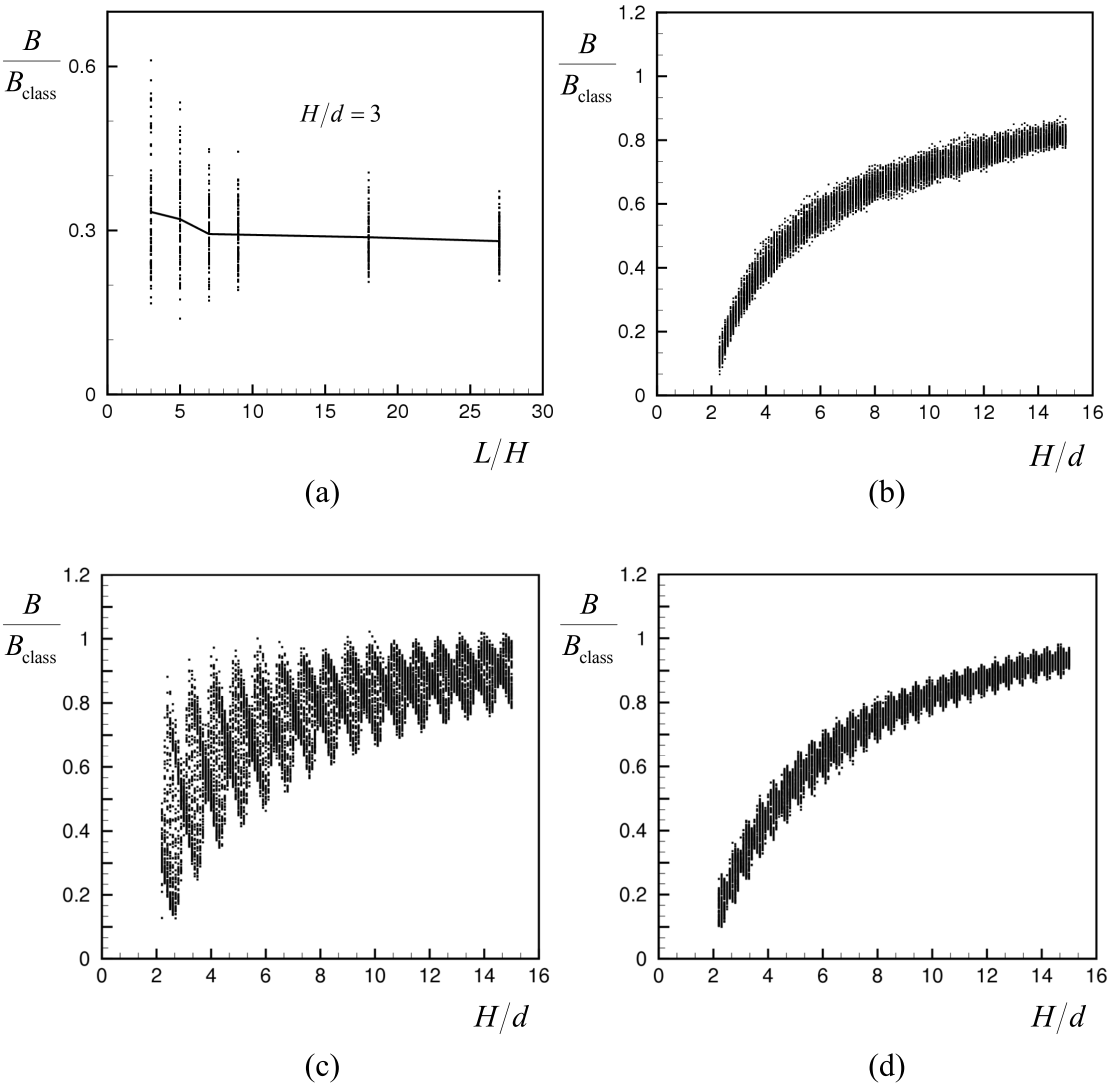

Figure 2.15: (a) The normalized macroscopic bending stiffness, B/B_{class}, plotted against L/H, for Voronoi microstructures with H/d=3. The normalized macroscopic bending stiffness, B/B_{class}, plotted against H/d, for the: (b) Voronoi microstructure. (c) Perturbed hexagonal microstructure in the default orientation. (d) Perturbed hexagonal microstructure in the rotated orientation.

macroscopic rotation is applied through a linearly varying displacement field over the sample height. The corresponding displacement and rotation boundary conditions at the cell walls read $u_1(x_1=0)=0$, $\phi_3(x_1=0)=0$ ($u_2=0$ for one node at $x_1=0$) and $u_1(x_1=L)=-cLx_2$. Here, x_2 is measured from the midsection of the structure and c is the curvature. The macroscopic moment is calculated from the reaction forces $f_1^{(k)}$ in the n cell walls at $x_1=L$ through

$$M = \sum_{k=1}^{n} f_1^{(k)} x_2^{(k)}. \tag{2.16}$$

The discrete bending stiffness B is calculated from M/c. The results are normalized with the classical bending stiffness of a dense sample with Young's modulus E and height H, defined as $B_{\text{class}} = EbH^3/12$ (b being the out-of-plane thickness). As in the previous section, E is taken to be the stiffness of a regular hexagonal structure, given in Equation (2.15). Figure 2.15a shows the effect of the aspect ratio on the macroscopic bending stiffness of Voronoi microstructures with $H/d = 3$. The scatter is larger for smaller aspect ratios. As it was the case for uniaxial compression, the sensitivity of the average value to the aspect ratio is very small; for aspect ratios of 3 and 7 the difference is about 12 per cent, and for aspect ratios larger than 7 the average value is almost the same. Although the sample will not be in pure bending for small aspect ratios, the results of Fig. 2.15a show that the effect of aspect ratio on the results is small. Figures 2.15b-d show the effect of specimen height on the bending stiffness for long, large-aspect-ratio samples ($L \approx 143d$) for Voronoi structures (Fig. 2.15b), and perturbed hexagonal microstructures in the default (Fig. 2.15c) and rotated orientation (Fig. 2.15d). There is a severe weakening in the small H/d regime similar to what we observed in the uniaxial compression test, and the value of the macroscopic bending rigidity converges to the classical value with increasing height. For a classical material, the material points located at the largest distance from the neutral axis would have the main contribution to the macroscopic bending stiffness. For the cellular microstructure, however, there are stress free boundaries and this causes a weakening in the bending rigidity, which is almost entirely due to the weakening in the macroscopic uniaxial stiffness. Indeed, the appearance of Fig. 2.15 is very similar to Fig. 2.13. Along these same lines, for materials which are size-independent under uniaxial loading, no size-effect is expected under bending. This is in accordance with the results for square lattices (analyzed in the Appendix) that, despite an increase in scatter, show a size-independent bending stiffness.

2.4 Conclusions

We analyzed size effects in the mechanical behaviour of cellular solids. To represent the cellular solids in two-dimensions, we used a large range of microstructures, both regular (squares and perfect hexagons) and irregular (perturbed hexagons and Voronoi tessellations). We performed simple shear, uniaxial compression and pure bending tests and analyzed the effect of the size of the samples, relative to the cell size. Figure 2.16 summarizes the effect of the specimen size on the macroscopic mechanical properties of cellular solids. We found that in simple shear the stiffness increases with decreasing sample height, while under uniaxial compression and in bending the overall (bending) stiffness decreases with decreasing specimen width. We relate these size effects to strong boundary layers in case of shear and weak boundary layers in case of uniaxial loading and bending.

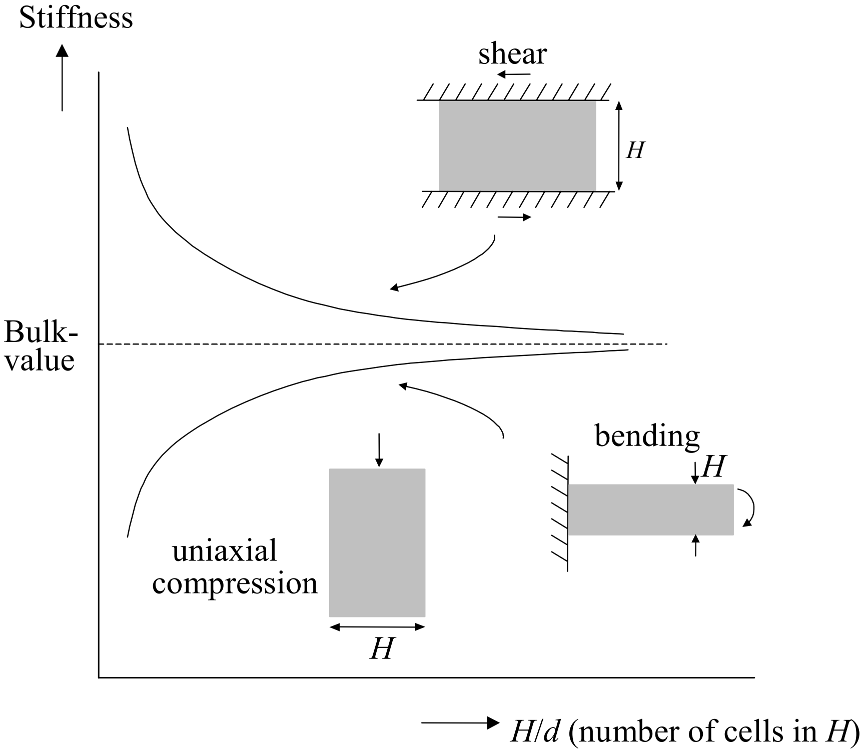

Figure 2.16: Summary of the size effects observed in the mechanical behaviour of cellular solids.

In simple shear, the cell walls connected at the top and the bottom boundaries are fully constrained, as a result of the bonding of the cellular material to the face sheets. The additional support gives rise to top and bottom regions that are stiffer than the interior regions of the material. The thickness of these strong layers depends on the boundary configuration (i.e., the length and the orientation of the cell walls at the boundaries), and we estimate them to be between 1 and 2 cell sizes. Therefore, the specimens with a small thickness, for which the area fraction of the strong boundary layers is large, have a larger macroscopic shear modulus compared to the classical (bulk) value. With the increasing specimen thickness, the area fraction of the strong boundary layers diminishes, and the macroscopic shear modulus converges to the classical value. We noted that for some boundary configurations, in case of regular microstructures, a weakening behaviour is also possible, which is related to the fact that we keep the density the same for every specimen cut. As a result some samples have a smaller cell wall thickness and weakening can occur.

In case of uniaxial compression, the cell walls at the free edge are stress free. In addition, the cells next to these cell walls have more freedom to deform and are therefore more compliant. These two phenomena, stress free cell walls and cells that are more compliant, are responsible for weak boundary layers parallel to the free edges. The contribution of these weak layers is large for small sample heights, leading to overall weakening. With increasing specimen height, the area fraction of the weak boundary layers diminishes, and the overall stiffness converges to the classical (bulk) value. Similar conclusions can be drawn for bending, leading to one weak boundary layer in tension and one in compression. The overall weakening due to the boundary layers is slightly larger in case of bending, due to the relatively large contribution of regions away from the neutral axis.

Typical for the results presented in this chapter is the presence of the scatter, which increases with decreasing specimen size. For the shear results the scatter clearly reflects the periodicity of the microstructure in case of squares and hexagons (see Fig. 2.11). By comparing the results for the hexagons in both orientations it can be observed that the average stiffening is approximately the same, but the appearance of the scatter is very different (see Figs. 2.11b and c). Due to the introduction of randomness the periodicity reduces (perturbed hexagons, Fig. 2.11d and e) and finally vanishes for fully random structures (Voronoi tessellations, Fig. 2.11f). Note that the amount of stiffening increases with randomness (Fig. 2.11). Similar conclusions with respect to the scatter can be drawn for uniaxial compression and bending: A large difference in scatter behaviour can be observed for the perturbed hexagons depending on orientation (see Figs. 2.13 and 2.15).

Appendix: Pure bending of square lattices

In this Appendix we analyze a long slender beam having a square cellular microstructure with cell size d. We do not cover the whole range of different cuts (as is done in section 2.3.3), but instead we test two extreme cases, Type A and Type B, having different lines of symmetry (see the inset of Fig. A1). The beam is in a pure bending mode having curvature c, so that the normal strain felt by the discrete members is $\varepsilon^{(k)} = -x_2{}^{(k)}c$, with $x_2{}^{(k)}$ being the distance of horizontal member (k) from the neutral axis. The effective moment follows from the normal forces $f_1{}^{(k)}$ in the horizontal members through

$$M = \sum_{k=1}^{n} f_1^{(k)} x_2^{(k)} = E_s btK \sum_{k=1}^{n} (x_2^{(k)})^2, \tag{A1}$$

so that the discrete bending stiffness for the Type A and Type B symmetries can be written as

$$B = 2E_s btd^2 \sum_{k=1}^{(n-1)/2} k^2, \tag{A2}$$

and

$$B = E_s btd^2 \sum_{k=1}^{(n-1)/2} (2k-1)^2, \tag{A3}$$

respectively. Here, n is the number of horizontal beams, related to the height of the beam, H/d, through

$$n = \begin{cases} \mathrm{mod}(\frac{H}{d}), & \text{for Type A} \\ \mathrm{mod}(\frac{H}{d}) + 1, & \text{for Type B} \end{cases} \tag{A4}$$

The discrete bending stiffness is compared to the continuum bending stiffness, B_{class}, obtained by multiplying the stiffness of an infinitely large square material, $E_s t/d$, by the moment of inertia of a dense comparison beam, $bH^3/12$. In Figure A1, the discrete bending stiffness, normalized by the continuum bending stiffness, is plotted against the normalized height. Although the results are sensitive to the symmetry-type (*A* or *B*) no clear trend can be observed. The scatter, which is partly due to the discreteness of the stiffness and partly due to the discreteness of the moment of inertia, increases with decreasing height. It should be noted that the cell wall thickness t for all the cuts was kept constant and equal to the cell wall thickness of an infinitely large structure with the same density. The effect of this on the results shown in Figure A1 is expected to be small.

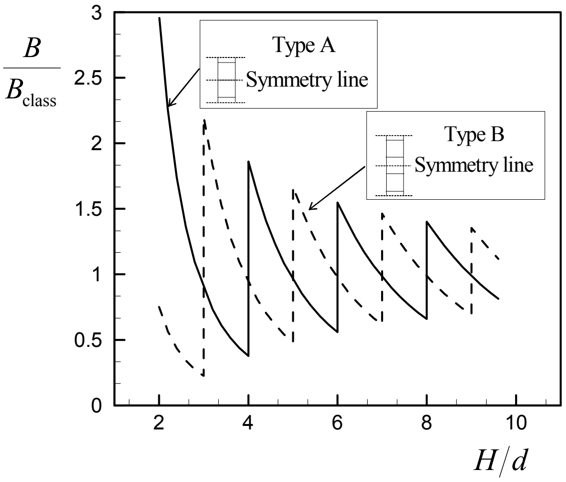

Figure A1: The normalized macroscopic bending stiffness, B/B_{class}, plotted against H/d for the square microstructure. Type A and Type B have different lines of symmetry.

3 Micropolar Modelling of Size Effects

In this chapter, we fit the elastic micropolar constants of the microstructures that we modelled discretely in chapter 2, by comparing the discrete and micropolar solutions for the simple shear problem in terms of the best agreement in the macroscopic shear stiffness. We develop a strain mapping procedure to be able to estimate the displacement and strain fields for the discrete calculations, and to compare the discrete and the analytical solutions for the local response under simple shear. Finally, we give the analytical solution for the pure bending problem of a plane-strain micropolar beam and critically address the limitations of the micropolar continuum theory.

3.1 Introduction

In the previous chapter, we have shown the size effects in the mechanical behaviour of two-dimensional cellular solids (i.e. honeycombs with square, hexagonal and Voronoi microstructures), for which we took the discreteness of the cellular morphology into account by modelling individual cell walls as beam elements. Although the mechanical properties calculated this way are in good agreement with experiments, this method is computationally expensive for more complex (especially three dimensional) microstructures. Another approach to account for these size effects is to use a generalised continuum theory. Here, we use the micropolar (Cosserat) theory for this purpose. For an overview of generalized continuum theories, including the micropolar theory, the reader is referred to chapter 1.

The elasticity matrix of a micropolar solid includes new constants relating microrotations to antisymmetric stresses, and couple stresses to curvatures (gradient of microrotations). In the literature, several homogenization/averaging techniques are proposed to obtain these constitutive coefficients for the micropolar theory. In most of these studies, cellular solids are represented by lattice frameworks (e.g. Aşkar and Çakmak [1968], Banks and Sokolowski [1968], Bazant and Christensen [1972], Ostoja-Starzewski *et al.* [1996], Adachi *et al.* [1998], Chen *et al.* [1998]). Micropolar homogenization approaches for irregular microstructures suffer from a dependence of the resulting effective constants on the specific choice of boundary conditions and RVE (representative volume element) size (e.g. Dendievel *et al.* [1998], Onck [2002]). Therefore, we do not use a homogenization technique, but instead, fit the elastic constants of the microstructures modelled discretely in chapter 2 by comparing the discrete solutions for the simple shear problem with the analytical micropolar solution, in terms of the best agreement in the macroscopic shear stiffness.

In section 3.2, we give the two-dimensional constitutive relations for micropolar solids. In section 3.3, we solve the simple shear problem for a micropolar continuum. After fitting the elastic constants of each microstructure in section 3.4.1, we develop a strain mapping procedure in section 3.4.2. In section 3.4.3, by means of this strain mapping procedure, we analyse the microrotation and strain fields for the discrete structures and compare them to the corresponding continuum fields of the micropolar theory. In section 3.5, we solve the pure bending problem of a plane-strain micropolar beam, and section 3.6 concludes this chapter by discussing the limitations of Cosserat-type continuum theories.

3.2 Constitutive equations

The three-dimensional elastic constitutive relations of a centro-symmetric micropolar (Cosserat) solid read

$$\sigma_{ij} = C_{ijkl}\gamma_{kl}, \qquad m_{ij} = D_{ijkl}k_{kl}. \tag{3.1}$$

For the most general case of a two-dimensional anisotropic micropolar solid, the in-plane elastic constitutive relations can be written in matrix-notation as

$$\begin{Bmatrix} \sigma_{11} \\ \sigma_{22} \\ \sigma_{12} \\ \sigma_{21} \\ m_{13} \\ m_{23} \end{Bmatrix} = \begin{bmatrix} C_{1111} & C_{1122} & C_{1112} & C_{1121} & 0 & 0 \\ C_{1122} & C_{2222} & C_{2212} & C_{2221} & 0 & 0 \\ C_{1112} & C_{2212} & C_{1212} & C_{1221} & 0 & 0 \\ C_{1121} & C_{2221} & C_{1221} & C_{2121} & 0 & 0 \\ 0 & 0 & 0 & 0 & D_{1313} & D_{1323} \\ 0 & 0 & 0 & 0 & D_{1323} & D_{2323} \end{bmatrix} \begin{Bmatrix} \gamma_{11} \\ \gamma_{22} \\ \gamma_{12} \\ \gamma_{21} \\ k_{13} \\ k_{23} \end{Bmatrix}, \tag{3.2}$$

and in terms of the symmetric and the antisymmetric stresses and strains as

$$\begin{Bmatrix} s_{11} \\ s_{22} \\ s_{12} \\ \tau_{12} \\ m_{13} \\ m_{23} \end{Bmatrix} = \begin{Bmatrix} A^{(1)}_{1111} & A^{(1)}_{1122} & A^{(1)}_{1112} & A^{(2)}_{1112} & 0 & 0 \\ A^{(1)}_{1122} & A^{(1)}_{2222} & A^{(1)}_{2212} & A^{(2)}_{2212} & 0 & 0 \\ \frac{1}{2}A^{(1)}_{1112} & \frac{1}{2}A^{(1)}_{2212} & A^{(1)}_{1212} & A^{(2)}_{1212} & 0 & 0 \\ \frac{1}{2}A^{(2)}_{1112} & \frac{1}{2}A^{(2)}_{2212} & A^{(2)}_{1212} & A^{(3)}_{1212} & 0 & 0 \\ 0 & 0 & 0 & 0 & D_{1313} & D_{1323} \\ 0 & 0 & 0 & 0 & D_{1323} & D_{2323} \end{Bmatrix} \begin{Bmatrix} \varepsilon_{11} \\ \varepsilon_{22} \\ \varepsilon_{12} \\ \beta_{12} \\ k_{13} \\ k_{23} \end{Bmatrix}, \tag{3.3}$$

where

$$\begin{gathered} s_{ij} = \frac{\sigma_{ij} + \sigma_{ji}}{2} \text{ and } \tau_{ij} = \frac{\sigma_{ij} - \sigma_{ji}}{2}, \\ \varepsilon_{ij} = \frac{\gamma_{ij} + \gamma_{ji}}{2} \text{ and } \beta_{ij} = \frac{\gamma_{ij} - \gamma_{ji}}{2} = \in_{ijk}(\omega_k - \phi_k), \end{gathered} \tag{3.4}$$

with $\omega_k = (\in_{ijk} u_{j,i})/2$ the classical macrorotation vector. By substituting $\sigma_{ij} = s_{ij} + \tau_{ij}$ and $\gamma_{ij} = \varepsilon_{ij} + \beta_{ij}$ into Equations (3.2) and solving for the symmetric (s_{ij}) and antisymmetric (τ_{ij}) stresses, the coefficients of Equations (3.3) are found in terms of those of Equations (3.2) as

$$
\begin{aligned}
&A^{(1)}_{1111} = C_{1111},\quad A^{(1)}_{1122} = C_{1122},\quad A^{(1)}_{1112} = C_{1112} + C_{1121},\\
&A^{(2)}_{1112} = C_{1112} - C_{1121},\quad A^{(1)}_{2222} = C_{2222},\quad A^{(1)}_{2212} = C_{2212} + C_{2221},\\
&A^{(2)}_{2212} = C_{2212} - C_{2221},\quad A^{(1)}_{1212} = \frac{C_{1212} + 2C_{1221} + C_{2121}}{2},\\
&A^{(2)}_{1212} = \frac{C_{1212} - C_{2121}}{2},\quad A^{(3)}_{1212} = \frac{C_{1212} - 2C_{1221} + C_{2121}}{2}.
\end{aligned}
\tag{3.5}
$$

According to the constitutive Equations (3.3), a two-dimensional anisotropic micropolar solid has 13 independent constants. The discrete structures analyzed in chapter 2 fall in two classes: in-plane orthotropic (the square structure) and in-plane isotropic (hexagons, perturbed hexagons and Voronoi structures). By incorporating the specific symmetries of these structures, it turns out that they can both be written as (Nowacki [1986], Dendievel *et al.* [1998], Wang and Stronge [1999], Warren and Byskov [2002])

$$
\begin{Bmatrix} s_{11} \\ s_{22} \\ s_{12} \\ \tau_{12} \\ m_{13} \\ m_{23} \end{Bmatrix}
=
\begin{bmatrix}
C_{1111} & C_{1122} & 0 & 0 & 0 & 0 \\
C_{1122} & C_{1111} & 0 & 0 & 0 & 0 \\
0 & 0 & A^{(1)}_{1212} & 0 & 0 & 0 \\
0 & 0 & 0 & A^{(3)}_{1212} & 0 & 0 \\
0 & 0 & 0 & 0 & D_{1313} & 0 \\
0 & 0 & 0 & 0 & 0 & D_{1313}
\end{bmatrix}
\begin{Bmatrix} \varepsilon_{11} \\ \varepsilon_{22} \\ \varepsilon_{12} \\ \beta_{12} \\ k_{13} \\ k_{23} \end{Bmatrix}.
\tag{3.6}
$$

For general in-plane orthotropic structures there are three independent classical constants, C_{1111}, C_{1122} and $A^{(1)}_{1212}$, while for in-plane isotropic structures only two of these are independent. In addition, there are two micropolar constants that need to be determined, $A^{(3)}_{1212}$ and D_{1313}. These constants must be larger than zero to satisfy positive definiteness of the strain energy density (Eringen [1999]).

In the following we will obtain closed-form expressions for the classical constants in terms of the microstructural parameters t (cell wall thickness), d (cell size), E_s (Young's modulus of the cell wall material) and ν_s (Poisson's ratio of the cell wall material). To do so, we start with the general expression of Hooke's law for an orthotropic linear elastic classical material:

$$\begin{Bmatrix} \varepsilon_{11} \\ \varepsilon_{22} \\ \varepsilon_{33} \\ \varepsilon_{12} \\ \varepsilon_{13} \\ \varepsilon_{23} \end{Bmatrix} = \begin{bmatrix} \frac{1}{E_1} & -\frac{\nu_{21}}{E_2} & -\frac{\nu_{31}}{E_3} & 0 & 0 & 0 \\ -\frac{\nu_{12}}{E_1} & \frac{1}{E_2} & -\frac{\nu_{32}}{E_3} & 0 & 0 & 0 \\ -\frac{\nu_{13}}{E_1} & -\frac{\nu_{23}}{E_2} & \frac{1}{E_3} & 0 & 0 & 0 \\ 0 & 0 & 0 & \frac{1}{2G_{12}} & 0 & 0 \\ 0 & 0 & 0 & 0 & \frac{1}{2G_{13}} & 0 \\ 0 & 0 & 0 & 0 & 0 & \frac{1}{2G_{23}} \end{bmatrix} \begin{Bmatrix} s_{11} \\ s_{22} \\ s_{33} \\ s_{12} \\ s_{13} \\ s_{23} \end{Bmatrix}, \tag{3.7}$$

with

$$\frac{\nu_{21}}{E_2} = \frac{\nu_{12}}{E_1}, \frac{\nu_{31}}{E_3} = \frac{\nu_{13}}{E_1}, \frac{\nu_{23}}{E_2} = \frac{\nu_{32}}{E_3}. \tag{3.8}$$

Throughout this thesis, the in-plane properties are those in the x_1-x_2 plane (as shown in Fig. 2.1), and the properties in the direction parallel to the axis of the prismatic cells, that is in the x_3 direction, are referred to as the out-of-plane properties. The Poisson's ratio ν_{ij} is defined as the negative of the normal strain in the j direction divided by the normal strain in the i direction, for normal loading in the i direction ($\nu_{ij} = -\varepsilon_{jj}/\varepsilon_{ii}$, no summation over the indices i and j).

For squares it can be deduced that

$$\begin{aligned} & E_1 = E_2 = E_s \frac{t}{d}, \quad E_3 = 2E_s \frac{t}{d}, \\ & G_{12} = \frac{1}{2} E_s \left(\frac{t}{d}\right)^3 \frac{1}{1+(2.4+1.5\nu_s)(t/d)^2}, \\ & \nu_{12} = \nu_{21} = 0, \quad \nu_{13} = \nu_{23} = 0.5\,\nu_s, \quad \nu_{31} = \nu_{32} = \nu_s, \end{aligned} \tag{3.9}$$

with d the length of an edge of a square and with shear deformations taken into account. The elastic constants of Equations (3.6) can be obtained in terms of the microstructural parameters (t, d, E_s, ν_s) by inverting Equations (3.7) after substituting Equations (3.9). Assuming plane stress conditions ($s_{33} = s_{13} = s_{23} = 0$), the elastic constants read

$$C_{1111} = E_s \frac{t}{d}, \quad C_{1122} = 0, \quad A^{(1)}_{1212} = 2G_{12} = E_s \left(\frac{t}{d}\right)^3 \frac{1}{1+(2.4+1.5\nu_s)(t/d)^2}. \tag{3.10}$$

Similarly, for plane strain ($\varepsilon_{33} = \varepsilon_{13} = \varepsilon_{23} = 0$):

$$
\begin{aligned}
&C_{1111} = E_\mathrm{s}\,\frac{t}{d}\,\frac{1-0.5\nu_\mathrm{s}^2}{1-\nu_\mathrm{s}^2}\,,\quad C_{1122} = E_\mathrm{s}\,\frac{t}{d}\,\frac{0.5\nu_\mathrm{s}^2}{1-\nu_\mathrm{s}^2}\,,\\
&A_{1212}^{(1)} = 2G_{12} = E_\mathrm{s}\left(\frac{t}{d}\right)^3 \frac{1}{1+(2.4+1.5\nu_\mathrm{s})(t/d)^2}\,.
\end{aligned}
\tag{3.11}
$$

The hexagonal microstructures (both regular and perturbed) and Voronoi tessellations are transverse isotropic, i.e., there is a plane of isotropy (the x_1-x_2 plane), but the material properties are not symmetric with respect to the out-of-plane, or transverse (x_3), direction. For transverse isotropy we can therefore write:

$$
\begin{aligned}
&E_1 = E_2 = E_\mathrm{p} && \text{(in-plane Young's modulus)}\\
&E_3 = E_\mathrm{t} && \text{(out-of-plane/transverse Young's modulus)}\\
&\nu_{12} = \nu_{21} = \nu_\mathrm{p} && \text{(in-plane Poisson's ratio)}\\
&\nu_{13} = \nu_{23} = \nu_\mathrm{pt} && \text{(Poisson's ratio associated with the effect of}\\
& && \text{an in-plane loading on the out-of-plane direction)}\\
&\nu_{31} = \nu_{32} = \nu_\mathrm{tp} && \text{(Poisson's ratio associated with the effect of an}\\
& && \text{out-of-plane loading on the in-plane direction).}
\end{aligned}
\tag{3.12}
$$

Because of symmetry, we have in addition:

$$
\frac{\nu_\mathrm{tp}}{E_\mathrm{t}} = \frac{\nu_\mathrm{pt}}{E_\mathrm{p}}. \tag{3.13}
$$

For the strain energy density to be positive definite, the elastic constants must satisfy (Hibbitt *et al.* [2001], Padovani [2002]):

$$
E_\mathrm{p},\, E_\mathrm{t} > 0, \quad \left|\nu_\mathrm{pt}\right| < (E_\mathrm{p} / E_\mathrm{t})^{1/2}, \quad \left|\nu_\mathrm{p}\right| < 1. \tag{3.14}
$$

Note that the in-plane Poisson's ratio ν_p can be larger than 0.5, which is not possible for isotropic materials. For the transverse isotropic microstructures that we analyzed, the main deformation mechanism is bending of cell walls in case of in-plane loading. When they are loaded in the out-of-plane direction, on the other hand, the cell walls deform by stretching, and consequently the out-of-plane Young's modulus (E_t) is much larger than the in-plane Young's modulus (E_p) (see also Table 2.1). As a consequence, the Poisson's ratio associated with the effects of the in-plane loads in the out-of-plane direction is very low, as shown by Gibson and Ashby [1997], and we take it to be zero:

$$\nu_{\mathrm{pt}} = \frac{E_{\mathrm{p}}}{E_{\mathrm{t}}} \nu_{\mathrm{s}} \approx 0. \tag{3.15}$$

Now, if we insert Equations (3.12) and (3.15) into Equations (3.7), assume plane strain and invert, the in-plane equations follow to be

$$\begin{Bmatrix} s_{11} \\ s_{22} \\ s_{12} \end{Bmatrix} = \frac{E_{\mathrm{p}}}{1-\nu_{\mathrm{p}}{}^2} \begin{bmatrix} 1 & \nu_{\mathrm{p}} & 0 \\ \nu_{\mathrm{p}} & 1 & 0 \\ 0 & 0 & (1-\nu_{\mathrm{p}}) \end{bmatrix} \begin{Bmatrix} \varepsilon_{11} \\ \varepsilon_{22} \\ \varepsilon_{12} \end{Bmatrix}, \tag{3.16}$$

which would be exactly the same if plane stress was assumed. Thus, for the case of $\nu_{\mathrm{pt}} = 0$, the plane-stress and plane-strain in-plane constitutive relations for a transverse isotropic solid are the same and given by (3.16). Comparison of (3.16) with (3.6) yields

$$C_{1111} = C_{2222} = \frac{E_{\mathrm{p}}}{1-\nu_{\mathrm{p}}^2}, \; C_{1122} = \frac{\nu_{\mathrm{p}} E_{\mathrm{p}}}{1-\nu_{\mathrm{p}}^2}, \; A_{1212}^{(1)} = \frac{E_{\mathrm{p}}}{1+\nu_{\mathrm{p}}}. \tag{3.17}$$

For the regular hexagonal structure, E_{p} and ν_{p} (taking shear deformations into account) can be directly written in terms of the microstructural parameters as (Gibson and Ashby [1997])

$$E_{\mathrm{p}} = \frac{4}{\sqrt{3}} E_{\mathrm{s}} (t/l)^3 \frac{1}{1+(5.4+1.5\nu_{\mathrm{s}})(t/l)^2}, \; \nu_{\mathrm{p}} = \frac{1+(1.4+1.5\nu_{\mathrm{s}})(t/l)^2}{1+(5.4+1.5\nu_{\mathrm{s}})(t/l)^2}. \tag{3.18}$$

For the irregular structures (perturbed hexagons and Voronoi structures) we will perform finite element calculations on large periodic unit-cells to obtain the elastic constants.

The in-plane constitutive equations for an isotropic and a transverse isotropic (with $\nu_{\mathrm{pt}} = 0$) micropolar solid can both be written in the form of Equation (3.6). For an isotropic material (with E and ν) in plane-strain, the coefficients in the first three equations of (3.6) read

$$C_{1111} = C_{2222} = \frac{E(1-\nu)}{(1+\nu)(1-2\nu)}, \; C_{1122} = \frac{E\nu}{(1+\nu)(1-2\nu)}, \; A_{1212}^{(1)} = \frac{E}{1+\nu}. \tag{3.19}$$

They can also be written in terms of the classical Lamé constants λ and μ (=G) as

$$C_{1111}=C_{2222}=\lambda+2\mu,\quad C_{1122}=\lambda,\quad A^{(1)}_{1212}=2\mu, \tag{3.20}$$

For isotropic materials the Lamé constants are related to Young's Modulus and Poisson's ratio as $\mu=E/2(1+\nu)$ and $\lambda=2E\,\nu/\{2(1+\nu)(1\text{-}2\nu)$. For transverse isotropic materials with $\nu_{pt}=0$ (see Equations (3.16)) the moduli can also be written in terms of 'in-plane' Lamé constants μ_{p} and λ_{p}, similar to Equations (3.20), with μ_{p} and λ_{p} defined as $\mu_{\mathrm{p}}=E_{\mathrm{p}}/2(1+\nu_{\mathrm{p}})$ and $\lambda_{\mathrm{p}}=2E_{\mathrm{p}}\nu_{\mathrm{p}}/\{2(1+\nu_{\mathrm{p}})(1\text{-}\nu_{\mathrm{p}})\}$. Therefore, if we know the solution of a plane-strain boundary value problem for an isotropic material expressed in terms of λ and μ, we can obtain the solution for a transverse isotropic material (with $\nu_{\mathrm{pt}}=0$) simply by substituting μ_{p} for μ and λ_{p} for λ. We will make use of this conversion at several places in the thesis.

3.3 Analytical solution of the simple shear problem

In this section, we analyze the simple shear of a sandwich panel having a micropolar material as a core (see also Diebels and Steeb [2002], Tekoğlu and Onck [2003a, b] and [2005]). The boundary conditions are similar as for the discrete structures analyzed in chapter 2, i.e. $u_1=-\gamma H$, $u_2=\phi_3=0$ at the top ($x_2=H$) and $u_1=u_2=\phi_3=0$ at the bottom ($x_2=0$). The panel is assumed to be infinitely wide in the horizontal (x_1) and out-of-plane (x_3) directions and is under a state of plane strain. For this situation the kinematic equations reduce to:

$$\begin{aligned}
&\varepsilon_{11}=0,\quad \varepsilon_{22}=u_{2,2},\\
&\varepsilon_{12}=\frac{1}{2}u_{1,2},\quad \beta_{12}=-\frac{1}{2}\left(u_{1,2}+2\phi_3\right),\\
&k_{13}=0,\quad k_{23}=\phi_{3,2},
\end{aligned} \tag{3.21}$$

while the equilibrium equations read

$$s_{12,2}-\tau_{12,2}=0,\quad s_{22,2}=0,\quad m_{23,2}+2\tau_{12}=0. \tag{3.22}$$

Inserting (3.21) into (3.22) via the constitutive equations (3.6), yields

$$\left(m+1\right)u_{1,22}+2m\phi_{3,2}=0, \tag{3.23}$$

$$u_{2,22}=0, \tag{3.24}$$

$$l_c^2 \phi_{3,22} - 2m\phi_3 - mu_{1,2} = 0, \tag{3.25}$$

with

$$l_c^2 = \frac{D_{1313}}{A^{(1)}_{1212}}, \quad m = \frac{A^{(3)}_{1212}}{A^{(1)}_{1212}}. \tag{3.26}$$

The parameter l_c is a material length, and it is often referred to as the characteristic length. The constant *m*, on the other hand, is a dimensionless term that can be seen as a coupling factor between the microrotation and macrorotation fields. For the limit $m \to \infty$, the micro- and macrorotation fields are fully coupled, and the micropolar theory reduces to the couple stress theory. We will explore the effect of the two higher order constants, *m* and l_c, in the following. The solution of the differential equations reads

$$u_2 = A_1 x_2 + A_2, \tag{3.27}$$

$$\phi_3 = C_1 + C_2 e^{\omega x_2} + C_3 e^{-\omega x_2}, \tag{3.28}$$

$$u_1 = C_4 - 2C_1 x_2 - PC_2 e^{\omega x_2} + PC_3 e^{-\omega x_2}, \tag{3.29}$$

with eigenvalue ω and coefficient *P* defined as

$$\omega = \frac{1}{l_c}\sqrt{\frac{2m}{m+1}}, \quad P = l_c\sqrt{\frac{2m}{m+1}}. \tag{3.30}$$

The remaining constants are determined by inserting the boundary conditions into the solutions (3.27), (3.28) and (3.29) and are given by

$$A_1 = A_2 = 0, \tag{3.31}$$

$$C_1 = \frac{\gamma H(e^{\omega H} - e^{-\omega H})}{2P(2 - e^{\omega H} - e^{-\omega H}) + 2H(e^{\omega H} - e^{-\omega H})}, \tag{3.32}$$

$$C_2 = -\frac{\gamma H(1 - e^{-\omega H})}{2P(2 - e^{\omega H} - e^{-\omega H}) + 2H(e^{\omega H} - e^{-\omega H})}, \tag{3.33}$$

$$C_3 = \frac{\gamma H(1-e^{\omega H})}{2P(2-e^{\omega H}-e^{-\omega H})+2H(e^{\omega H}-e^{-\omega H})}, \tag{3.34}$$

$$C_4 = -\frac{\gamma HP(2-e^{\omega H}-e^{-\omega H})}{2P(2-e^{\omega H}-e^{-\omega H})+2H(e^{\omega H}-e^{-\omega H})}. \tag{3.35}$$

The external work done by the surface tractions and couples can be calculated as shown on the left side of the virtual work expression (see Equation (1.3)). The microrotations and vertical displacements are zero on the surface, so that the surface couples Q_3 and vertical tractions t_2 do not contribute to the external work per unit-out-of-plane thickness, W^{ex}, which reduces to

$$W^{ex} = \int_S t_1 u_1 \, d\mathrm{S} = (\tau_{12} - s_{12}) L\gamma H = F\gamma H. \tag{3.36}$$

Here, F is the shear force per unit out-of-plane thickness and L the width of the sample (introduced to connect the continuum results of this chapter to the discrete results of the previous chapter). By substituting the constitutive equations (3.6), one can write

$$F = -LG\left(1+m\right)u_{1,2} = -LG\left(l_c^2 \phi_{3,22} + u_{1,2}\right), \tag{3.37}$$

where $A^{(1)}_{1212} = 2G$ has been substituted. In the second expression the boundary condition $\phi_3 = 0$ has been used, while for the third expression Equation (3.25) has been incorporated. These equations clearly emphasize the dependence on the two additional micropolar constants present in the theory. For classical elasticity we have $l_\mathrm{c} = m = 0$ and $u_{1,2} = -\gamma$, so that $F = LG\gamma$. This force will be used to normalize the results for the micropolar solid.

Figure 3.1a shows the normalized shear force (or normalized shear stiffness), $F/(LG\gamma)$, plotted against the relative specimen size, H/d, for different values of l_c/d and a fixed coupling factor ($m = 1$). For convenience we normalize H and l_c with the cell size d to facilitate comparison with the discrete results. For $l_\mathrm{c}/d \rightarrow 0$, the solution for the micropolar continuum theory reduces to the solution of the same problem in the classical continuum theory, irrespective of the coupling factor m. We see that with increasing l_c/d, the stiffening behaviour in the small H/d regime becomes more pronounced, and the convergence rate of the macroscopic shear stiffness, $F/(L\gamma)$, to the shear modulus, G, decreases. In the limiting case of $l_\mathrm{c}/d \rightarrow \infty$, it can be easily deduced from Equations (3.23), (3.24) and (3.25) that $u_2 = \phi_3 = 0$ and $u_1 = -\gamma x_2$ is the solution of the problem and that the normalized shear modulus does not depend on H

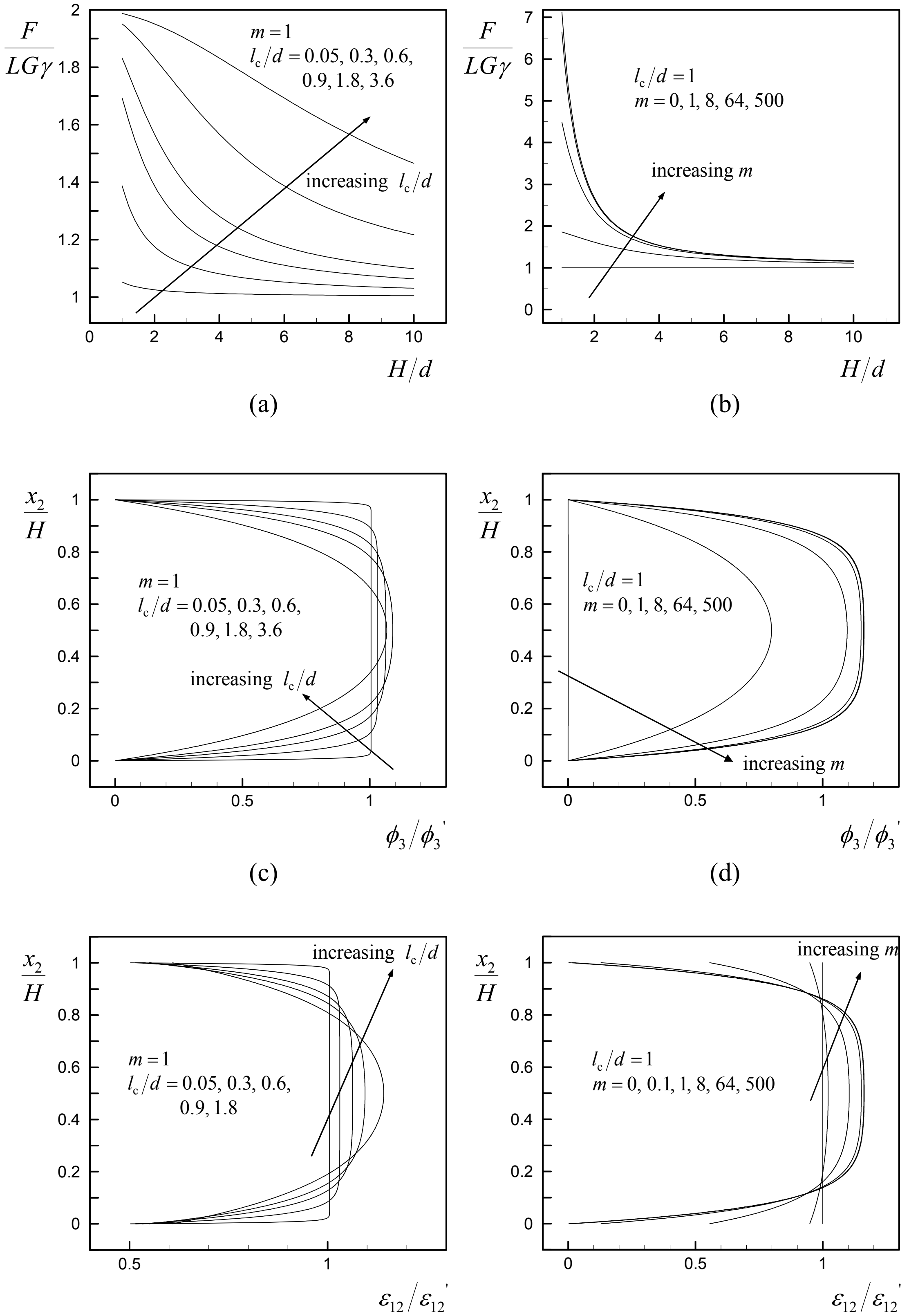
$\frac{F}{LG\gamma}$
$m=1$
$l_c/d = 0.05, 0.3, 0.6, 0.9, 1.8, 3.6$
increasing l_c/d
H/d
$\frac{F}{LG\gamma}$
$l_c/d = 1$
$m = 0, 1, 8, 64, 500$
increasing m
H/d
$\frac{x_2}{H}$
$m=1$
$l_c/d = 0.05, 0.3, 0.6, 0.9, 1.8, 3.6$
increasing l_c/d
ϕ_3/ϕ_3'
$\frac{x_2}{H}$
$l_c/d = 1$
$m = 0, 1, 8, 64, 500$
increasing m
ϕ_3/ϕ_3'
$\frac{x_2}{H}$
increasing l_c/d
$m=1$
$l_c/d = 0.05, 0.3, 0.6, 0.9, 1.8$
$\varepsilon_{12}/\varepsilon_{12}'$
$\frac{x_2}{H}$
increasing m
$l_c/d = 1$
$m = 0, 0.1, 1, 8, 64, 500$
$\varepsilon_{12}/\varepsilon_{12}'$

(a) (b)

(c) (d)

(e) (f)

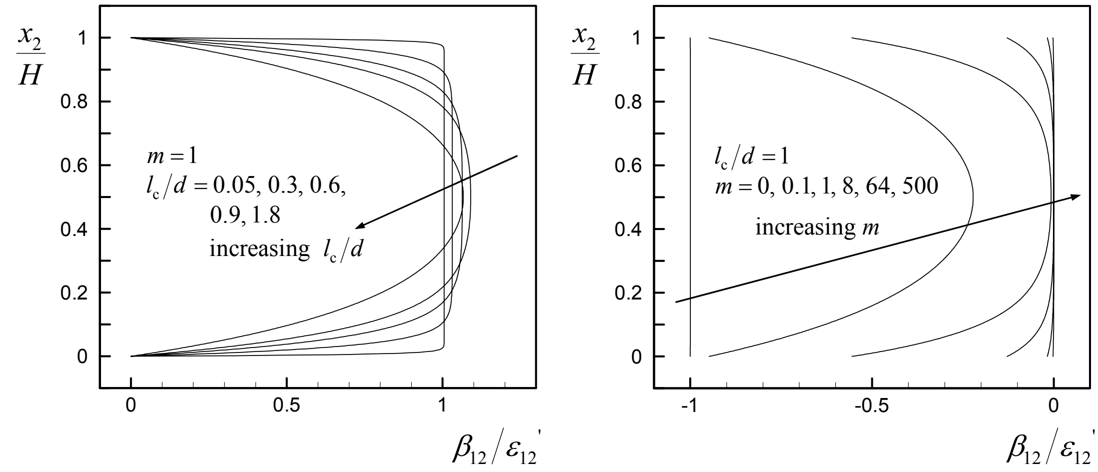

(g) (h)

Figure 3.1: (a) The normalized shear force (or normalized shear stiffness), $F/(LG\gamma)$, plotted against the relative specimen size, H/d, for different values of l_c/d and a fixed coupling factor ($m = 1$). (b) The effect of m on $F/(LG\gamma)$ plotted against H/d for $l_c/d = 1$. The normalized microrotation ϕ_3/ϕ_3' ($\phi_3' = \gamma/2$) through the thickness of a specimen with $H/d = 10$, for: (c) a fixed m and increasing l_c/d. (d) a fixed l_c/d and increasing m. The normalized symmetric shear strain $\varepsilon_{12}/\varepsilon_{12}'$ ($\varepsilon_{12}' = -\gamma/2$), through the thickness of a specimen with $H/d = 10$, for: (e) a fixed m and increasing l_c/d. (f) a fixed l_c/d and increasing m. The normalized antisymmetric strain $\beta_{12}/\varepsilon_{12}'$ ($\varepsilon_{12}' = -\gamma/2$), through the thickness of a specimen with $H/d = 10$, for: (g) a fixed m and increasing l_c/d. (h) a fixed l_c/d and increasing m.

and is given by $F/(LG\gamma) = 1 + m$ (see the second expression in (3.37)).

Figure 3.1b shows the effect of m on $F/(LG\gamma)$ plotted against H/d for $l_c/d = 1$. In this case, the stiffening behaviour in the small H/d regime becomes more and more pronounced as m approaches to the couple stress limit at $m \to \infty$. However, in contrast to Fig. 3.1a, the convergence rate of the shear stiffness to the classical shear modulus, G, increases with increasing m. For $m \to 0$, the macroscopic shear stiffness does not depend on H/d and is equal to the classical value $F/(LG\gamma) = 1$.

Next, we will explore the local fields through the thickness of the specimen, responsible for the overall behaviour shown in Figs. 3.1a and b. Figure 3.1c shows the normalized microrotation ϕ_3/ϕ_3' ($\phi_3' = \gamma/2$) through the thickness of a specimen with $H/d = 10$ and $m = 1$. A boundary layer is formed at the top and bottom, characterized by the constrained microrotations. The thickness of the boundary layer increases with increasing l_c/d. Figure 3.1d, on the other hand, shows that for a fixed l_c/d, the thickness of the boundary layer decreases with increasing m and converges to a thickness of approximately l_c for $m \to \infty$. Figures 3.1e and f show the normalized symmetric shear strain $\varepsilon_{12}/\varepsilon_{12}'$, through the thickness of the specimen, for a fixed m and increasing l_c/d, and for a fixed l_c/d and increasing m, respectively. Here ε_{12}' is the classical shear strain, given as $\varepsilon_{12}' = -\gamma/2$. Similar to the case of the normalized rotations, we see that for a fixed m (l_c/d) the thickness of the boundary layer increases (decreases) with increasing l_c/d (m).

Note that when l_c goes to zero (for fixed m) or when m goes to zero (for fixed l_c), the overall response is size-independent and the shear stiffness is equal to its classical counterpart (see Figs. 3.1a and b), while the symmetric shear strains are uniform over the thickness (see Figs. 3.1e and f) for both cases. However, these two cases are not equivalent as can be nicely exemplified by analyzing the antisymmetric strains β_{12} (see Figs. 3.1g and h). For the case of $m=0$, the microrotation field is not coupled with the displacement field (see Equations (3.23) and (3.25)). Incorporating the boundary conditions yields $\phi_3=0$ (see Fig. 3.1d) and $u_1=-\gamma x_2$ (or $\varepsilon_{12}=-\gamma/2$, see Fig. 3.1f). As a result, the antisymmetric shear strains are not zero as for the $l_c/d=0$ case (see Fig. 3.1g), but become equal to $\beta_{12}=\gamma/2$ (see Fig. 3.1h). For different boundary conditions for ϕ_3, however, the microrotation field throughout the specimen would be different, whereas the displacement field and the macroscopic shear stiffness would still coincide with their classical counterparts. The case of zero coupling, $m=0$, is analyzed by Lakes [1985] as well, for a quasistatic torsion problem of a circular cylindrical rod of an isotropic micropolar solid. He showed that for $m=0$, a given value of applied torque can be realized in more than one way by using different boundary conditions. This does not correspond to a failure of uniqueness in the usual sense, since different local boundary tractions are associated with different displacement and microrotation fields, even though the total microscopic load is the same. However, $m=0$ is a pathological case in the sense that the macroscopic end load does not uniquely determine the displacement and microrotation fields. Therefore, the classical elasticity is only recovered as a special case of the micropolar theory when both m and l_c vanish.

For the case of $m\rightarrow\infty$ (couple stress solution), the microrotations become equal to the macrorotations, $\phi_3=(u_{2,1}-u_{1,2})/2$, and the antisymmetric part of the shear strain vanishes (see e.g. Fig. 3.1h), so that the strain tensor becomes symmetric and equal to that in the classical continuum theory. The governing differential equations for the shear problem follow from combining Equations (3.23) and (3.25) and substituting $\phi_3=-u_{1,2}/2$, yielding

$$\frac{l_c^{\,2}}{2}\,u_{1,2222}-u_{1,22}=0, \tag{3.38}$$

supplemented by Equations (3.24), which stays the same. The external work done on the material per unit out-of-plane thickness reduces to

$$W^{ex}=\int_S t_1 u_1\; d\mathrm{S}=\gamma HGL\,\frac{l_c^{\,2}}{2}\,u_{1,222}\,. \tag{3.39}$$

Note that in the limit that l_c goes to zero, W^{ex} converges to $HGL\gamma^2$, the solution for the classical problem.

3.4 Comparison with the discrete results

In this section, we will compare the discrete results for the simple shear problem (see chapter 2) with the analytical solution for the micropolar continuum theory, and fit the micropolar constants, m and l_c, to give the best overall agreement. We will, in addition, develop a strain mapping procedure that enables a comparison between the discrete and continuum deformation fields.

3.4.1 Macroscopic response

Figures 3.2a-f show the best fit of the micropolar solution to the average value of the discrete results for the macroscopic shear stiffness, $F/(L\gamma)$, for the microstructures that we analyzed. To reflect the scatter, we plot the upper and lower bounds as well. For all cases, the couple stress solution ($m \to \infty$) gives the best agreement. We see that the characteristic length l_c depends on the cell orientation in the case of the perfect hexagonal microstructure ($l_c = 0.15d$ for the default and $l_c = 0.28d$ for the rotated orientations), whereas the difference is very small for the perturbed case ($l_c = 0.55d$ versus $l_c = 0.47d$). The stiffening behaviour is the largest for the Voronoi microstructure, followed by the square, perturbed hexagonal and perfect hexagonal microstructure, respectively, which is reflected in a larger value for the characteristic length l_c. Clearly, the characteristic length not only scales with the cell size, it also depends on the cellular morphology.

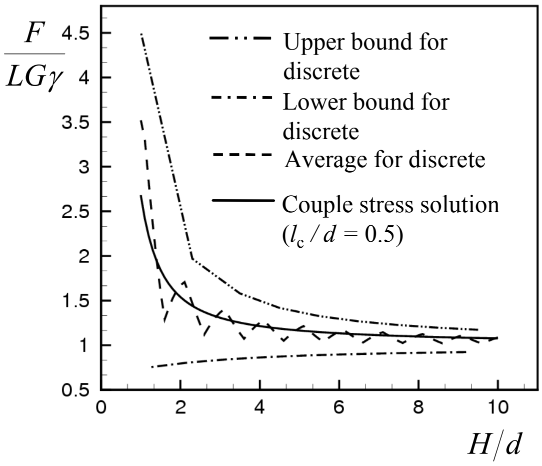

(a)

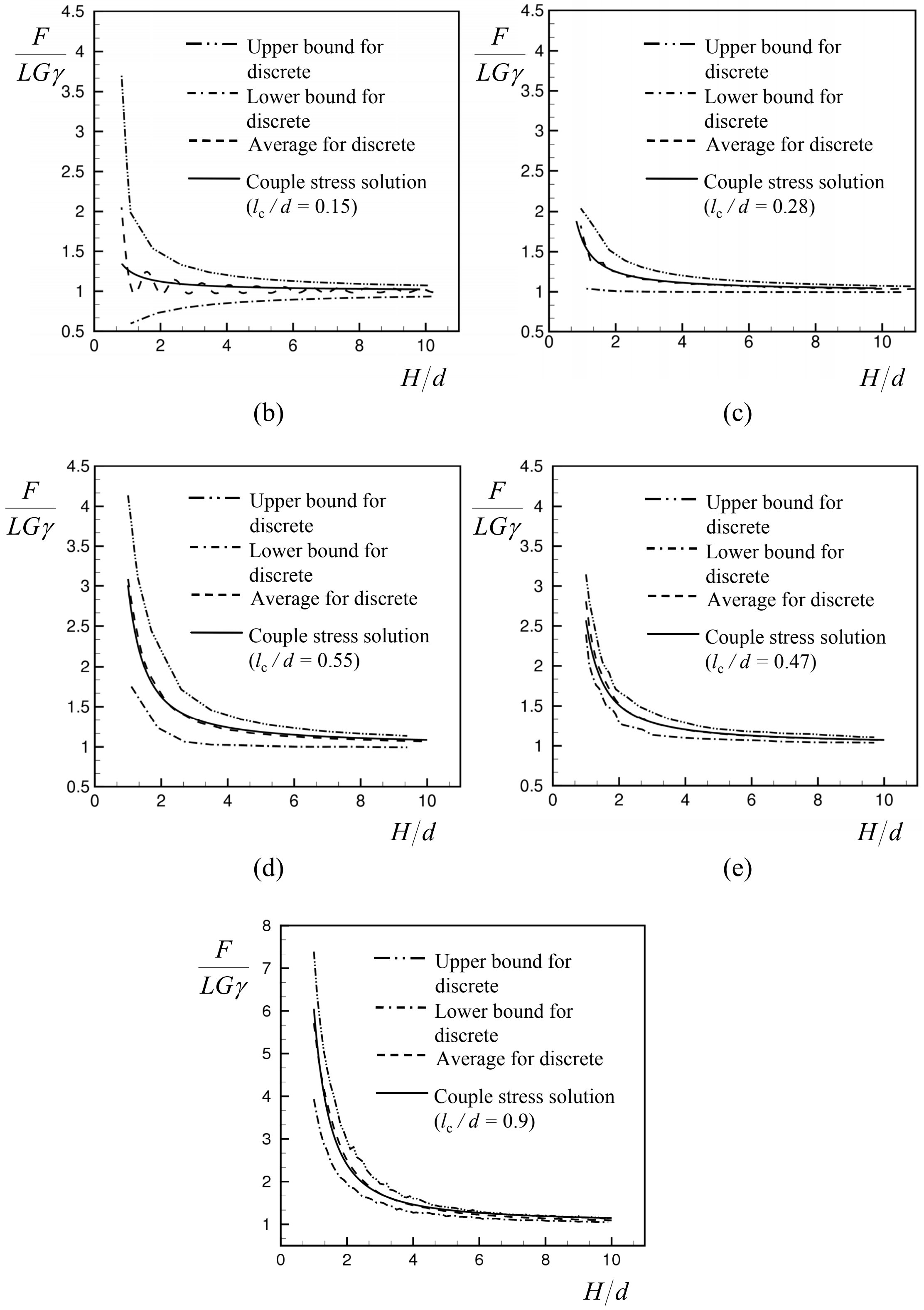

(b)

(c)

(d)

(e)

(f)

Figure 3.2: The best fit of the micropolar solution to the average value of the discrete results for the macroscopic shear stiffness, $F/(L\gamma)$, for the: (a) Square microstructure. (b) Perfect hexagonal

microstructure in the default orientation. (c) Perfect hexagonal microstructure in the rotated orientation. (d) Perturbed hexagonal microstructure in the default orientation. (e) Perturbed hexagonal microstructure in the rotated orientation. (f) Voronoi microstructure. For all cases, the couple stress solution ($m \to \infty$) gives the best agreement with the discrete results.

3.4.2 Strain mapping

In this section, we will develop a strain mapping procedure that will be used throughout the thesis for different boundary value problems. The finite element calculations performed on the discrete models (see chapter 2), provide the displacements and rotations of cell vertices, i.e. the locations at which the cell-walls meet. Figure 3.3, for instance, shows a Voronoi sample, indicated with red lines, having cell vertices that are indicated by black dots. We construct a square background grid (black dashed-lines), having grid nodes that are indicated with open squares. We take the average of the displacements and rotations at the cell vertices that are located inside a square, and assign these average values to each node of the square. Here, we only show a single sample for clarity, but in case there are multiple samples, the averaging is performed over the vertices of all the samples that are located in that square. If a node is shared by n squares, the values of the displacements and the rotations at that node are given by the arithmetic average of the values coming from each of these n squares. After finding the displacements and the rotations for each grid node, we divide each square in two triangles and calculate the strains for each triangle using standard finite element techniques. The strains within a triangle

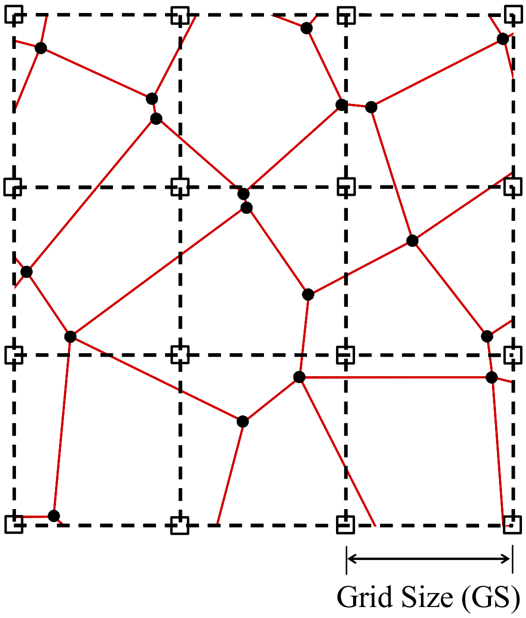

Figure 3.3: A square mesh for the strain mapping procedure plotted on top of a Voronoi sample.

with nodes p, r and q, respectively (numbered counterclockwise), are given as

$$\begin{Bmatrix} \varepsilon_{11} \\ \varepsilon_{22} \\ \varepsilon_{12} \end{Bmatrix} = \begin{bmatrix} N^p{}_{,1} & 0 & N^r{}_{,1} & 0 & N^q{}_{,1} & 0 \\ 0 & N^p{}_{,2} & 0 & N^r{}_{,2} & 0 & N^q{}_{,2} \\ \dfrac{N^p{}_{,2}}{2} & \dfrac{N^p{}_{,1}}{2} & \dfrac{N^r{}_{,2}}{2} & \dfrac{N^r{}_{,1}}{2} & \dfrac{N^q{}_{,2}}{2} & \dfrac{N^q{}_{,1}}{2} \end{bmatrix} \begin{Bmatrix} u_1^p \\ u_2^p \\ u_1^r \\ u_2^r \\ u_1^q \\ u_2^q \end{Bmatrix}, \tag{3.40}$$

where N^i ($i = p, r, q$) are the shape functions for a constant strain triangle (see Zienkiewicz and Taylor [2000]). Finally, the strains within a square are obtained by taking the average of the two triangles.

The accuracy and the scatter in the estimated displacement and strain fields depend, obviously, on the number of samples (NS) included in the strain mapping procedure. The samples that we analyze are cut from a large block of material, and each one of them corresponds to a different boundary configuration and cell distribution. The difference between two samples depends on the cutting step size (CSS, see section 2.3.1) and we will see that this affects the number of samples required for a converged displacement or strain field. The grid size (GS), i.e. the length of the edge of a square of the background grid (see Fig. 3.3), plays an important role as well. In the following, we explore the effect of these parameters on the strain maps of a uniaxial strain field.

Figure 3.4a shows a Voronoi sample with a length of 40d and a height of 24d. The sample is compressed in the x_1-direction by prescribing symmetry conditions at the left and a uniform horizontal displacement field at the right. Figures 3.4b, c and d show the strain field ε_{11} normalized with the applied strain $\varepsilon_{\text{appl}}$ for the sample of Fig. 3.4a, for 25 samples, and for 200 samples, respectively. The grid size is taken to be equal to the average cell size and the cutting step size to half a cell size ($\text{GS} = d$ and $\text{CSS} = d/2$). We see that in the case of a single sample, there are large fluctuations in the value of ε_{11} (Fig. 3.4b), whereas with increasing number of samples the fluctuations decrease (Fig. 3.4c), resulting in a smooth field for 200 samples (Fig. 3.4d). It can be observed that the strain is underestimated in an edge layer parallel to the left and right boundaries. To investigate whether these layers are a consequence of the strain mapping procedure or related to the discrete behaviour of the cellular material, we applied the strain mapping procedure to a linearly increasing displacement-field. The same edge layers were observed as for the discrete structure (Fig. 3.4d). The underlying reason of this behaviour is that the squares located at the left (right) boundary share only their right-side (left-side) nodes with other squares. As a result, the displacements are almost the same for all nodes and consequently, the

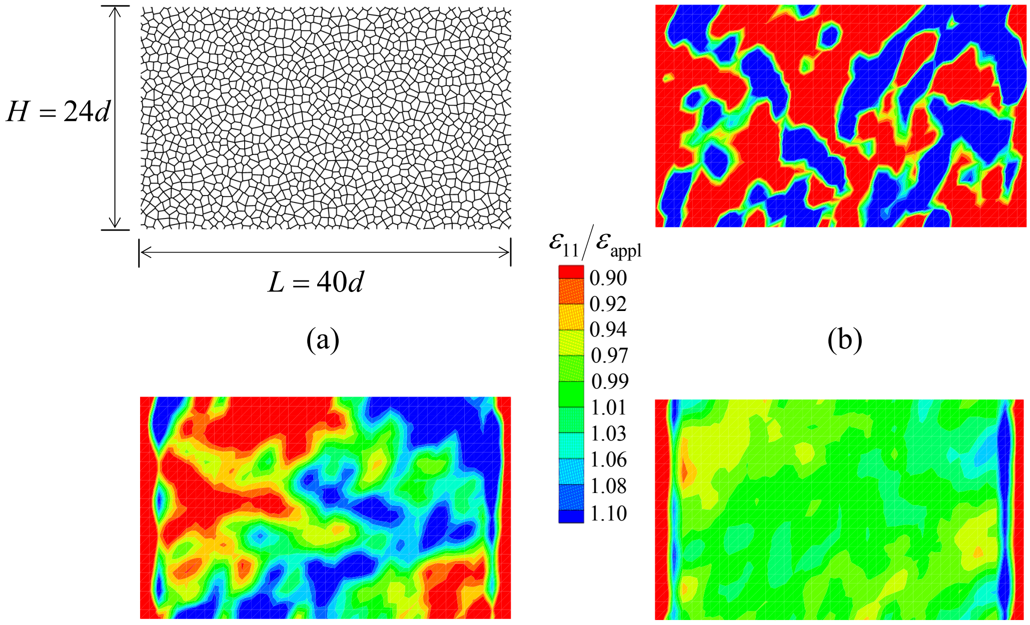

(a) (b) (c) (d)

Figure 3.4: (a) A Voronoi sample with a length of 40*d* and a height of 24*d*. The strain field ε_{11} normalized with the applied strain $\varepsilon_{\text{appl}}$ for: (b) the sample shown in (a). (c) 25 samples. (c) 200 samples.

strains are much lower for these elements. This is a bias of the strain mapping algorithm and results in edge layers with a thickness on the order of the grid size. Note that this artefact does not develop at the top and bottom, where the strain ε_{11} is calculated from the displacement gradients in a direction parallel instead of perpendicular to the edges.

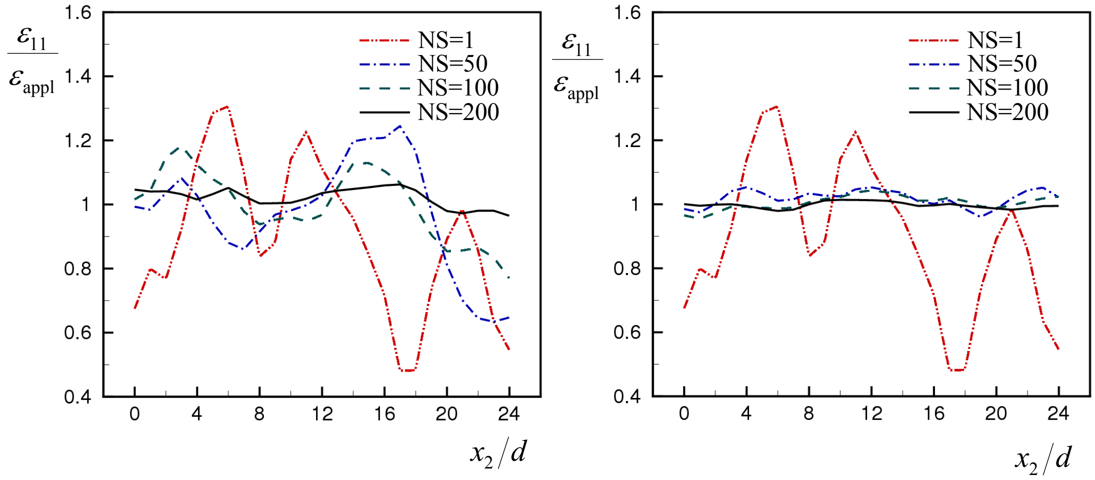

(a) (b)

Figure 3.5: The effect of the number of samples NS on the normalized strain $\varepsilon_{11}/\varepsilon_{\text{appl}}$, plotted through the thickness at the line $x_1 = L/2$, for a cutting step size (CSS) of (a) *d*/10. (b) *d*/2.

Figures 3.5a and b show the normalized strain $\varepsilon_{11}/\varepsilon_{\mathrm{appl}}$ through the thickness at the line $x_1 = L/2$, for a cutting step size (CSS) of $d/10$ and $d/2$, respectively. In both cases, the fluctuations in the $\varepsilon_{11}/\varepsilon_{\mathrm{appl}}$ value decreases with increasing number of samples NS, as it would be expected. The convergence rate, however, is much larger for the case of CSS = $d/2$: The field averaged over 50 samples (NS = 50) for CSS = $d/2$ (Fig. 3.5b) is almost the same as the field averaged over 200 samples (NS = 200) for CSS = $d/10$ (Fig. 3.5a).

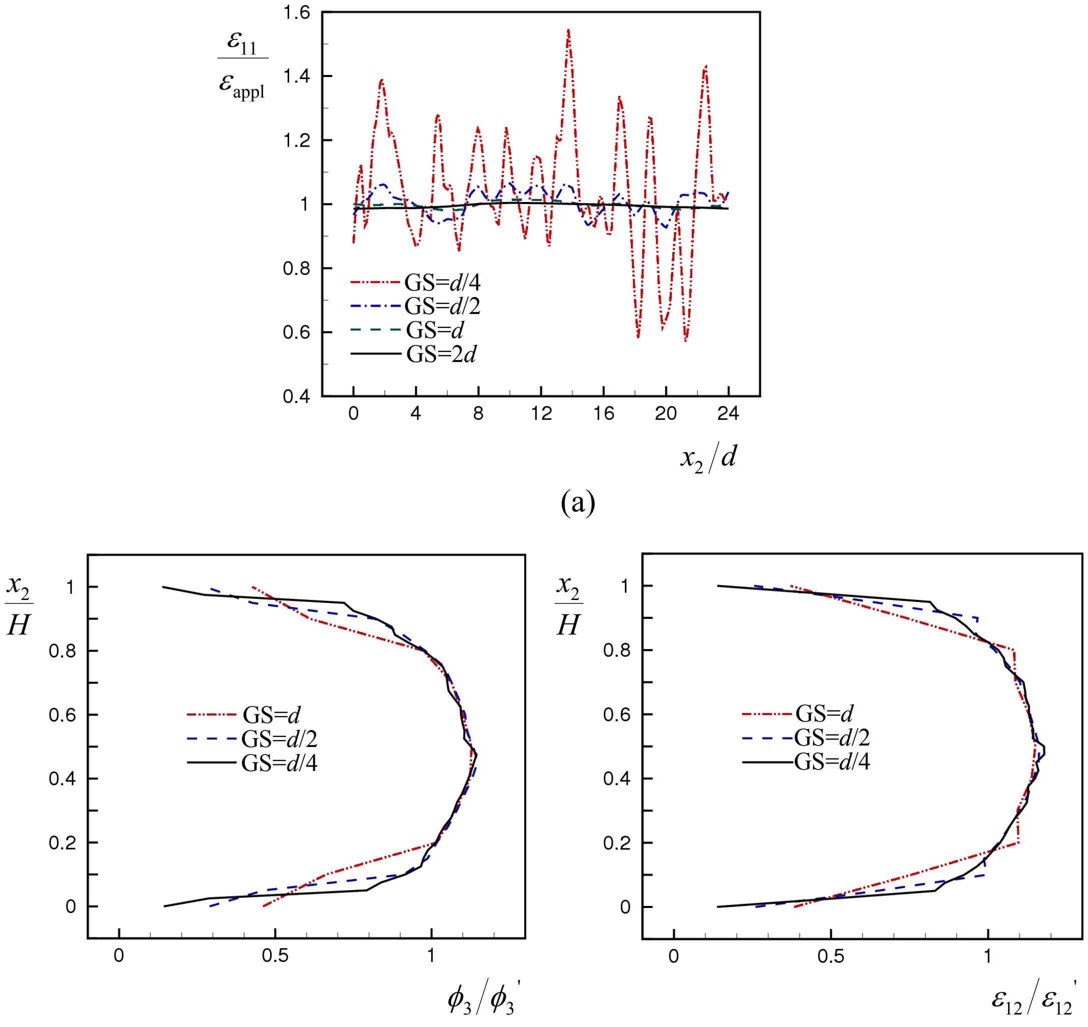

(a)

(c) (d)

Figure 3.6: (a) The effect of the grid size GS on the normalized strain $\varepsilon_{11}/\varepsilon_{\mathrm{appl}}$, plotted through the thickness at the line $x_1 = L/2$ for CSS = $d/2$ and NS = 200. The normalized rotation ϕ_3/ϕ_3' ($\phi_3' = \gamma/2$) (b) and the normalized shear strain $\varepsilon_{12}/\varepsilon_{12}'$ ($\varepsilon_{12}' = -\gamma/2$) (c) through the thickness, for samples with $H = 10d$ and $L = 100d$.

Figure 3.6a shows the effect of the grid size GS on the normalized strain $\varepsilon_{11}/\varepsilon_{\mathrm{appl}}$, plotted through the thickness at the line $x_1 = L/2$ for CSS = $d/2$ and NS = 200.

The results are as expected: The larger the grid size, the smoother the strain field. However, to be able to capture the gradients in the field variables, the grid size should be small enough. To investigate that, we plot the rotations and strains through the thickness for the Voronoi samples tested in shear in chapter 2 (section 2.3.1, Fig. 2.11f). Figures 3.6b and c show the normalized rotation $\phi_3/\phi_3^{'}$ ($\phi_3^{'}=\gamma/2$) and the normalized shear strain $\varepsilon_{12}/\varepsilon_{12}^{'}$ ($\varepsilon_{12}^{'}$=-$\gamma/2$), respectively, through the thickness, for samples with $H=10d$ and $L=100d$. The rotation ϕ_3 and the shear strain ε_{12} corresponding to an x_2 coordinate are the average values over all the nodes with the same x_2 coordinate along the length L of the samples. We see that the gradients near the top and bottom boundaries can be better picked up with small grid sizes, at the expense of an increased scatter in the central region.

We can summarize the effects of the different strain mapping parameters as follows.

- The number of samples (NS) should be large enough to smooth out the fluctuations in the field variables. An increase in the cutting step size (CSS) can significantly reduce the number of samples NS required for a converged solution.
- The optimal grid size (GS) is the one that is small enough to capture the gradients in non-uniform regions and large enough to provide relatively smooth fields in uniform regions.

3.4.3 Local response

In section 3.4.1 we found that the best fit to the global results (i.e. the macroscopic stiffness) was made by the couple stress theory ($m\rightarrow\infty$). Each specific cellular microstructure resulted in a specific value for the characteristic length, which turned out to be on the order of the cell size (ranging from $l_c=0.15d$ to $0.9d$). In this section, our aim is to see how accurate the corresponding local continuum fields correspond to the discrete results. To do so, we analyze the normalized rotations $\phi_3/\phi_3^{'}$ ($\phi_3^{'}=\gamma/2$) and the normalized shear strains $\varepsilon_{12}/\varepsilon_{12}^{'}$ ($\varepsilon_{12}^{'}=-\gamma/2$) through the thickness of samples with height $H=5d$ and $10d$.

Figures 3.7a and b show the normalized microrotation $\phi_3/\phi_3^{'}$ for the square microstructure (corresponding to Fig. 3.2a). To accurately account for the fields we repeated the calculations from chapter 2 using a smaller step size, CSS$=d/10$ instead of $d/5$. The discrete data correspond to the rotations of cell vertices (i.e. the locations where four cell walls meet). The fit is very good for both sample thicknesses. These figures clearly show that the thickness of the strong boundary layers located at the top and bottom of the samples is the same for both sample heights, approximately one cell size. As a result, the ratio of the boundary layer thickness to the total specimen thickness is smaller for the $H=10d$ case (Fig. 3.7b), explaining why the stiffening for the $H=10d$ case is lower as well (cf. Fig. 3.2a).

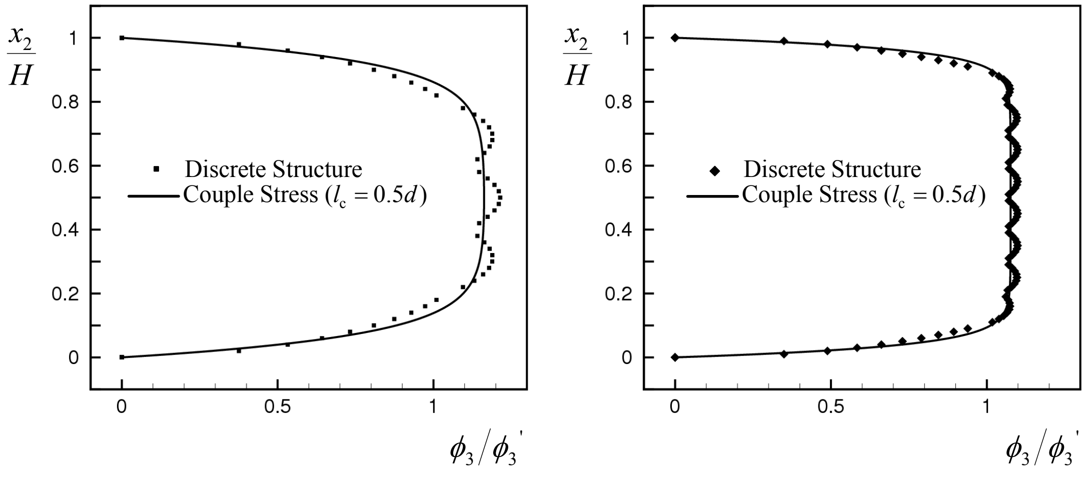

(a) (b)

Figure 3.7: The normalized rotation ϕ_3/ϕ_3' ($\phi_3' = \gamma/2$) for the square microstructure with: (a) $H=5d$. (b) $H=10d$.

Figures 3.8a (c) and b (d) show the normalized microrotation ϕ_3/ϕ_3' (the normalized shear strain $\varepsilon_{12}/\varepsilon_{12}'$) through the thickness, for the Voronoi microstructures with $H=5d$ and $H=10d$, respectively. The discrete data is obtained by applying the strain mapping procedure as explained in section 3.4.2 with NS = 100 and GS = d/2 (note that the 100 samples were cut with CSS = d/10). For the microrotation, only the average value at each x_2-coordinate is shown (dashed lines in Figs. 3.8a and b), whereas for the shear strain (Figs. 3.8c and d), all values at the nodes with the same x_2-coordinate are shown in addition to the averages. We see that the couple stress theory is able to nicely pick up the local fields and the boundary layer thickness for each case. For both the rotations and strains for the $H/d=5$ case the average discrete fields are slightly overestimated, although the continuum solution is

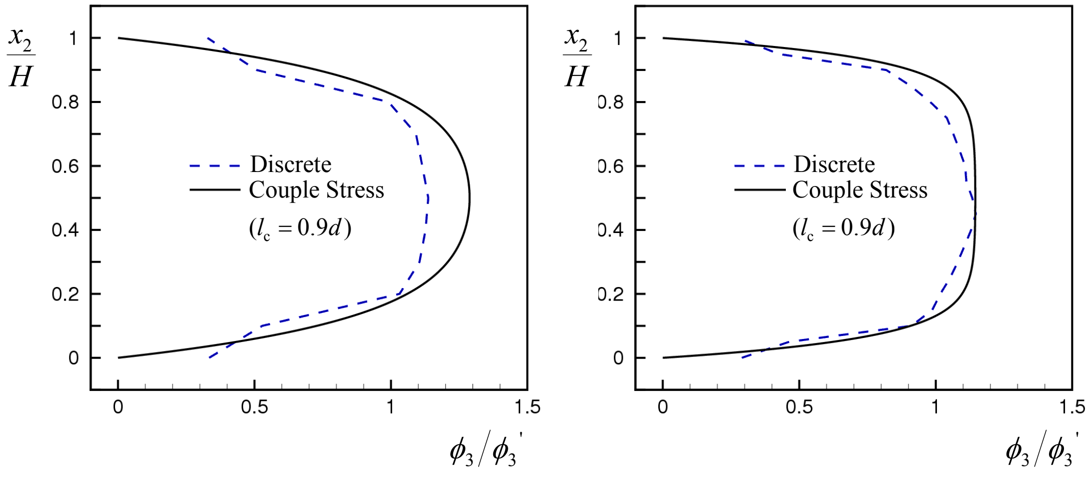

(a) (b)

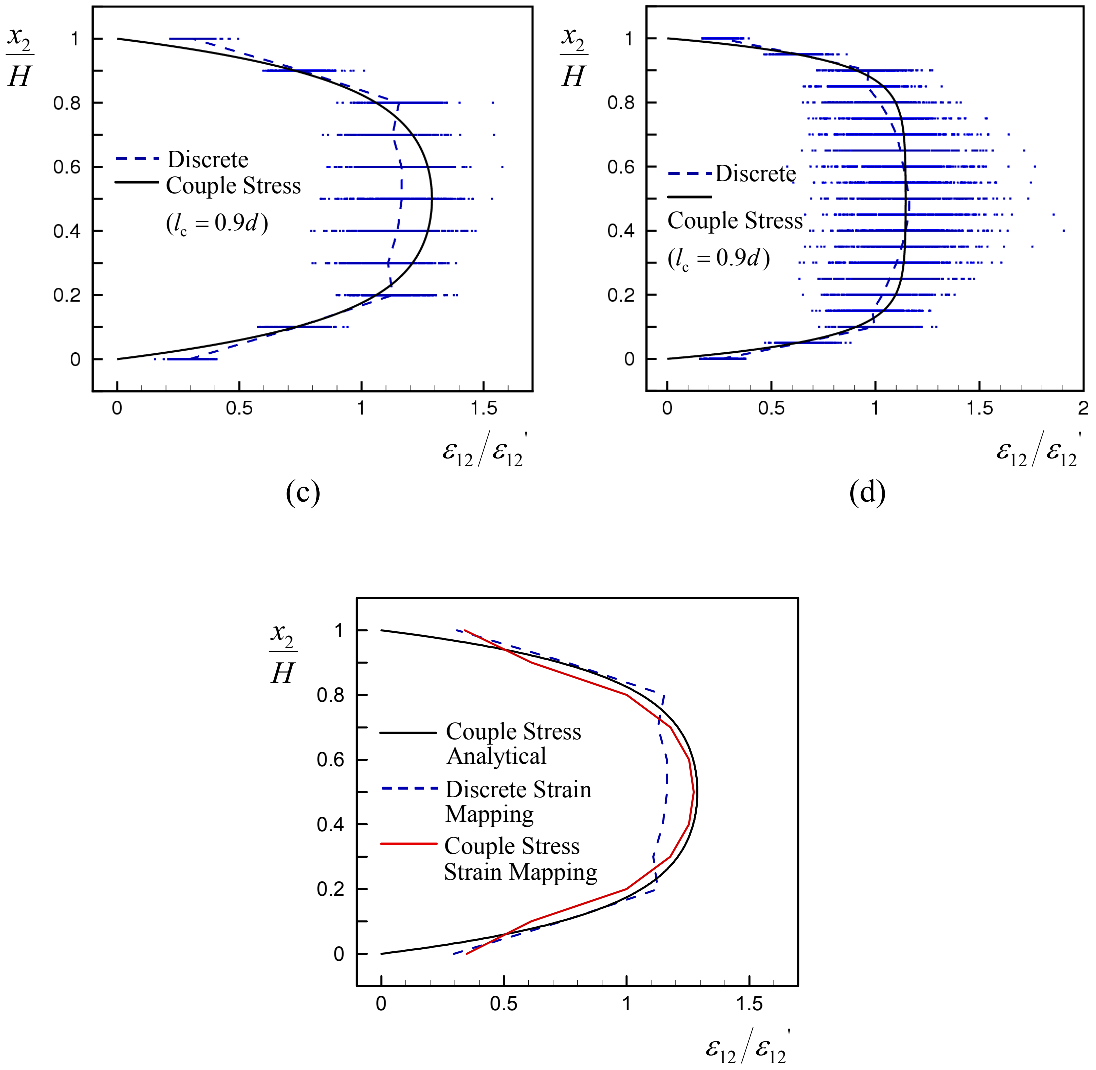

(c) (d)

(e)

Figure 3.8: The normalized rotation ϕ_3/ϕ_3' ($\phi_3' = \gamma/2$) through the thickness, for the Voronoi microstructures with: (a) $H = 5d$. (c) $H = 10d$. The normalized shear strain $\varepsilon_{12}/\varepsilon_{12}'$ ($\varepsilon_{12}' = -\gamma/2$) through the thickness, for the Voronoi microstructures with: (b) $H = 5d$. (d) $H = 10d$. (e) Comparison of the strain maps for the couple stress solution ($l_c/d = 0.9$) and discrete analyses with the best fit for the couple stress theory for Voronoi tessellations. All the strain maps are for a grid size GS = $d/2$.

well located within the scatter band of the discrete results. For the $H/d = 10$ case, the agreement is very good. To investigate the role of the strain mapping procedure in the discrepancy between the discrete and continuum solution for the $H/d = 5$ case, strain maps are constructed of the analytical (exact) displacement fields. As input for the strain map procedure we take the displacement values given by the analytical solution at the locations of the grid points for a grid size GS = $d/2$. Figure 3.8e shows that the strain map for the analytical solution overestimates the field variables in the boundary layers as well. In addition, the analytical strain map slightly underestimates the analytical shear strains in the central (core) region. Thus, the difference between the discrete and couple stress results is partly due to the inaccuracy in the strain mapping procedure, and partly due to the inaccuracy in the couple stress prediction.

3.5 Analytical solution of the pure bending problem

In this section, we will solve the pure bending problem of a straight plane-strain beam (i.e. a plate that is infinitely wide in the out-of-plane direction) for an isotropic, centro-symmetric micropolar material. The midplane of the plate is set as the x_1-x_3 plane, the x_3 direction coinciding with the out-of-plane direction. The pure bending assumption states that "transverse plane sections (that are parallel to the x_2-x_3 plane, in our case) remain plane and normal to the longitudinal fibres", see Fig. 3.9.

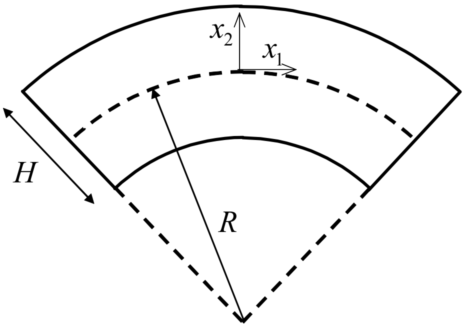

Figure 3.9: Notation and geometry of the plane-strain pure bending problem.

The most general displacement field that satisfies this can be written as

$$u_1 = \frac{1}{R} x_1 x_2, \ u_2 = -\frac{1}{2R} x_1^2 + f(x_2) + P, \ u_3 = 0, \tag{3.41}$$

where R is the radius of curvature, f a function of x_2 alone and P is an integration constant. The kinematic equations reduce to:

$$\begin{aligned} &\varepsilon_{11} = \frac{1}{R} x_2, \quad \varepsilon_{22} = f_{,2}, \quad \varepsilon_{12} = 0, \\ &\beta_{12} = -\left(\frac{1}{R} x_1 + \phi_3 \right), k_{13} = \phi_{3,1}, \ k_{23} = \phi_{3,2}, \end{aligned} \tag{3.42}$$

while the equilibrium equations are similar to the shear problem and given in Equations (3.22). Since the shear strains ε_{12} are zero, the first equilibrium equation (Equation 3.22a) combined with the constitutive behaviour (see Equations (3.6)) and the kinematics states that k_{23} must vanish. As a result, the third equilibrium equation (Equation 3.22c) corresponds to $\tau_{12}=\beta_{12}=0$, so that the only expression for the microrotations that satisfies equilibrium is given by

$$\phi_3 = -\frac{1}{R}x_1. \tag{3.43}$$

Finally, from the second equilibrium equation (Equation 3.22b) and the requirement that the surface tractions t_i and surface couples Q_i must vanish at the top and bottom, the remaining unknowns in Equations (3.41) can be determined, yielding

$$u_1 = \frac{1}{R}x_1x_2,\ u_2 = -\frac{1}{2R}(x_1^2 + \frac{C_{1122}}{C_{1111}}x_2^2),\ u_3 = 0, \tag{3.44}$$

which is equal to the solution of the bending problem in classical elasticity. Using the virtual work expression (1.2), we can find the bending moment per unit out-of-plane thickness acting on the beam as

$$\begin{aligned} M &= \int_{-H/2}^{H/2} s_{11}x_2\,\mathrm{d}x_2 - \int_{-H/2}^{H/2} m_{13}\,\mathrm{d}x_2 \\ &= \left(C_{1111} - \frac{C_{1122}^2}{C_{1111}}\right)\frac{H^3}{12R} + D_{1313}\frac{H}{R}. \end{aligned} \tag{3.45}$$

Multiplying the bending moment M with the radius of curvature R yields the bending stiffness B. By substituting the moduli for an isotropic material (Equations (3.19)) and using the definition of the characteristic length (Equation (3.26a)), the normalized bending stiffness B/B_{class} can be written as

$$\frac{B}{B_{\text{class}}} = 1 + 12(1-\nu)\left(\frac{l_c}{H}\right)^2, \tag{3.46}$$

with the classical bending stiffness B_{class} defined as

$$B_{\text{class}} = \frac{EH^3}{12(1-\nu^2)}. \tag{3.47}$$

The above results agree with the solutions given by Koiter [1964] and Gauthier and Jahsman [1975]. Similarly, by substituting the moduli for the transverse isotropic material (Equations (3.17)), we find

$$\frac{B}{B_{\text{class}}} = 1 + \frac{12}{1+\nu_p}\left(\frac{l_c}{H}\right)^2 , \tag{3.48}$$

with

$$B_{\text{class}} = \frac{E_{\text{p}} H^3}{12} . \tag{3.49}$$

Since we have $\nu_{\text{pt}} = 0$ for the transverse isotropic materials, there is no coupling with the out-of-plane dimension and the classical bending stiffness (Equation (3.49)) is lower than the classical bending stiffness for isotropic materials (Equation (3.47)).

Figure 3.10a shows the effect of the characteristic length l_{c} on the normalized bending stiffness for a transverse isotropic material with $\nu_{\text{p}} = 0.9$, which is a representative value for the cellular microstructures that we analyzed. We see that, as in the case of simple shear (see Fig. 3.1a), for $l_{\text{c}}/d \to 0$, the solution for the micropolar continuum theory reduces to the solution of the same problem in the classical continuum theory. There is a stiffening in the small H/d regime ($B/B_{\text{class}} > 1$), which becomes more pronounced with increasing l_{c}/d. Note that our results for the discrete models (see chapter 2), on the contrary, show weakening, i.e. a lower bending rigidity for small heights. For larger heights, the bending stiffness converges to its classical counterpart. Figure 3.10b shows the effect of the Poisson's ratio on the stiffening behaviour; the stiffening is larger for a lower Poisson's ratio.

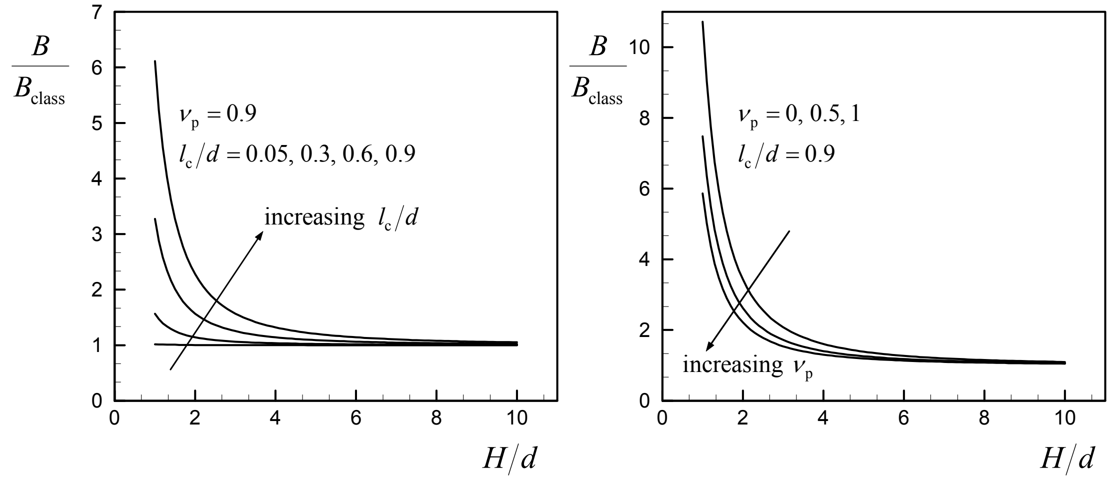

(a) (b)

Figure 3.10: (a) The effect of the characteristic length l_{c} on the normalized bending stiffness for a transverse isotropic material with $\nu_{\text{p}} = 0.9$. (b) The effect of the Poisson's ratio ν_{p} on the normalized bending stiffness for $l_{\text{c}}/d = 0.9$.

3.6 Summary and discussion

In this chapter, we have solved the simple shear and the pure bending problems analytically for the micropolar continuum theory. We investigated the effect of the two additional micropolar constants: the coupling factor m and the characteristic length l_c. By comparing the analytical and the discrete solutions for the simple shear problem in terms of the macroscopic shear stiffness, we found that it was possible to fit all discrete results only if the coupling factor m was taken to be very large ($m \to \infty$). In this limit, the micropolar theory reduces to the couple stress theory in which microrotations are no longer independent degrees of freedom but are constrained to be equal to the macroscopic rotations, $(u_{2,1}-u_{1,2})/2$. From the comparison it was found that l_c scales with the cell size d and depends on the cellular morphology, with l_c/d in the range 0.15 – 0.9.

We developed a strain mapping procedure to be able to obtain the strain fields based on the displacement data given by the discrete calculations. For the square and the Voronoi microstructures, we used this strain mapping procedure to compare the discrete microrotation and strain fields for the simple shear problem with their continuum counterparts given by the analytical couple stress solution. It was shown that the characteristic length l_c obtained by fitting the macroscopic shear stiffness resulted in an excellent agreement between the discrete and continuum microrotation and strain fields.

Hexagonal materials have six-fold symmetry in the x_1-x_2 plane, which makes them transversely (in-plane) isotropic both in classical and micropolar continuum theories (see also section 2.2.1). This means there is only one l_c value for the regular hexagonal structure, irrespective of its orientation. This is clearly in contradiction with Fig. 3.2b and c, yielding two different values for l_c for the default ($l_c = 0.15d$) and the rotated ($l_c = 0.28d$) orientation. However, the large scatter in the discrete results and the relatively low stiffening makes it hard to find a unique fit; i.e. taking $l_c = 0.28d$ would also make a reasonable fit for the default hexagons that falls well within the scatter band (see Figs. 2.11b and 3.2b). Random imperfections in the hexagonal structure not only reduce the scatter, it also decreases the difference between the two orientations (Figs. 2.11d and e and Figs. 3.2d and e). As a result, the fitting procedure is more accurate, leading to values of l_c that are close together. The results for the fully random structures are orientation-independent with a limited amount of scatter (Figs. 2.11f and 3.2f). By taking into account the isotropy of the structures, good fits are obtained for $l_c/d = 0.28$ for the regular hexagons, $l_c/d = 0.47$ for the perturbed hexagons and $l_c/d = 0.9$ for the Voronoi structures. These characteristic lengths also reflect the increasing stiffening with increasing randomness.

The current study enables a comparison with existing homogenization studies on regular lattices. For square structures, Banks and Sokolowski [1968] and Adachi *et al.* [1998] found $l_c/d=0.289$ for couple stress theory ($m \to \infty$). Warren and Byskov [1997] and Chen *et al.* [1998] found $m=1$, $l_c/d=0.289$ and $m=1$, $l_c/d=0.577$, respectively. For regular hexagonal structures, Warren and Byskov [2002], Pradel and Sab [1998] and Wang and Stronge [1999] found m=0.5 and $l_c/d=0.11$, while Chen et al. [1998] found m=0.5 and $l_c/d=0.22$. By comparing the continuum solutions based on these parameters with the discrete results and the best couple stress fits (Figs. 3.2a-c), it follows that the 'homogenization parameters' have a strong tendency to underestimate the discrete stiffening effect. It should be noted, however, that the scatter in the small *H/d* regime is too large to make any conclusive statements.

The system parameters that determine the overall elastic response to a shear deformation in couple stress theory are H, E_p, ν_p and D_{1313}. The overall stiffness S $(=F/(L\gamma))$ can be written in terms of the system parameters as

$$S\left(H, E_\mathrm{p}, \nu_\mathrm{p}, D_{1313}\right) = G\, g\left(\frac{H}{l_\mathrm{c}}\right), \tag{3.50}$$

with $2G=E_\mathrm{p}/(1+\nu_\mathrm{p})$, $2l_\mathrm{c}^2 = D_{1313}/G$, and the function g being dependent on H/l_c only. As discussed in section 2.3.1 a similar expression for the average discrete results was obtained in terms of the microstructural parameters:

$$S\left(t, d, H, E_\mathrm{s}\right) = G f\left(\frac{H}{d}\right), \tag{3.51}$$

with

$$G = cE_s\left(\frac{t}{d}\right)^3, \tag{3.52}$$

and c a dimensionless constant. By taking G to be the classical shear stiffness of the specific cellular microstructure under consideration in both Equation (3.50) and (3.51), the function g can be fitted to the discrete function f, which was found to yield $l_\mathrm{c}=\alpha d$, with α a dimensionless constant between 0.28 and 0.9, depending on cellular morphology. By using the definition of l_c, the new micropolar constant D_{1313} can be written in terms of the microstructural parameters as

$$D_{1313} = 2cE_s\left(\frac{t}{d}\right)^3\left(\alpha d\right)^2, \tag{3.53}$$

with α and c dimensionless constants specific for the cellular microstructure under consideration.

For pure bending the discrete results show softening while micropolar theory predicts stiffening for non-zero values of the characteristic length (independent from the value of the coupling factor m). Clearly, free edge effects leading to softening cannot be captured by the micropolar theory, giving the opposite effect instead.

4 Strain Divergence Theory

In this chapter, we propose a higher-grade continuum theory that treats the divergence of the strains as an independent deformation measure, in addition to the classical strains. We derive the equilibrium equations and the natural boundary conditions. We solve the simple shear and the pure bending problems, and compare the results with the discrete analyses of chapter 2.

4.1 Introduction

The discrete results obtained in Chapter 2 show that a stiffening mechanism is triggered when the cellular materials are subjected to an applied shear deformation. By analyzing the local deformation fields we learned that boundary layers form that are associated with gradients in micro-rotations and shear strains. Another deformation mode that is often associated with deformation gradients and size effects is bending. However, under pure bending the stiffening mechanism was found to be not active. Instead, free-edge effects resulted in overall weakening, which was also observed under uniaxial loading, i.e. in the absence of gradients. Aim of this chapter is to find a generalized continuum theory that is able to pick up the stiffening mechanism under shear, but leaves it inactive under bending.

The stiffening mechanism in the micropolar theory is associated with the gradients in microrotation. These are triggered under shear and when fully coupled to the macroscopic rotations, are able to accurately describe the global (stiffening) and local (boundary layer) response of the discrete microstructures analyzed. However, the same rotation gradients are active under bending as well, erroneously leading to stiffening. Here, we focus on the gradients of strain instead. The particular strain gradient measure should preferably coincide with the shear strain gradient in shear and should be absent in bending. For this, we propose to use the divergence of strain as an additional deformation measure in the theory.

In section 4.2 we derive the equilibrium equations and the natural boundary conditions of the strain divergence theory. In section 4.3, we develop a finite element implementation of the theory. Section 4.4 shows the analytical solution for the simple shear problem and the comparison of the analytical and the discrete results in terms of the macroscopic shear stiffness. In section 4.5, we solve the pure bending problem analytically for the strain divergence theory and finally, in section 4.6, we summarize and discuss the results.

4.2 Strain divergence theory

The deformation measures in strain divergence theory are the conventional strain ε_{ij} and the divergence of strain η_i, defined as

$$\varepsilon_{ij} = \frac{1}{2}(u_{j,i} + u_{i,j}) \quad \text{and} \quad \eta_i = \varepsilon_{ij,j} = \frac{1}{2}(u_{j,ij} + u_{i,jj}). \tag{4.1}$$

For a linear elastic, anisotropic material, the strain energy density function can be written as

$$w(\varepsilon_{ij},\eta_i)=\frac{1}{2}C_{ijkl}\varepsilon_{ij}\varepsilon_{kl}+B_{ijk}\varepsilon_{ij}\eta_k+D_{ij}\eta_i\eta_j, \tag{4.2}$$

where the linear terms in ε_{ij} and η_i are omitted to have zero stress in the undeformed state. Note that in the third term of Equation (4.2), the components of the vector η_k change sign under an inversion of the coordinate system, whereas the components of the tensor ε_{ij} do not. To have an objective strain energy density, B_{ijk} must be a pseudo-tensor (i.e. a tensor whose components change sign under an inversion of the coordinate system). For a material with *central symmetry*, however, the elastic constants must be independent with respect to an inversion of the coordinate system, and this requires the tensor B_{ijk} to vanish (see also section 1.3.1).

The constants D_{ij} are new higher-order constants associated with the divergence of strain η_i, and they have unit of force. The Cauchy stress tensor σ_{ij} and the higher-order stress vector τ_i are work conjugates to the strain tensor ε_{ij} and to the strain divergence vector η_i, and are given as

$$\sigma_{ij}=\frac{\partial w}{\partial\varepsilon_{ij}}=C_{ijkl}\varepsilon_{kl}\quad\text{and}\quad\tau_i=\frac{\partial w}{\partial\eta_i}=2D_{ij}\eta_j, \tag{4.3}$$

respectively. For an isotropic material, $D_{ij}=a\delta_{ij}$, with "*a*" being a positive constant. The variation of the total strain energy in a volume V can be written as

$$\delta\int_V w\,\mathrm{d}V=\underbrace{\int_V\sigma_{ij}\delta\varepsilon_{ij}\,\mathrm{d}V}_{I_1}+\underbrace{\int_V\tau_i\delta\eta_i\,\mathrm{d}V}_{I_2}. \tag{4.4}$$

I_1 and I_2 are the parts of the total strain energy density associated with the conventional and higher order terms, respectively. Applying Gauss's divergence theorem, I_1 yields

$$I_1=\int_S n_i\sigma_{ij}\delta u_j\,\mathrm{d}S-\int_V\sigma_{ij,i}\delta u_j\,\mathrm{d}V, \tag{4.5}$$

where n_i is the outward unit vector normal to the boundary surface S of the volume V. I_2 can be written as

$$I_2 = \frac{1}{2}\left(\underbrace{\int_V \tau_i \delta u_{j,ij} \, \mathrm{d}V}_{P_1} + \underbrace{\int_V \tau_i \delta u_{i,jj} \, \mathrm{d}V}_{P_2} \right). \tag{4.6}$$

Applying Gauss's divergence theorem to P_1 gives

$$P_1 = \underbrace{\int_S n_j \tau_i \delta u_{j,i} \, \mathrm{d}S}_{K_1} - \underbrace{\int_V \tau_{i,j} \delta u_{j,i} \, \mathrm{d}V}_{K_2}. \tag{4.7}$$

Note that if δu_j is already specified on the surface S, the surface part of $\delta u_{j,i}$ cannot be prescribed independently. Therefore, to be able to correctly determine the independent boundary conditions, we decompose the gradient operator into its surface and normal components (see e.g. Mindlin [1964]),

$$\partial_i = D_i + n_i D, \tag{4.8}$$

where the surface gradient operator D_i and the normal gradient operator D are defined as

$$D_i = (\delta_{ij} - n_i n_j)\partial_j \quad \text{and} \quad D = n_k \partial_k, \tag{4.9}$$

respectively. Now we can write K_1 in terms of the components of the gradient vector,

$$K_1 = \int_S [D_i(n_j \tau_i \delta u_j) - D_i(n_j \tau_i)\delta u_j + n_i n_j \tau_i \delta D u_j] \, \mathrm{d}S. \tag{4.10}$$

To further reduce the first term of K_1 we make use of Stokes' surface divergence theorem. This theorem states that the integral of the surface gradient of a continuously differentiable vector function v on a surface S having and edge C, can be written as

$$\int_S D_i v_i \, d\mathrm{S} = \int_S (D_i n_i) n_j v_j \, \mathrm{d}S + \oint_C z_i v_i \, \mathrm{d}s. \tag{4.11}$$

In (4.11), $z_i = \in_{ijk} q_j n_k$ where $\in_{ijk}$ is the Levi-Civita permutation tensor, q_j is the unit tangent vector along the edge C, n_k is the unit normal to the surface S and s is the arc length along C in the direction of q_j. The positive sign of q_j is such that "a man walking along the edge C in the positive q_j direction will find the interior of S to the left, provided his head is in the positive n_k direction" (Malvern [1969]). For the situation that the volume V has a surface S that consists of m smooth surface segments S_m, with each surface segment having an edge C_m, it follows that

$$\int_S D_i v_i \, \mathrm{d}S = \int_S (D_i n_i) n_j v_j \, \mathrm{d}S + \sum_m \oint_{C_m} z_i v_i \, \mathrm{d}s. \tag{4.12}$$

Figure 4.1, for instance, shows a volume V with a surface S consisting of 32 surface segments S_m (20 hexagons and 12 pentagons). The last term of Equation (4.12) is the sum of all integrals over the closed contours C_m. This means that each edge segment C (see Fig. 4.1) has contributions from two contour integrals (over the edges C_1 and C_2 in Fig. 4.1) associated with the two adjacent surface segments S_1 and S_2:

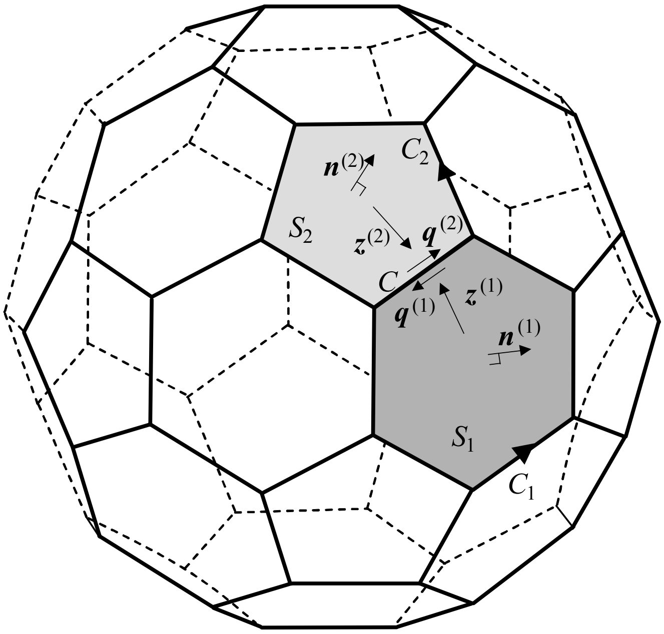

Figure 4.1: Illustration for the positive directions $q^{(1)}$ and $q^{(2)}$ along an edge C with respect to the surfaces S_1 and S_2 to which it is connected.

$$\int_C z_i v_i ds = \int_{C_1} z_i^{(1)} v_i \mathrm{d}s^{(1)} + \int_{C_2} z_i^{(2)} v_i \mathrm{d}s^{(2)}. \tag{4.13}$$

By substituting $z_i^{(d)} = \in_{ijk} q_j^{(d)} n_k^{(d)}$, $(d = 1, 2)$ and accounting for the fact that the tangents q_j have opposite directions, $q_j^{(2)} \mathrm{d}s^{(2)} = -q_j^{(1)} \mathrm{d}s^{(1)}$, the contribution of an edge C to the last term of Equation (4.12) can be written as

$$\int_C \in_{ijk} q_j^{(1)} (n_k^{(1)} - n_k^{(2)}) v_i \, \mathrm{d}s^{(1)} = \int_C \Delta b_i^{(1)} v_i \mathrm{d}s^{(1)}, \tag{4.14}$$

with $\Delta b_i^{(1)} = \in_{ijk} q_j^{(1)}(n_k^{(1)} - n_k^{(2)})$. The edge contribution is associated with the jump $\Delta b_i^{(1)}$ that vanishes when there are no sharp edges ($n_k^{(1)} = n_k^{(2)}$). If written in terms of jumps as in Equation (4.14), the contour integrals in Equation (4.12) reduce to line integrals and the summation extends over all line segments (such as C in Fig. 4.1). Here, we will not do so, but continue with the expression in Equation (4.12). Applying Stokes' surface divergence theorem (Equation (4.12)) to the first term of K_1 in Equation (4.10) yields

$$\begin{aligned} K_1 = {} & \int_S [(D_p n_p) n_i n_j \tau_i - D_i(n_j \tau_i)]\delta u_j \ \mathrm{d}S \\ & + \int_S (n_i n_j \tau_i)\delta D u_j \ \mathrm{d}S + \sum_m \oint_{C_m} z_i n_j \tau_i \delta u_j \mathrm{d}s. \end{aligned} \tag{4.15}$$

By applying Gauss's divergence theorem to K_2 in Equation (4.7), we find

$$K_2 = \int_S n_i \tau_{i,j} \delta u_j \ \mathrm{d}S - \int_V \tau_{i,ji} \delta u_j \ \mathrm{d}V. \tag{4.16}$$

Following the same procedure for P_2 in Equation (4.6), we can write the variation in the total strain energy density as

$$\begin{aligned} \delta \int_V w \ \mathrm{d}V = {} & -\int_V [\sigma_{ij,i} - \frac{1}{2}(\tau_{i,ji} + \tau_{j,ii})]\delta u_j \ \mathrm{d}V + \\ & \int_S [n_i \{\sigma_{ij} + \frac{1}{2} \left\langle (D_p n_p)(n_j \tau_i + n_i \tau_j) - (\tau_{i,j} + \tau_{j,i}) \right\rangle \} \\ & - \frac{1}{2} D_i (n_j \tau_i + n_i \tau_j)]\delta u_j \ \mathrm{d}S + \\ & \frac{1}{2} \int_S [n_i (n_j \tau_i + n_i \tau_j)]\delta D u_j \ \mathrm{d}S + \\ & \frac{1}{2} \sum_m \oint_{C_m} z_i (n_j \tau_i + n_i \tau_j)\delta u_j \ \mathrm{d}s. \end{aligned} \tag{4.17}$$

The external work done on the body is

$$W^{ex} = \int_V f_j \delta u_j \ \mathrm{d}V + \int_S (t_j \delta u_j + r_j \delta D u_j) \ \mathrm{d}S + \sum_m \oint_{C_m} s_j \delta u_j \ \mathrm{d}s, \tag{4.18}$$

where f_j is the body force per unit volume, t_j is the surface traction, r_j is the higher-order surface traction and s_j is the line force acting over any sharp edge C_m. By equating the external work done on the body to the internal energy stored, we obtain the equilibrium equations

$$\sigma_{ij,i} - \frac{1}{2}(\tau_{i,ji} + \tau_{j,ii}) + f_j = 0, \tag{4.19}$$

in the volume V, and the boundary conditions on the surface S and along the sharp edges C_m, respectively,

$$\begin{gathered} n_i\{\sigma_{ij} + \frac{1}{2}\left\langle (D_p n_p)(n_j\tau_i + n_i\tau_j) - (\tau_{i,j} + \tau_{j,i})\right\rangle\} - \frac{1}{2}D_i(n_j\tau_i + n_i\tau_j) = t_j^{*} \\ \text{or} \quad u_j = u_j^{*}, \\ \frac{1}{2}n_i(n_j\tau_i + n_i\tau_j) = r_j^{*} \quad \text{or} \quad Du_j = Du_j^{*}, \end{gathered} \tag{4.20}$$

and

$$\frac{1}{2}z_i(n_j\tau_i + n_i\tau_j) = s_j^{*} \quad \text{or} \quad u_j = u_j^{*}, \tag{4.21}$$

where the superscript * indicates a prescribed quantity on the surface, or along an edge. Note that the strain divergence theory is a special case of Toupin-Mindlin's strain gradient elasticity: If the four higher-order constants (a_1, a_2, a_4, a_5) in Equation (1.14) vanish, the strain gradient theory reduces to the strain divergence theory, with $a_3 = a$.

4.3 Finite element implementation

To analytically solve the partial differential equations of the strain divergence theory for engineering problems with complex geometries and/or complex loading conditions is a tedious job and even impossible in some cases. Therefore, we will develop a finite element implementation of the strain divergence theory in this section. The strain divergence involves second order gradients of the displacements, which requires C^1-continuous interpolation functions (i.e., both the function and its derivative are continuous at the interface between elements) for the usual displacement-based finite elements. However, there exist no robust C^1-continuous finite elements in the literature for higher order continuum theories (Shu *et al.* [1999], Engel *et al.* [2002]). Hence, we will re-write the virtual work principle in such a form that it is sufficient to use C^0-continuous shape functions. For this purpose, we introduce extra nodal degrees of freedom through a second order tensor ϕ_{ij}, and a related deformation vector $\hat{\eta}_i = (\phi_{ij} + \phi_{ji})_{,j}/2$. If we strictly enforce the constraint

$$\phi_{ij} = u_{i,j} \tag{4.22}$$

everywhere, then $\hat{\eta}_i$ becomes exactly equal to η_i. In that sense, ϕ_{ij} and $\hat{\eta}_i$ can be referred to as the 'relaxed' displacement gradient and strain divergence, respectively. To enforce this constraint we will use a penalty method. We define an error e_{ij} as

$$e_{ij} = u_{i,j} - \phi_{ij}, \tag{4.23}$$

and a work conjugate penalty measure ρ_{ij} as

$$\rho_{ij} = ke_{ij}, \tag{4.24}$$

where k is the penalty factor. Now, the kinematic constraint (4.22) may be enforced in the volume in an average sense through

$$\int\limits_V \rho_{ij} \delta e_{ij} \, \mathrm{d}V = 0 \quad \text{(no summation on } i \text{ and } j\text{)}, \tag{4.25}$$

which also ensures that the error e_{ij} will be small at the surface. Finally, assuming a smooth surface (so that the line integral at the right hand side of Equation (4.18) vanishes), the virtual work principal may be written, in the absence of body forces, as

$$\int\limits_V (\sigma_{ij} \delta \varepsilon_{ij} + \tau_i \delta \hat{\eta}_i + \rho_{ij} \delta e_{ij}) \, \mathrm{d}V = \int\limits_S (t_j \delta u_j + R_{ij} \delta \phi_{ij}) \, \mathrm{d}S, \tag{4.26}$$

where $R_{ij} = n_i r_j$. For plane strain loading conditions, the principle of virtual work can be written in vector form as

$$\int\limits_V \delta \boldsymbol{\chi}^{\mathrm{T}} \boldsymbol{\kappa} \, \mathrm{d}V = \int\limits_S \delta \boldsymbol{q}^{\mathrm{T}} \boldsymbol{f} \, \mathrm{d}S, \tag{4.27}$$

where

$$\begin{aligned}
\boldsymbol{\kappa} &= \{\sigma_{11}, \sigma_{22}, \sigma_{12}, \tau_1, \tau_2, \rho_{11}, \rho_{22}, \rho_{12}, \rho_{21}\}^{\mathrm{T}}, \\
\boldsymbol{\chi} &= \{\varepsilon_{11}, \varepsilon_{22}, 2\varepsilon_{12}, \hat{\eta}_1, \hat{\eta}_2, e_{11}, e_{22}, e_{12}, e_{21}\}^{\mathrm{T}}, \\
\boldsymbol{f} &= \{t_1, t_2, R_{11}, R_{22}, R_{12}, R_{21}\}^{\mathrm{T}}, \\
\boldsymbol{q} &= \{u_1, u_2, \phi_{11}, \phi_{22}, \phi_{12}, \phi_{21}\}^{\mathrm{T}}.
\end{aligned} \tag{4.28}$$

$\boldsymbol{\kappa}$, $\boldsymbol{\chi}$, $\boldsymbol{f}$ and $\boldsymbol{q}$ are the generalized stress, generalized strain, generalized traction and nodal degrees of freedom vectors, respectively. The superscript $^{\mathrm{T}}$ indicates the transpose of a matrix or vector. To be able to obtain a unique solution, one has to prescribe four independent boundary conditions on a smooth surface, see Equations (4.17). If the tractions t_j^* and higher order tractions r_j^* on the surface are known, the boundary conditions to be specified for the finite element method are

$$t_j = t_j^* \quad \text{and} \quad R_{ij} = n_i r_j^*. \tag{4.29}$$

Note that for the remainder of this chapter, subscript indices take the values 1 and 2 only. In case of pure displacement loading (u_j^* and Du_j^* are prescribed), we have

$$u_j = u_j^* \quad \text{and} \quad \phi_{ij} = n_j Du_i^* + D_j u_i^*. \tag{4.30}$$

Equation (4.30b) consists of four boundary conditions, of which only two are independently related to Du_j^*. The additional two enforce that the relaxed displacement gradients tangent to the surface are equal to the surface gradients of u_j^*. To make this explicit, we can write

$$\phi_{ij} = (\phi_{ik} n_k) n_j + (\phi_{ik} m_k) m_j, \tag{4.31}$$

where m_i is a unit vector tangent to the surface. Equation (4.30b) is then identical to

$$\phi_{ik} n_k = Du_i^* \text{ and } \phi_{ik} m_k = m_k u_{i,k}^*, \tag{4.32}$$

clearly showing that the first two equations of (4.32) are used to describe the boundary conditions and the second two to complete the constraint $e_{ij} = 0$ at the surface.

Figure 4.2a and b show two triangular elements that we developed for the strain gradient elasticity, to which we refer as the linear and the quadratic element, respectively. The linear element has in total 18 degrees of freedom, six at each node, namely u_1, u_2, ϕ_{11}, ϕ_{22}, ϕ_{12}, ϕ_{21}. The displacements u_i and the relaxed displacement gradients ϕ_{ij} are both interpolated using standard linear shape functions. The generalized strain vector $\boldsymbol{\chi}$ is related to the nodal values of displacements u_i and the relaxed displacement gradients ϕ_{ij} via

$$\boldsymbol{\chi} = \boldsymbol{L}\boldsymbol{N}\boldsymbol{q}^e. \tag{4.33}$$

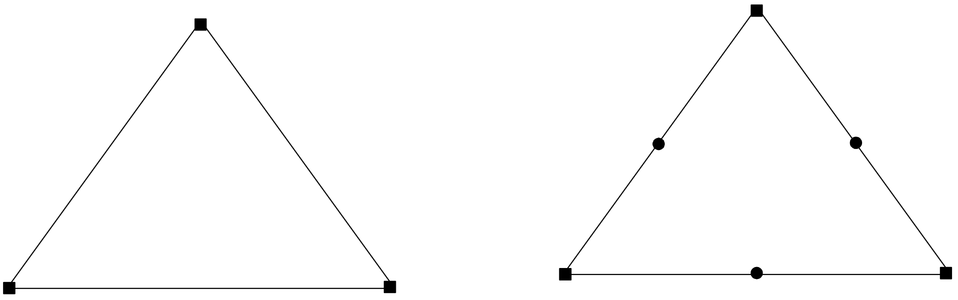

DOF at ■: $u_1, u_2, \phi_{11}, \phi_{22}, \phi_{12}, \phi_{21}$
DOF at ●: u_1, u_2

Figure 4.2: Sketch of (a) a linear element and (b) a quadratic element.

where L is the differential operator matrix, N is the shape function matrix and $\boldsymbol{q}^e$ is the vector for the 18 nodal degrees of freedom for an element. L is given as

$$L = \begin{bmatrix} \partial/\partial x_1 & 0 & \partial/\partial x_2 & 0 & 0 & \partial/\partial x_1 & 0 & \partial/\partial x_2 & 0 \\ 0 & \partial/\partial x_2 & \partial/\partial x_1 & 0 & 0 & 0 & \partial/\partial x_2 & 0 & \partial/\partial x_1 \\ 0 & 0 & 0 & \partial/\partial x_1 & 0 & -1 & 0 & 0 & 0 \\ 0 & 0 & 0 & 0 & \partial/\partial x_2 & 0 & -1 & 0 & 0 \\ 0 & 0 & 0 & \partial/2\partial x_2 & \partial/2\partial x_1 & 0 & 0 & -1 & 0 \\ 0 & 0 & 0 & \partial/2\partial x_2 & \partial/2\partial x_1 & 0 & 0 & 0 & -1 \end{bmatrix}^T, \tag{4.34}$$

The generalized stress vector $\boldsymbol{\kappa}$ is related to the generalized strains $\boldsymbol{\chi}$ through

$$\boldsymbol{\kappa} = (D_1 + kD_2)\boldsymbol{\chi}, \tag{4.35}$$

where

$$D_1 = \begin{bmatrix} C_{1111} & C_{1122} & & & & & & & \\ C_{1122} & C_{1111} & & & & & & & \\ & & \frac{A^{(1)}_{1212}}{2} & & & & 0 & & \\ & & & 2a & & & & & \\ & & & & 2a & & & & \\ & & & & & 0 & & & \\ & & 0 & & & & 0 & & \\ & & & & & & & 0 & \\ & & & & & & & & 0 \end{bmatrix}, D_2 = \begin{bmatrix} 0 & & & & & & & & \\ & 0 & & & & & & & \\ & & 0 & & & 0 & & & \\ & & & 0 & & & & & \\ & & & & 0 & & & & \\ & & & & & 1 & & & \\ & & 0 & & & & 1 & & \\ & & & & & & & 1 & \\ & & & & & & & & 1 \end{bmatrix}. \tag{4.36}$$

D_1 relates the stress σ_{ij} and the higher order stresses τ_i to the strains ε_{ij} and the strain divergence $\hat{\eta}_i$, and D_2 relates the error e_{ij} to the penalty measure ρ_{ij}. Note that the classical coefficients can be obtained for several cellular microstructures from chapter 3. By substituting Equations (4.33) and (4.35) in the principle of virtual work for one element, Equation (4.27), it follows that

$$\delta \boldsymbol{q}^{e\mathrm{T}} \int_V (B^{\mathrm{T}} D_1 B + kB^{\mathrm{T}} D_2 B)\, \mathrm{d}V \boldsymbol{q}^e = \delta \boldsymbol{q}^{e\mathrm{T}} \int_S N^{\mathrm{T}} \boldsymbol{f}\, \mathrm{d}S, \tag{4.37}$$

where $B = LN$. The discretised equilibrium equations read

$$(K_1{}^e + kK_2{}^e) q^e = K^e q^e = f^e, \tag{4.38}$$

with

$$K_1{}^e = \int_V B^T D_1 B\, \mathrm{d}V \quad \text{and} \quad K_2{}^e = \int_V B^T D_2 B\, \mathrm{d}V. \tag{4.39}$$

$K_1{}^e$ and $K_2{}^e$ form together the stiffness matrix K^e for an element, and they introduce five and four independent relations at each Gauss integration point, respectively.

The linear element (Fig. 4.2a) uses linear shape functions; therefore a patch test for this element must satisfy

$$\begin{aligned} u_i &= A_i + B_i x_1 + C_i x_2, \\ \phi_{ij} &= u_{i,j}, \end{aligned} \tag{4.40}$$

for all possible patches and boundary conditions. In other words, if the values corresponding to the fields given in (4.40) are prescribed at the boundary nodes, the finite element calculations should give the exact values of the displacements u_i and the relaxed displacement gradients ϕ_{ij} for the internal nodes (consistency requirement). We used several different patches containing at least one internal node from which it was concluded that the consistency requirement is satisfied. In addition, to ensure stability, the stiffness matrix for a patch should be non-singular provided that the rigid body modes are eliminated (for a detailed discussion of the patch test, see e.g. Zienkiewicz and Taylor [2000]). If we use a single Gauss integration point for both $K_1{}^e$ and $K_2{}^e$, the total number of independent equations is nine, whereas a single element has thirteen degrees of freedom after subtracting the minimum number of degrees of freedom required to eliminate the rigid body motion. As a result, it fails the stability test. The singularity of the total stiffness matrix disappears for patches with large number of elements. It should be noted that for large patches the element is susceptible for locking for large values of k, since the stiffness matrix $K_2{}^e$ is non-singular (see e.g. Zienkiewicz and Taylor [2000]).

The quadratic triangular element (see Fig. 4.2b) has six nodes. It has 24 degrees of freedom in total: Each corner node contains all six degrees of freedom (u_1, u_2, ϕ_{11}, ϕ_{22}, ϕ_{12}, ϕ_{21}) and each mid-side node contains only two displacement degrees of freedom (u_1, u_2). Displacements u_i are interpolated using quadratic shape functions and the relaxed displacement gradients ϕ_{ij} are interpolated using standard linear shape functions. For that reason, next to the patch test performed in the case of linear element, we also performed a quadratic patch test, where

$$\begin{aligned} u_i &= A_i + B_i x_1 + C_i x_2 + D_i x_1 x_2 + E_i x_1{}^2 + F_i x_2{}^2, \\ \phi_{ij} &= u_{i,j}. \end{aligned} \tag{4.41}$$

$K_1{}^e$ and $K_2{}^e$ are integrated by three- and one-point Gaussian quadrature, respectively. For several assemblies tested, as well as a single element, the quadratic triangular element satisfies both the consistency and stability requirements of the patch test. In addition, $K_2{}^e$ is singular, so that locking will not occur when k becomes large.

In the next section, we will show the convergence for the linear and quadratic elements by comparing the finite element calculations with the analytical solution for the simple shear problem.

4.4 Analytical solution of the simple shear problem

Figure 4.3 shows the boundary conditions of the simple shear problem for the strain divergence theory in plane strain. In addition to the displacement boundary conditions corresponding to the classical problem, we specify the higher-order boundary conditions ($Du_1 = Du_2 = 0$, at $x_2 = 0, H$). The first higher-order boundary condition,

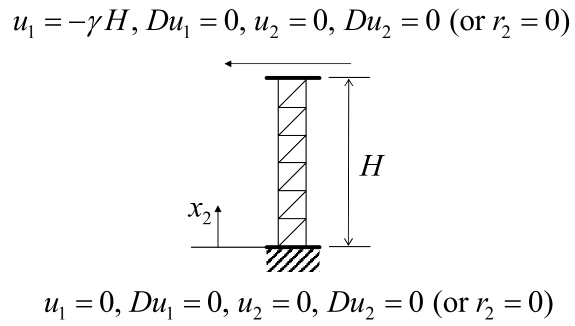

Figure 4.3: Illustration of a finite element mesh and boundary conditions for the simple shear problem using strain divergence elasticity.

$Du_1 = u_{1,2} = 0$, represents the perfect bonding between the face sheets and the core material, which was embodied into the discrete calculations by fixing the rotational degrees of freedom of the beam elements at the nodes where they connect to the face sheets (see Fig. 2.9). The second boundary condition, $Du_2 = u_{2,2} = 0$, however, is physically less clear. One could equally well prescribe the work-conjugate higher-order surface traction, $r_2 = 0$. In the following we will explore both possibilities.

The sample is taken to be infinitely long in the x_1 direction, and therefore, all field variables are independent of x_1. The kinematic variables are

$$\begin{gathered}\varepsilon_{11} = 0, \quad \varepsilon_{22} = u_{2,2}, \quad \varepsilon_{12} = \frac{1}{2} u_{1,2}, \\ \eta_1 = \varepsilon_{12,2} = \frac{1}{2} u_{1,22}, \quad \eta_2 = \varepsilon_{22,2} = u_{2,22}.\end{gathered} \tag{4.42}$$

In the absence of body forces, the equilibrium equations (4.19) reduce to

$$\sigma_{12,2} - \frac{1}{2} \tau_{1,22} = 0, \tag{4.43}$$

and

$$\sigma_{22,2} - \tau_{2,22} = 0. \tag{4.44}$$

Inserting the kinematics into the equilibrium equations via the constitutive equations (Equations (4.35) with $k = 0$) gives

$$l_{\mathrm{c}}^2 u_{1,2222} - u_{1,22} = 0, \tag{4.45}$$

and

$$2 l_{\mathrm{c}}^2 u_{2,2222} - \frac{C_{1111}}{A_{1212}^{(1)}} u_{2,22} = 0, \tag{4.46}$$

where l_c is the characteristic length defined as

$$l_{\mathrm{c}}^2 = \frac{a}{A_{1212}^{(1)}}. \tag{4.47}$$

The solutions of these differential equations read

$$u_1 = C_1 + C_2 x_2 + C_3 e^{K_1 x_2} + C_4 e^{-K_1 x_2}, \tag{4.48}$$

and

$$u_2 = D_1 + D_2 x_2 + D_3 e^{K_2 x_2} + D_4 e^{-K_2 x_2}, \tag{4.49}$$

with $K_1 = 1/l_c$ and $K_2 = (C_{1111} / 2A^{(1)}_{1212})^{\frac{1}{2}} / l_c$. Incorporating the boundary conditions for u_1 yields

$$\begin{aligned}
C_1 &= \frac{\gamma H(e^{K_1 H} + e^{-K_1 H} - 2)}{4 - (2 - K_1 H)e^{K_1 H} - (2 + K_1 H)e^{-K_1 H}}, \\
C_2 &= \frac{\gamma HK(e^{-K_1 H} - e^{K_1 H})}{4 - (2 - K_1 H)e^{K_1 H} - (2 + K_1 H)e^{-K_1 H}}, \\
C_3 &= \frac{\gamma H(1 - e^{-K_1 H})}{4 - (2 - K_1 H)e^{K_1 H} - (2 + K_1 H)e^{-K_1 H}}, \\
C_4 &= \frac{\gamma H(1 - e^{K_1 H})}{4 - (2 - K_1 H)e^{K_1 H} - (2 + K_1 H)e^{-K_1 H}}.
\end{aligned} \tag{4.50}$$

For u_2, both choices of the higher order boundary conditions, $u_{2,2} = 0$ or $r_2 = 0$ at $x_2 = 0$ and H, give the same result:

$$D_1 = D_2 = D_3 = D_4 = 0 \Rightarrow u_2 = 0. \tag{4.51}$$

The non-vanishing tractions at the top surface of the sample are

$$t_1 = \frac{A^{(1)}_{1212}}{2} u_{1,2} - \frac{1}{2} a u_{1,222} \quad \text{and} \quad r_1 = \frac{1}{2} a u_{1,22}. \tag{4.52}$$

Since the work-conjugate to r_1, Du_1, is zero on the surface, the external work per unit out-of-plane thickness is done solely by t_1 and reduces to

$$W^{ex} = \int_S t_1 u_1 \, \mathrm{d}S = \gamma HGL l_c{}^2 u_{1,222}, \tag{4.53}$$

where L is the width of the sample and $A^{(1)}_{1212} = 2G$ has been substituted. Note that from Equations (4.48) and (4.50) it follows that in the limit that l_c goes to zero, W^{ex} converges to $HGL\gamma^2$, the solution for the classical problem.

By comparing the governing equations and boundary conditions of the shear problem for strain divergence theory (see above) and couple stress theory (see Equations (3.38) and (3.39)), it follows that the displacement fields and overall response are identical, provided that

$$l_{\mathrm{c}}^{\text{Strain Divergence}} = \frac{l_{\mathrm{c}}^{\text{Couple Stress}}}{\sqrt{2}}. \qquad (4.54)$$

In chapter 3, we have shown that the couple stress theory is able to successfully predict the local and global response for the analyzed discrete structures under simple shear, yielding specific values for the characteristic couple stress length. Therefore, the characteristic strain divergence length can be directly obtained from Equation (4.54).

In Figures 4.4a and b, we show the convergence for the linear and the quadratic finite elements implemented in the previous section, respectively. We compare the normalized shear strain $\varepsilon_{12}/\varepsilon_{12}'$ ($\varepsilon_{12}' = -\gamma/2$) through the thickness of a sample with $H/d = 10$ and $l_c/d = 0.64$, for the analytical and finite element solutions (d is the cell size). The finite element mesh is shown in Fig. 4.3. The vertical displacements along the sides of the column are constrained to be zero. The penalty factor k in Equation (4.35) needed to constrain the relaxed displacement gradients ϕ_{ij} to be equal to $u_{i,j}$ was found be at least $50A_{1212}^{(1)}$. To trace the convergence, we gradually increase the number of elements in the x_2 direction (NE). Both linear and quadratic elements give a converged solution with increasing NE, with the convergence rate being much larger for the quadratic element.

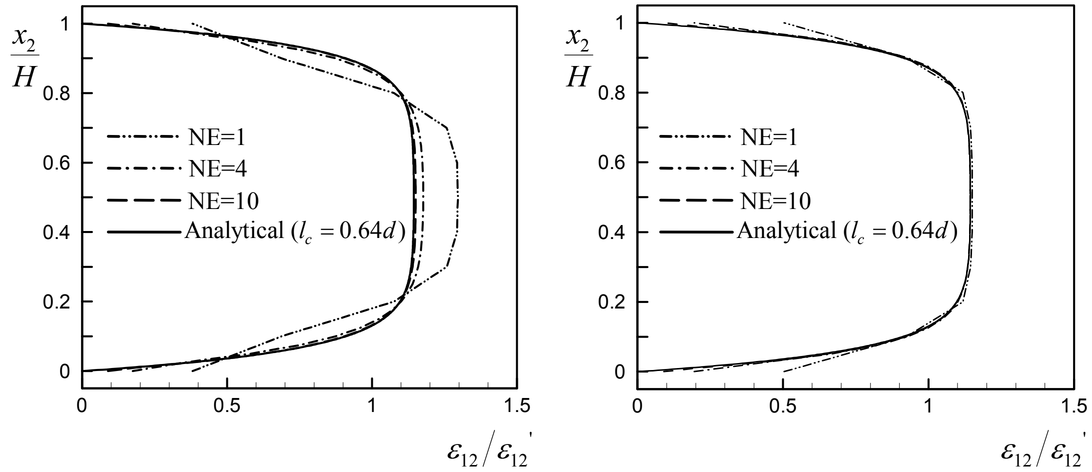

(a) (b)

Figure 4.4: Convergence study for (a) the linear and (b) the quadratic elements. The normalized shear strain $\varepsilon_{12}/\varepsilon_{12}'$ ($\varepsilon_{12}' = -\gamma/2$) through the thickness of a sample with $H/d = 10$ and $l_c/d = 0.64$ is plotted for an increasing number of elements in the x_2 direction (NE).

4.5 Analytical solution of the pure bending problem

In this section, we will solve the pure bending problem for the strain divergence theory[1]. The midplane of the plate is set as the x_1-x_3 plane, the x_3 direction coinciding with the out-of-plane direction (see Fig. 3.9). The pure bending assumption states that "transverse plane sections (that are parallel to the x_2-x_3 plane, in our case) remain plane and normal to the longitudinal fibres". A direct consequence of this is that the shear strains ε_{12} are zero throughout the beam. The most general displacement field that satisfies this can be written as

$$u_1 = \frac{1}{R} x_1 x_2, \; u_2 = -\frac{1}{2R} x_1^2 + f(x_2) + P, \; u_3 = 0, \tag{4.55}$$

where f is a function of x_2 alone and P is an integration constant. The corresponding non-vanishing in-plane strains and strain divergence are

$$\varepsilon_{11} = \frac{1}{R} x_2, \; \varepsilon_{22} = f_{,2}, \; \text{ and } \; \eta_2 = f_{,22}. \tag{4.56}$$

By inserting (4.56) into the constitutive equations (Equations (4.35) with $k = 0$), the non-vanishing in-plane stresses and higher-order stress are found as

$$\begin{aligned} \sigma_{11} &= C_{1111} \frac{x_2}{R} + C_{1122} f_{,2}, \\ \sigma_{22} &= C_{1111} f_{,2} + C_{1122} \frac{x_2}{R}, \\ \tau_2 &= 2a f_{,22}. \end{aligned} \tag{4.57}$$

The only non-trivial in-plane equilibrium equation is

$$\sigma_{22,2} - \tau_{2,22} = 0, \tag{4.58}$$

which combines with Equation (4.57) to yield the governing differential equation

$$2a f_{,2222} - C_{1111} f_{,22} - C_{1122} \frac{1}{R} = 0. \tag{4.59}$$

---

[1] See the Appendix for a summary of the bending solution for the strain gradient theory.

The solution of (4.59) reads

$$f=\frac{2a}{C_{1111}}\left(q_1e^{\sqrt{\frac{C_{1111}}{2a}}x_2}+q_2e^{-\sqrt{\frac{C_{1111}}{2a}}x_2}\right)-\frac{1}{2R}\frac{C_{1122}}{C_{1111}}x_2{}^2+q_3x_2+q_4. \tag{4.60}$$

If we merge the two constants q_4 in Equation (4.60) and P in Equation (4.55) into a single constant B, we have four unknowns (q_1, q_2, q_3, B) to be determined from the boundary conditions. The tractions at the top and the bottom surfaces are zero, yielding the (non-trivial) boundary conditions

$$\begin{aligned}&t_2=\pm(\sigma_{22}-\tau_{2,2})=0 \quad \text{at} \quad x_2=\pm H/2\,,\\&r_2=\tau_2=0 \quad \text{at} \quad x_2=\pm H/2\,.\end{aligned} \tag{4.61}$$

The first two equations ($t_2=0$ at ± $H/2$) are not linearly independent, which leaves only 3 independent equations. The fourth equation comes from specifying the displacement u_2 to be zero at $x_1=x_2=0$. Solving the four equations for the four unknowns yields

$$q_1=q_2=-\frac{BC_{1111}}{4a}=\frac{C_{1122}e^{\sqrt{\frac{C_{1111}}{8a}}H}}{C_{1111}R\left(e^{\sqrt{\frac{C_{1111}}{2a}}H}+1\right)},\quad q_3=0. \tag{4.62}$$

Now that we know the displacement fields, we can calculate the macroscopic bending moment by using the external work expression (4.18). The line force s_i acting at the sharp out-of-plane edges of a cross-section perpendicular to the length of the beam follows from Equation (4.21) to be (s_1, s_2, s_3) = ($\tau_2/2$, $\tau_1/2$, 0) at $x_2=H/2$ and (s_1, s_2, s_3) = (-$\tau_2/2$, -$\tau_1/2$, 0) at $x_2=-H/2$. The component of the edge force that does work is s_1, but since $\tau_2=0$ is prescribed at the top and bottom surfaces, this contribution vanishes. As a result, the bending moment per unit out-of-plane thickness can be written as

$$M=\int_{-H/2}^{H/2}x_2\sigma_{11}\,\mathrm{d}x_2-\frac{1}{2}\int_{-H/2}^{H/2}(x_2\tau_{2,2}+\tau_2)\,\mathrm{d}x_2. \tag{4.63}$$

The second integral in Equation (4.63) vanishes irrespective of the material parameters and we are left with

$$M = \int_{-H/2}^{H/2} x_2 \sigma_{11} \, \mathrm{d}x_2. \tag{4.64}$$

This expression has exactly the same form as the classical bending moment. In the strain divergence theory, however, the vertical displacement field u_2 differs from that in classical elasticity due to the higher-order boundary conditions at the traction-free top and bottom surfaces. As a result, σ_{11} as given in Equations (4.57), is non-linear over the cross-section. In the following we will analyze the difference between the strain divergence and the classical solution for isotropic and transverse isotropic materials, for which the material constants C_{1111} and C_{1122} in Equations (4.57) follow from Equations (3.19) and (3.17), respectively. The ratio of σ_{11} for the strain divergence theory, $\sigma_{11}{}^{\mathrm{SD}}$, to the corresponding one for the classical continuum theory, $\sigma_{11}{}^{\mathrm{C}}$, can be written for isotropic materials as

$$\frac{\sigma_{11}{}^{\mathrm{SD}}}{\sigma_{11}{}^{\mathrm{C}}} = 1 + \frac{(1 - f_{,2} / \varepsilon_{22}{}^{\mathrm{C}}) \nu^2}{1 - 2\nu}, \tag{4.65}$$

and for transverse isotropic materials (with a zero out-of-plane Poisson's ratio, $\nu_{\mathrm{pt}} = 0$), as

$$\frac{\sigma_{11}{}^{\mathrm{SD}}}{\sigma_{11}{}^{\mathrm{C}}} = \frac{1 - (f_{,2} / \varepsilon_{22}{}^{\mathrm{C}}) \nu_{\mathrm{p}}{}^2}{1 - \nu_{\mathrm{p}}{}^2}. \tag{4.66}$$

Here, $\varepsilon_{22}{}^{\mathrm{C}}$ is the classical strain field and ν_{p} the in-plane Poisson's ratio. Note that $f_{,2}/\varepsilon_{22}{}^{\mathrm{C}}$ depends on the Poisson's ratio and the characteristic length. For a vanishing characteristic length, f falls back onto its classical counterpart (see Equation (4.60)), as it should be. For zero Poisson's ratio, $\sigma_{11}{}^{\mathrm{SD}}/\sigma_{11}{}^{\mathrm{C}} = 1$, irrespective of the value for the characteristic length. Figure 4.5a and b show $f_{,2}/\varepsilon_{22}{}^{\mathrm{C}}$ and $\sigma_{11}{}^{\mathrm{SD}}/\sigma_{11}{}^{\mathrm{C}}$, respectively, plotted against the normalized distance from the neutral axis, $2x_2/H$, on the upper half of the beam, for a transverse isotropic material with a characteristic length of $l_{\mathrm{c}} = 0.64d$ and for $H = 2d$. We see that $f_{,2}/\varepsilon_{22}{}^{\mathrm{C}}$ is between 0.3 and 0.4 for $\nu_{\mathrm{p}} = 0$ and converges to one as the value of ν_{p} approaches the incompressibility limit $\nu_{\mathrm{p}} = 1$. $\sigma_{11}{}^{\mathrm{SD}}/\sigma_{11}{}^{\mathrm{C}}$, on the other hand, is constant and equal to one throughout the whole beam for ν_{p} equal to zero. With increasing ν_{p}, the ratio increases uniformly over the cross-section until $\nu_{\mathrm{p}} \approx 0.7$. With a further increase of ν_{p}, $\sigma_{11}{}^{\mathrm{SD}}/\sigma_{11}{}^{\mathrm{C}}$ increases towards the top surface and falls back to one in the middle of the beam. For ν_{p} approaching the incompressibility limit, $\nu_{\mathrm{p}} = 1$, its value gets very large in a small region close to the top surface ($\sigma_{11}{}^{\mathrm{SD}}/\sigma_{11}{}^{\mathrm{C}} = 46$ at $\nu_{\mathrm{p}} = 0.9999$). The tendencies are the same in the case of isotropic solids, and will not be shown here.

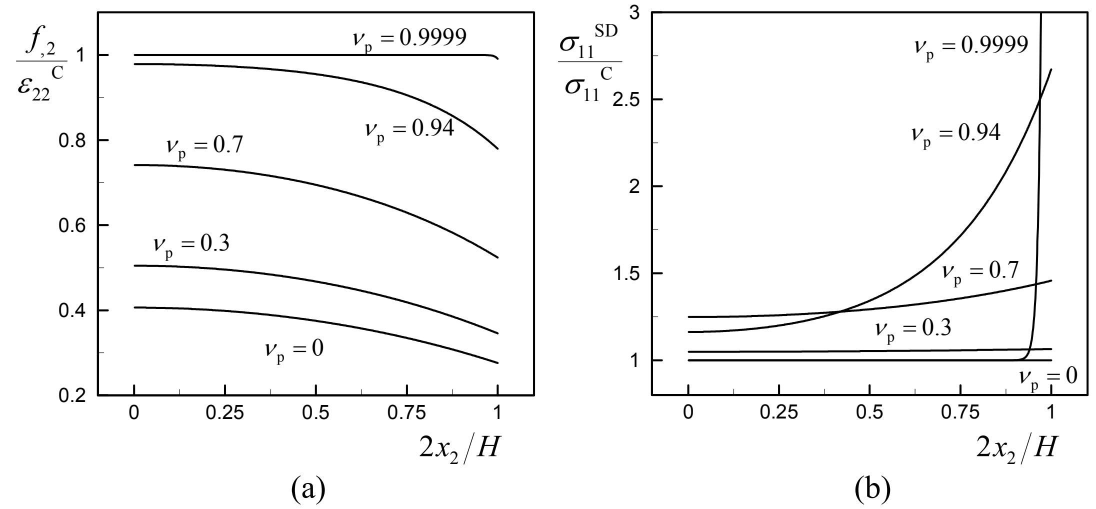

Figure 4.5: The ratio of (a) the transverse strain ($f_{,2}$) and (b) the normal stress ($\sigma_{11}{}^{\mathrm{SD}}$) given by the strain divergence theory to their classical counterparts ($\varepsilon_{22}{}^{\mathrm{C}}$ and $\sigma_{11}{}^{\mathrm{C}}$, respectively), for transverse isotropic materials with a characteristic length of $l_{\mathrm{c}} = 0.64d$, a height of $H = 2d$ and with different Poisson's ratios ranging from $\nu_{\mathrm{p}} = 0$ to $\nu_{\mathrm{p}} \approx 1$.

Multiplication of the bending moment with the radius of curvature R yields the bending stiffness. The bending stiffness of a classical isotropic continuum beam is

$$B_{\text{class}} = \frac{EH^3}{12(1-\nu^2)}. \tag{4.67}$$

To be able to write the normalized bending stiffness in a more convenient way, we will introduce a function $g(x_2)$ such that

$$g(x_2) = f(x_2)_{,2} + \frac{1}{R}\frac{C_{1122}}{C_{1111}}x_2. \tag{4.68}$$

Then, the normalized bending stiffness can be written as

$$\frac{B}{B_{\text{class}}} = 1 + \frac{12R\nu(1-\nu)}{(1-2\nu)H^3}\int_{-H/2}^{H/2} x_2 g \, \mathrm{d}x_2. \tag{4.69}$$

The corresponding solution for the transverse isotropic case (with a zero out of plane Poisson's ratio, $\nu_{\mathrm{pt}} = 0$), can be find in a similar manner as

$$\frac{B}{B_{\text{class}}} = 1 + \frac{12R\nu_p}{(1-\nu_p{}^2)H^3}\int_{-H/2}^{H/2} x_2 g \, \mathrm{d}x_2, \tag{4.70}$$

with the classical bending stiffness defined as

$$B_{\text{class}} = \frac{E_{\text{p}} H^3}{12} \,. \tag{4.71}$$

Figure 4.6 shows the normalized bending stiffness plotted as a function of the normalized height H/d, for an increasing Poisson's ratio for the couple stress theory (Equation (3.48)) and the strain divergence theory (Equation (4.70)). The characteristic length is taken to be the one obtained by fitting the continuum results of the shear problem to the corresponding discrete results of the Voronoi microstructures: $l_{\text{c}}^{\text{CS}} = 0.9d$ (corresponding to $l_{\text{c}}^{\text{SD}} = 0.64d$). We see that there is stiffening in the small H/d regime for both cases. The stiffening increases with increasing Poisson's ratio for the strain divergence case, whereas it decreases for the couple stress theory. For the same Poisson's ratio, the stiffening is larger for the couple stress solid, but the difference vanishes as we approach to the incompressibility limit $\nu_{\text{p}} = 1$. For Poisson's ratio's smaller than, say, $\nu_{\text{p}} < 0.7$, the stiffening for the strain divergence solution is small, whereas it is quite high for the couple stress solution.

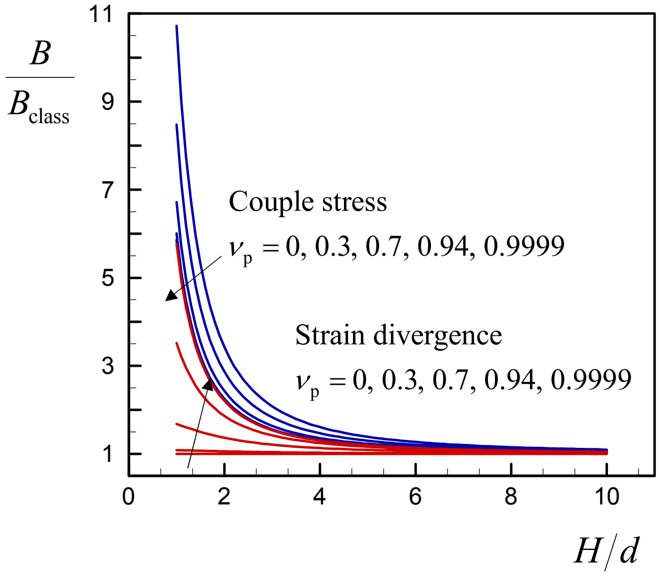

Figure 4.6: The normalized bending stiffness plotted as a function of the normalized height H/d, for an increasing Poisson's ratio, for the couple stress (in blue) and strain divergence (in red) theories. The arrows denote the direction of increasing ν_{p}.

4.6 Summary and conclusions

In this chapter we developed a higher-grade continuum theory that falls in the class of Toupin-Mindlin's strain gradient theories. The theory incorporates the divergence of strain to be the additional higher-grade kinematic measure. Fist, we derived the equilibrium equations and the boundary conditions for the strain divergence theory. We developed a finite element implementation of the theory making use of the penalty approach. Then, we solved the simple shear problem analytically and assessed the accuracy of the finite element method. The strain divergence and couple stress theory turn out to yield the same solution for the simple shear problem, provided that the characteristic length for the strain divergence solid l_c^{CS} is related to the characteristic length for the couple stress solid l_c^{CS} via $l_c^{SD} = l_c^{CS}/\sqrt{2}$.

In the plane strain bending of a classical solid, ε_{22} varies linearly through the thickness of the beam. In the case of a strain divergence solid, however, ε_{22} becomes non-linear (i.e. exponential) as a result of satisfying both the classical and additional higher-order boundary conditions. This difference in ε_{22} results in an increasing bending stiffness with decreasing specimen thickness, being larger for larger Poisson's ratios. Nevertheless, for the same Poisson's ratio, the stiffening of a strain divergence solid is less than the stiffening of a couple stress solid, with this difference being larger when the Poisson's ratio is low.

Appendix: Pure bending for the strain gradient theory

In this appendix we summarize the analytical solution of the plane-strain pure bending problem for Toupin-Mindlin's strain gradient theory. The geometry of the problem is shown earlier in Fig. 3.9. The displacement field that satisfies the pure bending assumption for the strain gradient elasticity is the same as given for the strain divergence theory in Equations (4.55). The corresponding non-vanishing in-plane strains and strain gradients (see Equations (1.13)) are

$$\begin{aligned} &\varepsilon_{11}=\frac{1}{R}x_2,\ \ \varepsilon_{22}=f_{,2},\\ &\eta_{211}=\frac{1}{R}\ \text{and}\ \eta_{222}=f_{,22}. \end{aligned} \tag{A1}$$

By inserting (A1) into the constitutive equations (1.15), the non-vanishing in-plane stresses and higher-order stresses are found as

$$\begin{aligned} \sigma_{11}&=C_{1111}\frac{x_2}{R}+C_{1122}f_{,2},\\ \sigma_{22}&=C_{1111}f_{,2}+C_{1122}\frac{x_2}{R},\\ \tau_{112}&=\left(\frac{1}{2}a_1+a_5\right)\frac{1}{R}+\left(\frac{1}{2}a_1+a_3\right)f_{,22},\\ \tau_{211}&=\left(a_2+a_4\right)\frac{2}{R}+\left(a_1+2a_2\right)f_{,22},\\ \tau_{222}&=\left(a_1+2a_2\right)\frac{1}{R}+2\left(a_1+a_2+a_3+a_4+a_5\right)f_{,22}. \end{aligned} \tag{A2}$$

The only non-trivial in-plane equilibrium equation is

$$\sigma_{22,2}-\tau_{222,22}=0, \tag{A3}$$

which combines with (A2) to yield the governing differential equation

$$2(a_1+a_2+a_3+a_4+a_5)f_{,2222}-C_{1111}f_{,22}-C_{1122}\frac{1}{R}=0. \tag{A4}$$

The solution of (A4) reads

$$f=\frac{2a_\mathrm{h}}{C_{1111}}\left(q_1 e^{\sqrt{\frac{C_{1111}}{2a_\mathrm{h}}}x_2}+q_2 e^{-\sqrt{\frac{C_{1111}}{2a_\mathrm{h}}}x_2}\right)-\frac{1}{2R}\frac{C_{1122}}{C_{1111}}x_2{}^2+q_3x_2+q_4, \tag{A5}$$

where $a_\mathrm{h}=a_1+a_2+a_3+a_4+a_5$. Combining the two constants q_4 in Equation (A5) and P in Equation (4.55) into a single constant B, we have four unknowns (q_1, q_2, q_3, B) to be determined from the boundary conditions. The non-trivial traction boundary conditions at the top and the bottom surfaces are

$$\begin{aligned} t_2 &= \pm(\sigma_{22}-\tau_{222,2})=0 \quad \text{at} \quad x_2=\pm H/2\,, \\ r_2 &= \tau_{222}=0 \quad \text{at} \quad x_2=\pm H/2\,. \end{aligned} \tag{A6}$$

The first two equations ($t_2=0$ at ± H/2) are not linearly independent, which leaves only 3 independent equations. The fourth equation comes from specifying the displacement u_2 to be zero at $x_1=x_2=0$. Solving the four equations for the four unknowns yields

$$q_1=q_2=-\frac{BC_{1111}}{4a_h}=-\frac{(a_1+2a_2)C_{1111}-2a_\mathrm{h}C_{1122}e^{\sqrt{\frac{C_{1111}}{8a_h}}H}}{2a_\mathrm{h}C_{1111}R\left(e^{\sqrt{\frac{C_{1111}}{2a_h}}H}+1\right)}\,, \quad q_3=0. \tag{A7}$$

In the case of the strain gradient elasticity, the line forces s_k acting at the sharp edges read

$$s_k=z_j n_i \tau_{ijk}, \tag{A8}$$

which reduce to $(s_1, s_2, s_3)=(\tau_{112}+\tau_{211}, 0, 0)$ at $x_2=H/2$ and $(s_1, s_2, s_3)=(-\tau_{112}-\tau_{211}, 0, 0)$ at $x_2=-H/2$ for the out-of-plane edges of a cross-section perpendicular to the length of the beam. By inserting these and the (higher-order) tractions in the external work expression (4.18), the macroscopic bending moment per unit out-of-plane thickness can be written as

$$\begin{aligned} M = &\int_{-H/2}^{H/2} x_2\sigma_{11}\,\mathrm{d}x_2-\int_{-H/2}^{H/2}\left(x_2(\tau_{211,2}+\tau_{112,2})+\tau_{112}\right)\mathrm{d}x_2 \\ &+\frac{H}{2}\left(\tau_{112}\,|_{x_2=H/2}+\tau_{211}\,|_{x_2=H/2}\right)+\frac{H}{2}\left(\tau_{112}\,|_{x_2=-H/2}+\tau_{211}\,|_{x_2=-H/2}\right). \end{aligned} \tag{A9}$$

Multiplying the bending moment with the radius of curvature R yields the bending stiffness.

5

Higher-order effects on the strain distribution around a cylindrical hole

In this chapter, we investigate the plain-strain problem of a circular cylindrical hole in an infinitely large block under a field of uniaxial tension. First, we analyse the analytical solutions for the strain divergence, couple stress and classical theories. Then, we perform discrete analyses on Voronoi samples and compare the results with the continuum solutions. Finally, we critically assess whether the generalized continuum theories can capture the effect of the hole size (relative to the cell size) on the strain distribution around the hole.

5.1 Introduction

The effects of a hole on the strain/stress distribution in a solid material, which is uniform at points distant from the hole, is of great practical importance for the engineer; the strain/stress concentration induced by the hole may initiate fracture at the overstrained/overstressed portions close to the hole boundary. The classical continuum solution for circular cylindrical holes gives good agreement with experiments on conventional dense metals if the hole is large enough compared to the grain size of the crystalline aggregate (see Timoshenko and Goodier [1970] and the references therein). However, the classical theory is size-independent and the effect of the hole size relative to the size of the micro-constituents is absent in the solution. To capture possible hole size effects, one need to employ a generalized continuum theory.

The effects of the hole size on the overall properties and the local strain fields have been investigated experimentally for cellular metals and polymers (see e.g. Fleck *et al.* [2001], Paul *et al.* [1999], Mora and Waas [2000] and Dillard *et al.* [2006]). Mora and Waas [2000] investigated the strain concentration around a circular cylindrical hole in a polycarbonate honeycomb. They were not able to detect any size effects for the hole problem, in contrast to the case of a rigid circular inclusion. In that case they were able to fit the experimental results by using the couple stress theory. Dillard *et al.* [2006] studied the strain fields around a hole in an open-cell nickel foam. They concluded that the strain concentration around the hole is closely related to the hole size relative to the cell size: for large hole sizes the experimental results agreed with classical continuum theory. For a hole size comparable to the cell size, however, they did not observe any strain concentration.

Our aim in this chapter is to investigate the effects of the hole size (relative to the cell size) on the strain distribution in an infinite elastic block under uniaxial tension. In section 5.2, we first summarize the analytical solution for the strain gradient theory, which we use to obtain the corresponding solution for the strain divergence theory. Then, we compare the analytical solutions for the strain divergence, couple stress and classical theories. In section 5.3, we perform finite element calculations on discrete Voronoi models containing holes with different radii. We extract the strain distribution throughout the samples from the nodal displacements given by the finite element calculations by applying a strain mapping procedure developed earlier in section 3.4.2. In section 5.4, we compare the analytical and discrete results, in terms of the strain concentration around the hole, both qualitatively and quantitatively. Finally, we summarize this chapter and discuss the results in section 5.5.

5.2 Strain divergence and couple stress solutions

In this section, we discuss the analytical solutions of a hole in a strain divergence and a couple stress material subjected to a far-field uniaxial stress state. We will compare these solutions with the classical field through the relevant dimensionless parameters.

The governing equations of the strain gradient theory, for an isotropic body with a smooth bounding surface, are given in section 1.3.2. If we insert the kinematics (1.13) into the equilibrium equations (1.19a) via the constitutive relations (1.15), we obtain the displacement equations of equilibrium

$$(\lambda+2\mu)(1-l_1^2\nabla^2)\nabla\nabla\bullet\boldsymbol{u}-\mu(1-l_2^2\nabla^2)\nabla\times\nabla\times\boldsymbol{u}=0, \tag{5.1}$$

with

$$l_1^2=2\,\frac{a_1+a_2+a_3+a_4+a_5}{\lambda+2\mu}\ \text{ and }\ l_2^2=\frac{a_3+2a_4+a_5}{2\mu}, \tag{5.2}$$

where $\boldsymbol{u}$ is the displacement vector, ∇ is the gradient operator, ∇^2 is the Laplacian operator (see the Appendix for its definition) and l_1 and l_2 are the two characteristic lengths of a strain gradient material. Note that any kinematically admissible displacement field for an isotropic strain gradient material must satisfy Equation (5.1).

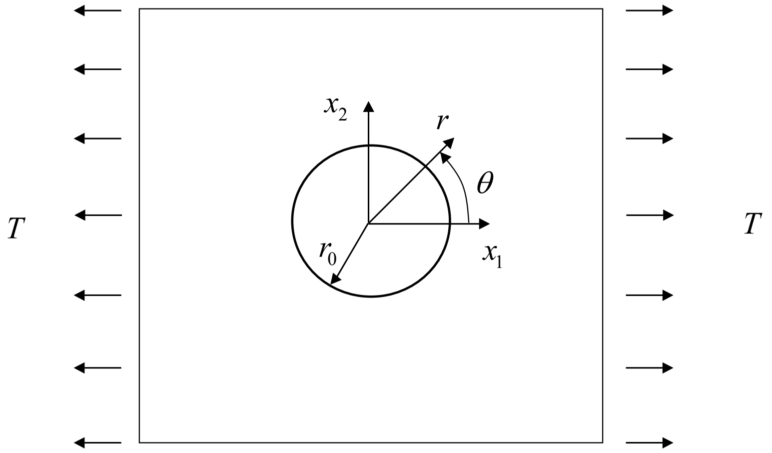

Figure 5.1: Notation and geometry of an infinite plane with a circular cylindrical hole subjected to remotely uniform tension.

Figure 5.1 shows the boundary conditions corresponding to the plane-strain problem of a circular cylindrical hole (in an infinitely large block) under a field of uniaxial tension. Eshel and Rosenfeld [1970] obtained the solution $\boldsymbol{u}$ of the partial differential equation (5.1) for these boundary conditions (a brief summary of their solution is given in the Appendix), and showed that the solution depends on five independent and dimensionless parameters, namely,

$$\begin{aligned} &\nu=\frac{\lambda}{2(\lambda+\mu)},\ \beta_1=\frac{\alpha_0}{2\alpha_1},\ \beta_2=\frac{\alpha_2}{2\alpha_1}, \\ &\gamma=\frac{p_2}{p_1}=\left(\frac{2\alpha_1}{\lambda+2\mu}\frac{2\mu}{\alpha_3}\right)^{\frac{1}{2}},\ p_1=\frac{r_0}{l_1}\ (\text{or}\ p_2=\frac{r_0}{l_2}), \end{aligned} \tag{5.3}$$

with

$$\begin{aligned} &\alpha_0=r_0^{-2}(a_4+a_5), \quad \alpha_1=r_0^{-2}(a_1+a_2+a_3+a_4+a_5), \\ &\alpha_2=r_0^{-2}(a_1+2a_2),\ \alpha_3=r_0^{-2}(a_3+2a_4+a_5), \end{aligned} \tag{5.4}$$

where ν is the Poisson's ratio and r_0 is the hole radius.

As mentioned earlier in section 4.2, the strain gradient theory reduces to the strain divergence theory if the four higher-order constants (a_1, a_2, a_4, a_5) vanish, with $a_3=a$. In this case, β_1 and β_2 are zero, we have a single characteristic length l_{c} as defined in Equation (4.47) and, as a result, p_1 and p_2 are no longer independent (see Equations (5.3)). This leaves only two independent parameters that enter the solution, namely,

$$\nu=\frac{\lambda}{2(\lambda+\mu)}\ \text{and}\ p=\frac{r_0}{l_{\mathrm{c}}}. \tag{5.5}$$

The solution to the same problem is given by Eringen [1999] for the micropolar theory, and by Mindlin [1963] for the couple stress theory. Since the couple stress theory is a special case of both the micropolar and strain gradient theories (see table 1.1), the solution can also be obtained from the micropolar solution by imposing $m\to\infty$ (see section 3.3) or from the strain gradient solution by performing the reduction as discussed in section 1.3.2. Similar to the strain divergence theory, the couple stress solution depends on the two dimensionless parameters given in Equations (5.5), with the corresponding couple stress characteristic length[1]. As it would be expected, for $p\to\infty$ (or $l_{\mathrm{c}}\to 0$), the solution converges to the solution of the

---

[1] Note that Mindlin's definition for the couple stress characteristic length is $l_{\mathrm{c}}=(D_{1313}/2A_{1212}^{(1)})^{1/2}$. Therefore, the characteristic length that we defined in Equation (3.26), i.e. $l_{\mathrm{c}}=(D_{1313}/A_{1212}^{(1)})^{1/2}$ should be divided by $\sqrt{2}$ when using Mindlin's [1963] solution.

same problem in classical elasticity, for both theories. We note in passing that the related problem of a cylindrical rigid inclusion in a field of uniaxial tension is investigated for the couple stress theory by Hartranft and Sih [1965] and by Weitsman [1965]. The more general cases of spherical and cylindrical elastic inclusions are analyzed for the micropolar theory by Zhang and Sharma [2005].

As discussed in detail in section 3.2, the discrete cellular structures analyzed are transverse isotropic with a zero out-of-plane Poisson's ratio ($\nu_{\mathrm{pt}}=0$). The equations for a plane-strain isotropic problem (Equations (5.1-5) in this case) can simply be converted to their transverse isotropic (with $\nu_{\mathrm{pt}}=0$) counterparts by replacing μ with μ_{p} and λ with λ_{p}. In the following, the results are given for transverse isotropic materials (with $\nu_{\mathrm{pt}}=0$).

Figures 5.2a-f show the effects of the (in-plane) Poisson's ratio, ν_{p}, and p (the ratio of the hole size r_0 to the characteristic length l_{c}) on the distribution of the strain component ε_{11}, normalized by the applied strain $\varepsilon_{\mathrm{appl}}$ (i.e. the strain ε_{11} applied far away from the hole). Figures 5.2a, c and e (5.2b, d and f) are for a classical, strain divergence and couple stress solid, respectively, and all three solids have a Poisson's ratio of $\nu_{\mathrm{p}}=0.3$ ($\nu_{\mathrm{p}}=0.94$). The classical case corresponds to $p\rightarrow\infty$, and for the strain divergence and the couple stress solids p is taken to be equal to one, small enough to exemplify the higher order effects. The value $\nu_{\mathrm{p}}=0.3$ represents a low Poisson's ratio solid, whereas $\nu_{\mathrm{p}}=0.94$ is the value for the Voronoi honeycombs analyzed discretely in chapter 2. Due to the symmetries of the problem, only the upper right quarter is shown in Figs. 5.2a-f. For all six cases it holds that the effect of the hole on the strain distribution is localized in a regime near its boundary; the value of the strain ε_{11} rapidly approaches the applied strain $\varepsilon_{\mathrm{appl}}$ moving away from the hole. For the classical solid, the strain concentration factor at the edge of the hole at $\theta=\pi/2$ does not depend on ν_{p} and is equal to $\varepsilon_{11}/\varepsilon_{\mathrm{appl}}=3$ (see Figs. 5.2a and b). The strain distribution around the hole, however, is quite sensitive to the value of ν_{p}. Along the line $\theta=\pi/2$, ε_{11} approaches $\varepsilon_{\mathrm{appl}}$ faster for the larger Poisson's ratio ($\nu_{\mathrm{p}}=0.94$), whereas at approximately $\theta=\pi/4$, it approaches $\varepsilon_{\mathrm{appl}}$ slower. For the strain divergence solid, the strain concentration factor ($\varepsilon_{11}/\varepsilon_{\mathrm{appl}}$ at $x_2=r_0$ and $\theta=\pi/2$) decreases with increasing ν_{p} ($\varepsilon_{11}/\varepsilon_{\mathrm{appl}}\approx 2.92$ for $\nu_{\mathrm{p}}=0.3$, and $\varepsilon_{11}/\varepsilon_{\mathrm{appl}}\approx 2.34$ for $\nu_{\mathrm{p}}=0.94$), whereas the strain concentration remains more localized around the hole (see Figs. 5.2c and d). For decreasing ν_{p}, the solution for a strain divergence solid converges to the solution for a classical solid (with the same ν_{p}), irrespective of the value of p; for $\nu_{\mathrm{p}}=0$, the two solutions are the same. Clearly, a non-zero value of ν_{p} is needed to trigger higher-order effects in the case of the strain divergence theory. A similar effect was observed in pure bending (see Fig. 4.6). In the case of the couple stress solid, on the other hand,

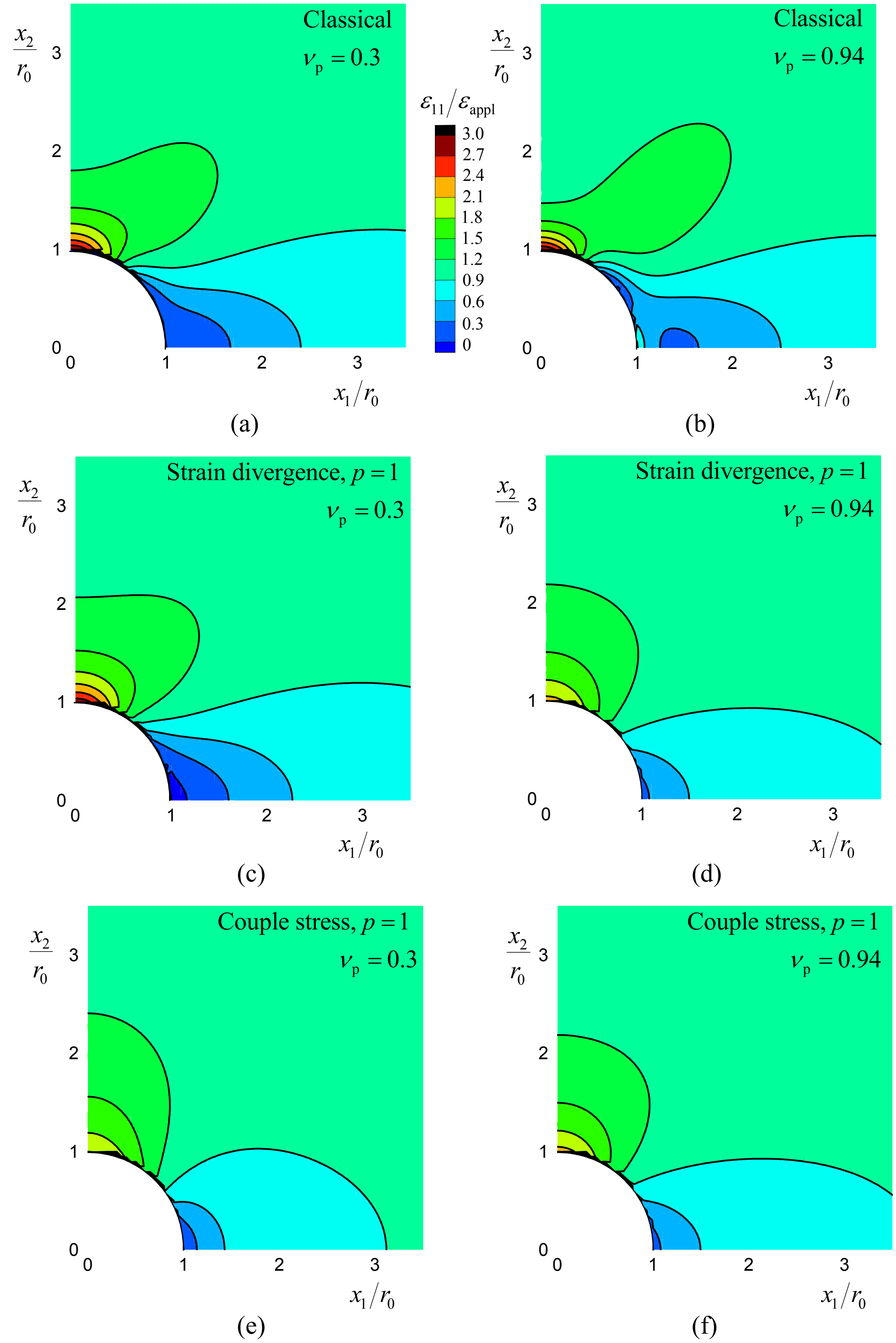

Figure 5.2: The effects of the (in-plane) Poisson's ratio, ν_p, and p (the ratio of the hole size r_0 to the characteristic length l_c) on the distribution of the strain component ε_{11}, normalized by the

applied strain $\varepsilon_{\mathrm{appl}}$ (i.e. the strain ε_{11} applied far away from the hole) for a classical, (a) and (b), strain divergence, (c) and (d), and for a couple stress solid, (e) and (f). (a), (c) and (e) are for a Poisson's ratio of $\nu_{\mathrm{p}} = 0.3$ and (b), (d) and (f) for a Poisson's ratio of $\nu_{\mathrm{p}} = 0.94$.

there is an opposite tendency in the value of the strain concentration factor ($\varepsilon_{11}/\varepsilon_{\mathrm{appl}}$ at x_2=r_0 and θ=π/2); it increases with increasing ν_{p} ($\varepsilon_{11}/\varepsilon_{\mathrm{appl}}$≈2.02 for ν_{p}=0.3 and $\varepsilon_{11}/\varepsilon_{\mathrm{appl}} \approx 2.22$ for $\nu_{\mathrm{p}} = 0.94$, see Figs. 5.2e and f). For the same p and ν_{p} values, the strain concentration factor at the edge of the hole is lower for the couple stress solid than for the strain divergence solid. The difference between the two cases diminishes as the Poisson's ratio approaches the incompressibility limit $\nu_{\mathrm{p}} \rightarrow 1$, at which value they are very different from the classical solution (compare Figs. 5.2b, d and f). In summary, for low Poisson's ratio materials, the couple stress field is very different from the strain divergence field (which closely resembles the classical field), whereas they are very similar for large Poisson's ratio materials, in which case they differ considerably from the classical field.

The differences between the classical and the higher order/grade solutions are associated with the additional deformation mechanisms appearing in the theory: the divergence of strain for the strain divergence theory and the gradient of the (macro-) rotation for the couple stress theory. To exemplify this, we show the contour plots of one component of the strain divergence, η_1 (and one component of the curvature, k_{13}) for the classical and strain divergence (couple stress) theories in Fig. 5. The Poisson's ratio is $\nu_{\mathrm{p}} = 0.94$ for each case and $p = 1$ for both the strain divergence and couple stress solutions. It is clear that both η_1 and k_{13} in the classical case (see Figs. 5.3a and c) are much larger compared to those for the strain divergence and couple stress solutions, respectively (see Figs. 5.3b and d). This is caused by the increase in the characteristic length l_{c} (or decrease in $p = r_0/l_{\mathrm{c}}$) from the classical to the strain divergence (couple stress) solution, putting an energy penalty on the development of

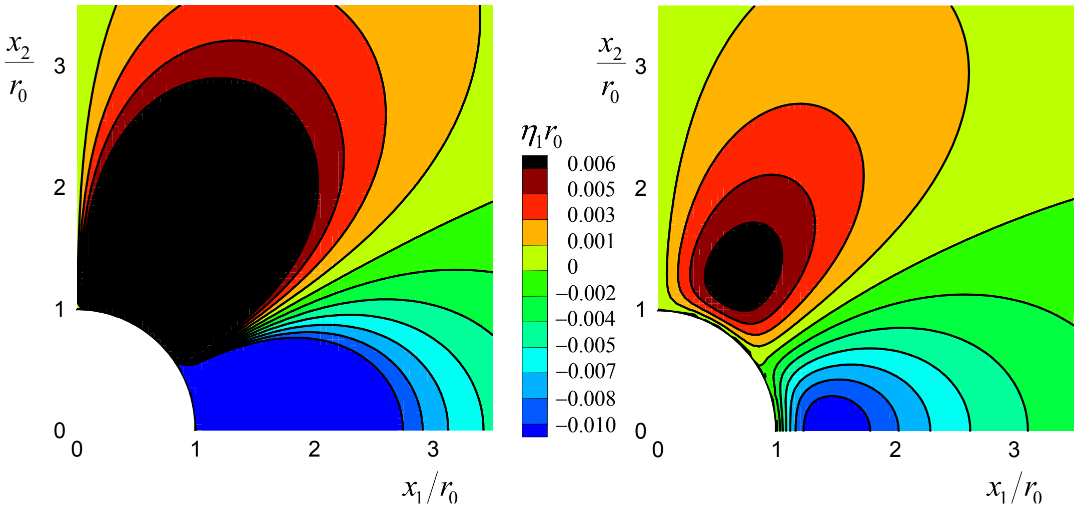

(a) (b)

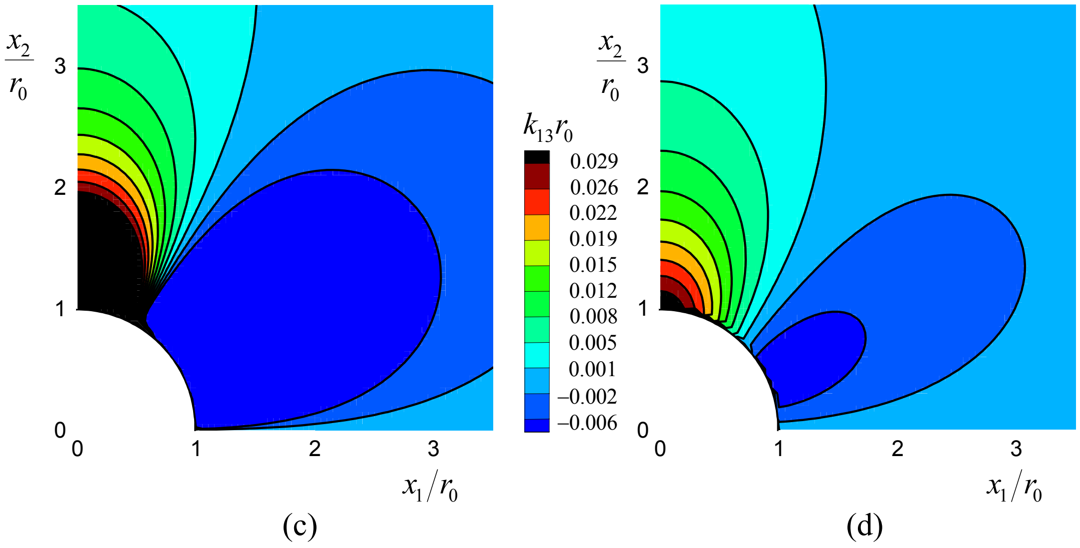

Figure 5.3: Contour plots of one component of the strain divergence, η_1, (a) and (b), and one component of the curvature, k_{13}, (c) and (d). (a) and (c) are for a classical, (b) is for a strain divergence solid with $p = 1$ and (d) is for a couple stress solid with $p = 1$, each with a Poisson's ratio of $\nu_p = 0.94$.

the divergence of strain and the gradient of the (macro-) rotation. The other two in-plane components, η_2 and k_{23}, show a similar behaviour and are not presented here.

5.3 Discrete analyses

In this section, we discretely analyze the hole problem for Voronoi tessellations (see Fig. 5.4). The Voronoi microstructure is similar to the one used in section 2.3. To be able to mimic a hole in an infinite block, the size of the samples should be large enough compared to the hole radius r_0. It was found that for $L \approx 5\text{–}6r_0$, the effect of

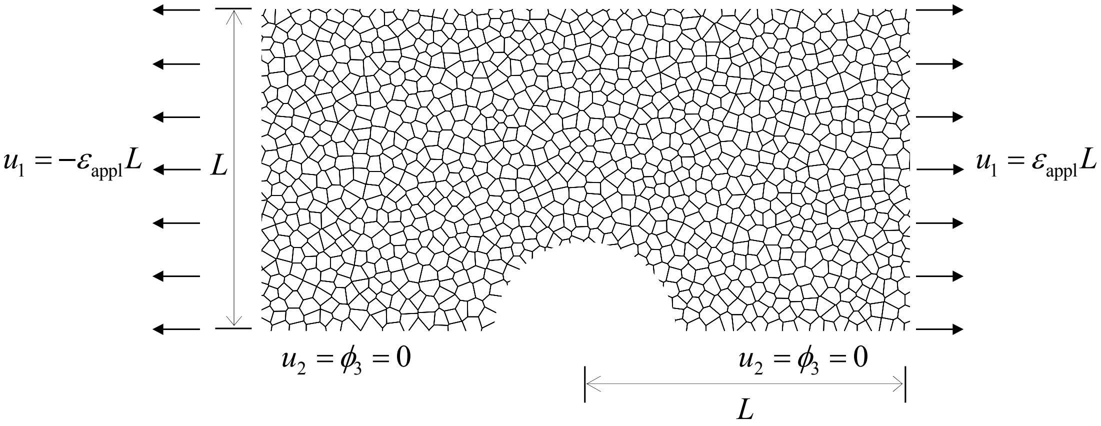

Figure 5.4: Geometry and boundary conditions for the discrete analysis of a circular cylindrical hole subjected to remotely uniform tension.

the hole on the macroscopic stiffness is negligible. Owing to the symmetries of the problem (see Fig. 5.1), it is essentially enough to model only a quarter of the specimens. However, we take a full length sample in the x_1 direction (the direction of the applied tensile strain, $\varepsilon_{\text{appl}}$) to avoid underestimated strain values along the line $\theta = \pi/2$, which could arise in the strain mapping procedure that will be employed (for a discussion on this, see section 3.4.2). We apply symmetry boundary conditions at the bottom boundary (along the line $\theta = 0$ and line $\theta = \pi$, for $x_1 > r_0$). Note that we do not account for the symmetry in the cellular structure at these locations. Nevertheless, the error was found to be negligible.

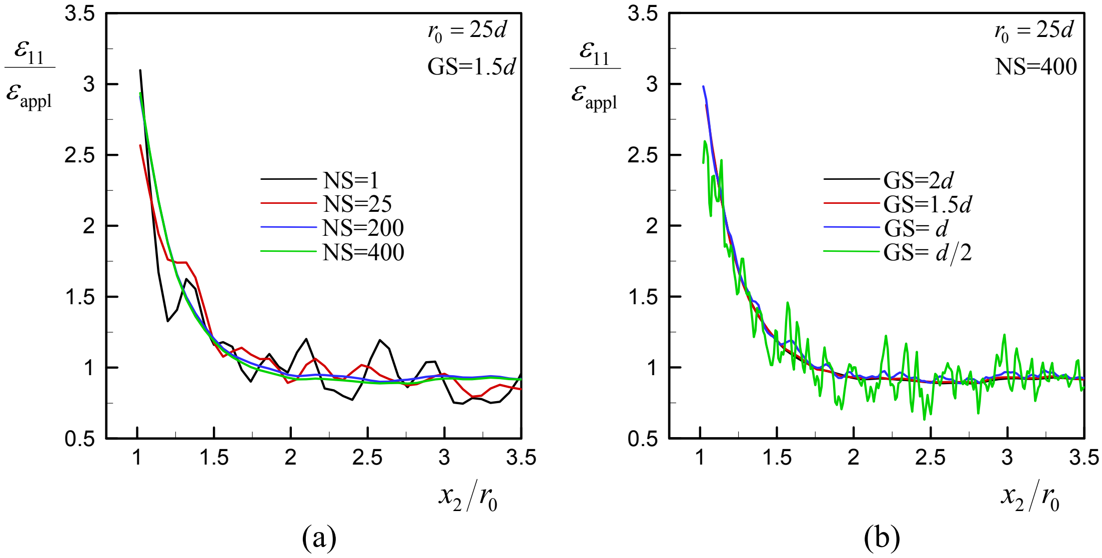

Figure 5.5: The normalized strain $\varepsilon_{11}/\varepsilon_{\text{appl}}$ over the line $\theta = \pi/2$, plotted against the normalized distance from the edge of the hole x_2/r_0, for (a) a fixed grid size GS = 1.5d and increasing number of samples NS and (b) NS = 400 and a decreasing grid size GS.

In section 3.4.2 it was shown that the accuracy of the strain mapping procedure is determined by three parameters, the cutting step size CSS for the samples, the number of samples NS used for the simulations and the grid size GS of the square background mesh. To accurately pick-up the gradients for the different hole sizes, these parameters should be carefully selected. In the following we will discuss the procedure adopted to do so. As a reference case we analyze a hole with radius $r_0 = 25d$ (d is the average cell size for the Voronoi samples), which is large enough so that higher-order effects will not be present. This allows benchmarking the discrete strain maps against the analytical results of classical elasticity. Each sample is cut from a big block with CSS $\approx 0.4d$. Figure 5.5a shows the normalized strain $\varepsilon_{11}/\varepsilon_{\text{appl}}$ over the line $\theta = \pi/2$, plotted against the normalized distance from the edge of hole, for a fixed grid size GS=1.5d and increasing number of samples NS. We clearly

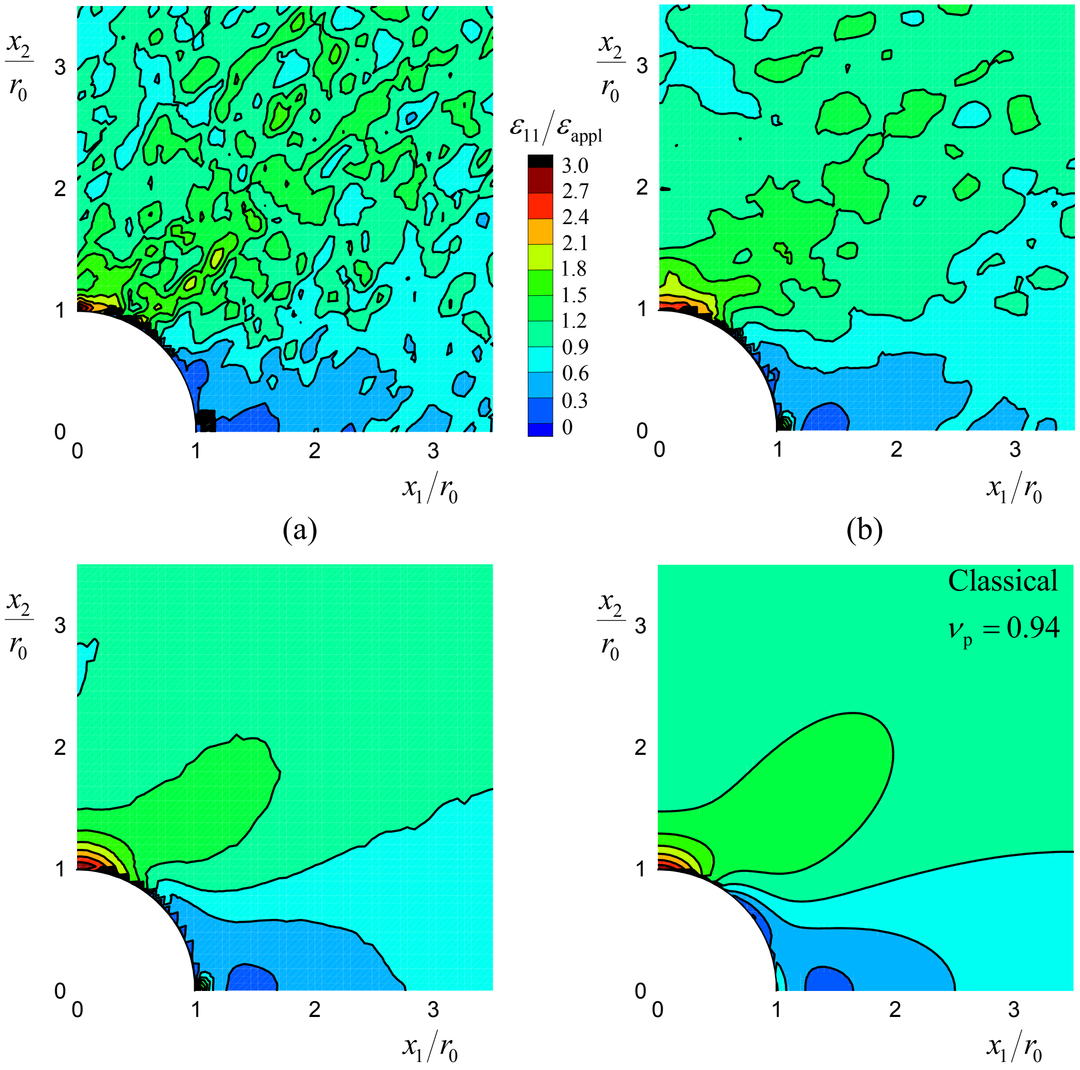

(a) (b) (c) (d)

Figure 5.6: The strain field ε_{11} normalized with the applied strain $\varepsilon_{\text{appl}}$ for $r_0 = 25d$: (a) 1 sample. (b) 25 samples. (c) 400 samples. (d) The classical continuum solution ($\nu_{\text{p}} = 0.94$).

see that a converged field is obtained for NS larger than 200 that exactly coincides with the analytical solution of classical elasticity. To also investigate this convergence spatially around the hole, we present contour plots of the strain field $\varepsilon_{11}/\varepsilon_{\text{appl}}$ in Fig. 5.6a-c for NS = 1, 25 and 400 samples, respectively. We see that there are large fluctuations for a single sample, which decreases for 25 samples and finally, for 400 samples, we obtain a smooth field that is in very good agreement with the classical solution, shown in Fig. 5.6d.

Next, we fix the number of samples NS and investigate the effect of the grid size GS. Figure 5.5b shows the strain fields along the line $\theta = \pi/2$, plotted against the normalized distance from the hole for a fixed number of samples (NS = 400) and a varying GS. The figure nicely depicts that for the grid sizes chosen the average strain field is accurately picked-up. For this number of samples, the smallest grid size (GS = $d/2$) induces fluctuations around the exact field, while by increasing the grid size further beyond $2d$ (not shown) the strain fields are smoothed out to such an extent that the gradients can no longer be picked-up. Clearly, to have a converged discrete strain field, the GS must be small enough to pick-up the gradients, while the NS must be large enough to smooth out fluctuations. In other words, if for a certain NS a reduction of the GS does not change the recorded field, a converged solution is obtained. This procedure will be employed in the following to find the NS and GS for each hole size investigated.

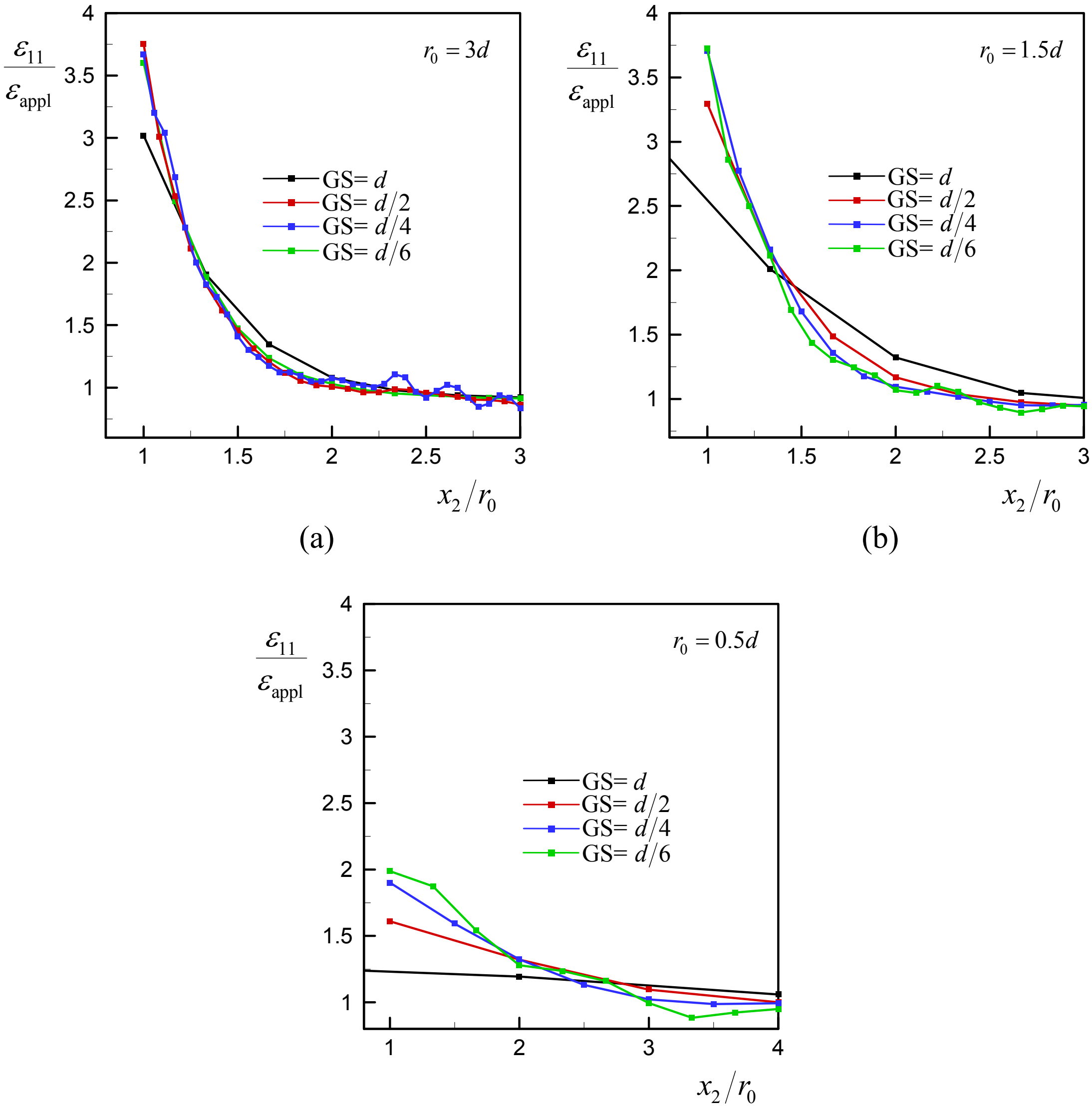

(a) (b)

(c)

Figure 5.7: The strain fields along the line $\theta = \pi/2$, plotted against the normalized distance from the hole x_2/r_0, for a fixed number of samples NS and a varying grid size GS for: (a) $r_0 = 3d$ (NS = 15000). (b) $r_0 = 1.5d$ (NS = 15000). (c) $r_0 = 0.5d$ (NS = 13000).

The discrete results are expected to diverge from the classical solution for small hole sizes, where r_0 is on the order of the cell size. Hence, we analyzed the cases of $r_0=6d$, $3d$, $1.5d$ and $0.5d$. In the simulations, we used 13000 samples for $r_0=0.5d$ and 15000 samples for the others. We first generated 3000 different Voronoi blocks and cut 4-5 samples from each with a CSS $= 0.5d$. Figures 5.7a-c show $\varepsilon_{11}/\varepsilon_{\text{appl}}$ over the line $\theta=\pi/2$, plotted against x_2/r_0 for a decreasing GS and for $r_0=3d$, $1.5d$ and $0.5d$, respectively. Already for $r_0=6d$, the discrete results converge to the classical solution, and therefore the results (which do not differ much from those for $r_0=25d$) are not plotted here. For the $r_0=3d$ and $1.5d$ cases, it can be observed that the gradient in $\varepsilon_{11}/\varepsilon_{\text{appl}}$ can not be picked-up for the largest grid size (GS $= d$). With decreasing GS, the fields converge. A further decrease in GS does not change the average gradient in $\varepsilon_{11}/\varepsilon_{\text{appl}}$ but causes oscillations around the converged field. For the $r_0=0.5d$ case, the strain concentration is drastically reduced. The two largest grid sizes are not sufficiently small to pick up the gradients. Although the convergence is not as clear as in the other two cases, the fact that the results for GS $= d/6$ start to oscillate around the GS $= d/4$ case suggests that the results for GS $= d/4$ are representative for the discrete fields. To obtain more accurate fields, the number of samples NS should be drastically increased. Yet, we do not expect qualitative changes in the results with a smaller GS.

5.4 Comparison of the analytical and discrete models

In this section we compare the discrete results with the strain divergence and couple stress solutions. As we showed in section 5.1, we need two parameters for the analytical solutions: ν_{p} and p. The Poisson's ratio $\nu_{\text{p}}=-\varepsilon_{22}/\varepsilon_{11}=0.94$ is obtained by performing uniaxial tension tests in the x_1 direction on Voronoi samples without a hole and measuring the average strains ε_{22} and ε_{11} by using the strain mapping procedure. For the parameter $p=r_0/l_{\text{c}}$, the characteristic length l_{c} is used that has been obtained by fitting the simple shear calculations, $l_{\text{c}}^{\text{SD}}=0.64d$ for the strain divergence theory (see section 4.4) and $l_{\text{c}}^{\text{CS}}=0.9d$ for the couple stress theory (see section 3.4.1). To analyze qualitatively the spatial distribution of the strain field, we show contour plots of $\varepsilon_{11}/\varepsilon_{\text{appl}}$ for the discrete models for $r_0=0.5d$ (with GS $= d/4$ and NS $= 13000$, Fig. 5.8a) and $r_0=3d$ (with GS $= d/2$ and NS $= 15000$, Fig. 5.8c), next to the corresponding strain divergence continuum solution (Figs. 5.8b and d, respectively). Figures 5.8a and b show that the discrete results are in reasonable good agreement with the strain divergence solution and both differ considerably from the classical solution (Fig. 5.2b). For $r_0=3d$, the discrete and strain divergence solutions (Figs. 5.8c and d, respectively) already closely resemble the classical solution (Fig. 5.2b). The couple stress fields are almost perfectly identical to the strain divergence fields (as also discussed in section 5.2) and are not shown here.

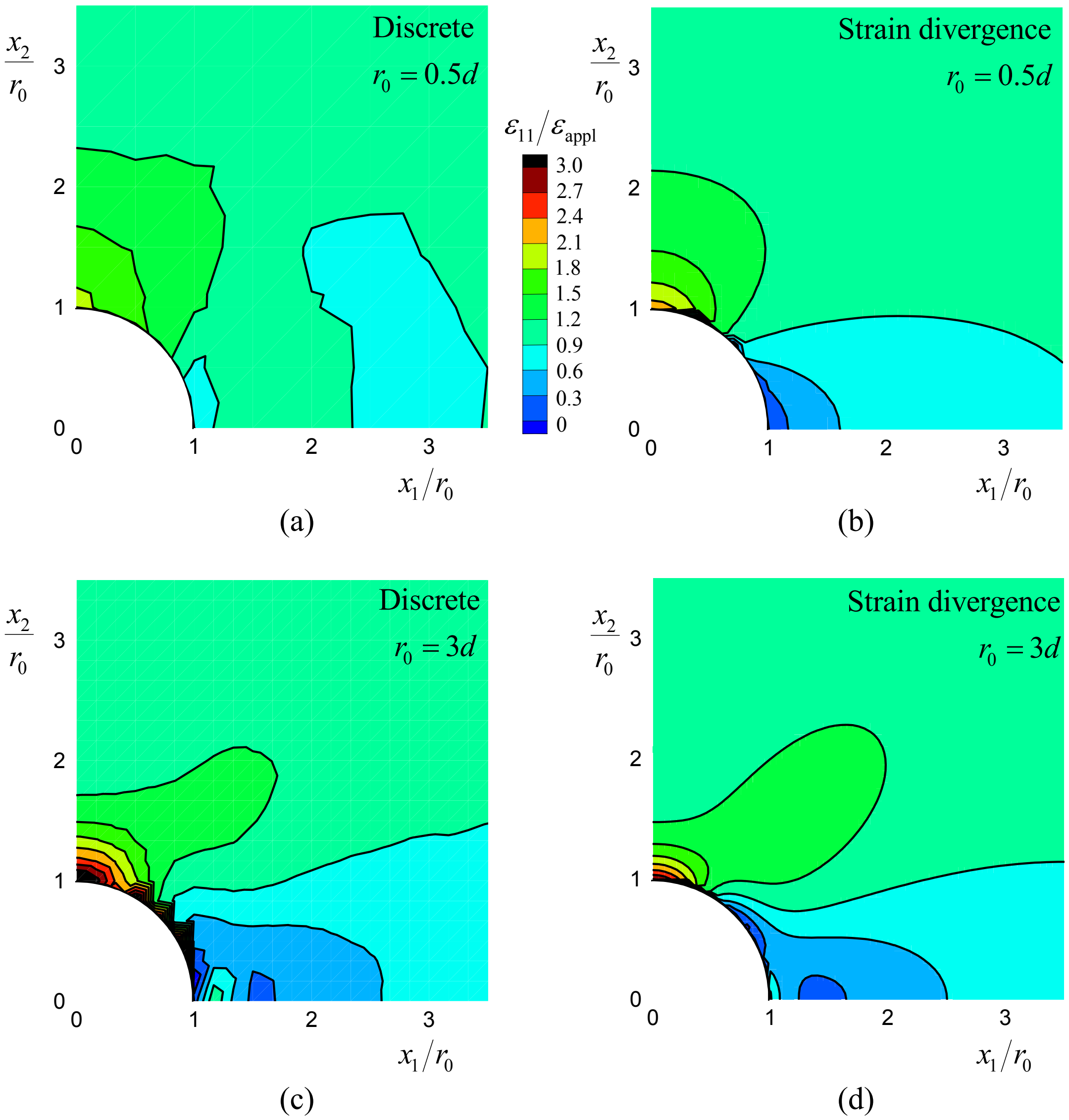

Figure 5.8: Comparison of $\varepsilon_{11}/\varepsilon_{\mathrm{appl}}$ for the discrete models with (a) $r_0 = 0.5d$ (GS = $d/4$ and NS = 13000) and (c) $r_0 = 3d$ (GS = $d/2$ and NS = 15000) with the corresponding strain divergence continuum solutions (with $\nu_p = 0.94$ and $l_c^{SD} = 0.64d$), (b) and (d).

Figures 5.9a and b show the discrete results for different hole sizes and the corresponding strain divergence solutions (with $l_c^{SD} = 0.64d$) for $\varepsilon_{11}/\varepsilon_{\mathrm{appl}}$ over the line $\theta = \pi/2$. It can be observed that the strain concentration factor at the edge of the hole for the strain divergence theory is equal to 3 for the largest hole radius, $r_0 = 25d$, and it decreases with decreasing r_0 value (Figs. 5.9b). For the discrete results there is no such a tendency and the strains obtained are larger than the continuum measures (Figs. 5.9a). For the discrete samples, the cell walls connected to the hole boundary are traction free, and as a result, the cells contiguous to the hole are more compliant compared to the ones located away from the hole. This might result in an overestimation of the strains. Moving further away from the hole, however, this effect

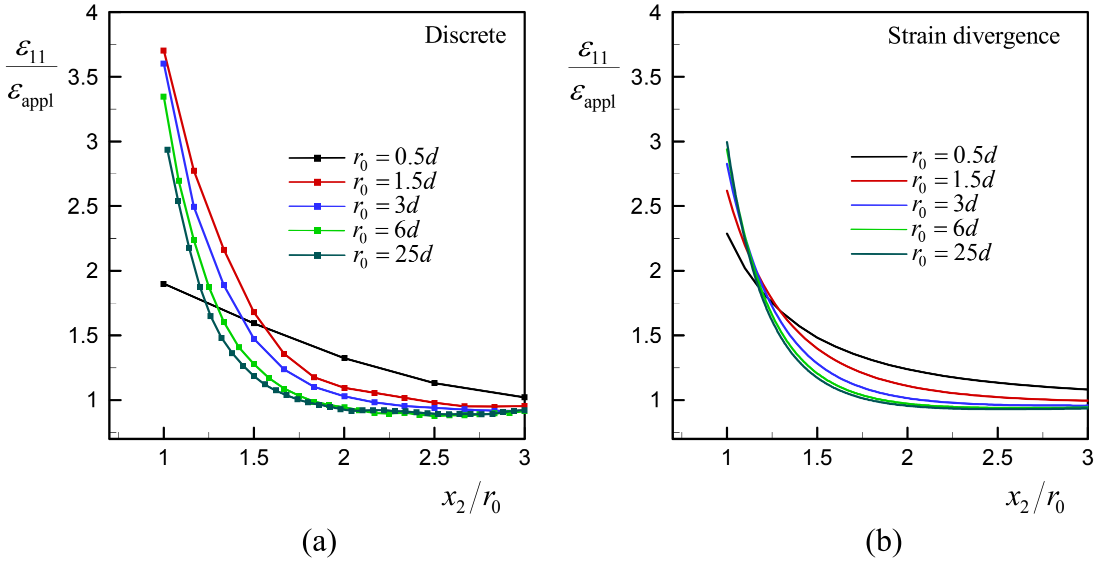

Figure 5.9: Comparison of (a) the discrete results for different hole sizes and (b) the corresponding strain divergence solutions (with $l_c^{SD} = 0.64d$) for $\varepsilon_{11}/\varepsilon_{appl}$ over the line $\theta = \pi/2$.

diminishes and the discrete and the continuum results are in good agreement. Both discrete and continuum solutions predict that for larger normalized hole sizes, the strain level drops to the far-field level at a smaller normalized distance from the hole edge than for small holes. To quantify this, we plot the discrete results for $\varepsilon_{11}/\varepsilon_{appl}$ at $\theta = \pi/2$ and $x_2/r_0 = 1.75$ and compare them with the analytical solutions for both the strain divergence and couple stress solutions in Fig. 5.10. Both the strain divergence and couple stress theories are in reasonable agreement with the discrete solutions; the

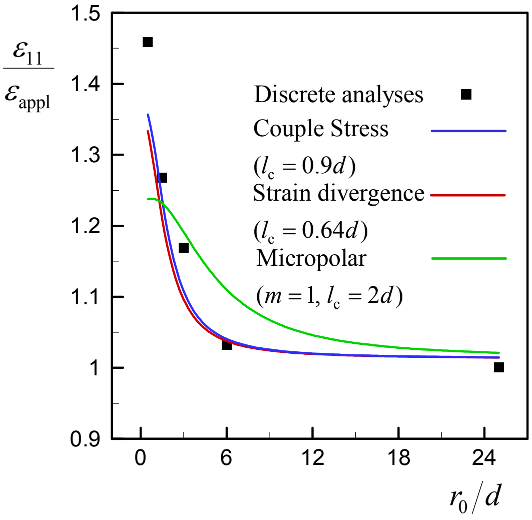

Figure 5.10: The best fits of the strain divergence, couple stress and micropolar (with a small coupling factor $m = 1$) theories to the change in the normalized strain $\varepsilon_{11}/\varepsilon_{appl}$ (at $\theta = \pi/2$ and $x_2/r_0 = 1.75$) with increasing hole radius r_0/d for the discrete calculations.

strain $\varepsilon_{11}/\varepsilon_{\mathrm{appl}}$ decreases with increasing r_0, whereas the classical theory would predict a size-independent response. We also briefly explored micropolar solutions with a small coupling factor m. Figure 5.10 shows the best fit for $m = 1$, which occurs for a characteristic length $l_c = 2d$; it is not able to capture the large gradient in $\varepsilon_{11}/\varepsilon_{\mathrm{appl}}$ with increasing hole size.

5.5 Summary and discussion

In this chapter, we analysed the higher-order effects on the strain distribution around a circular cylindrical hole in a field of uniaxial tension. First, we investigated the differences in the analytical solutions for the strain divergence, couple stress and classical continuum theories. Then we performed finite element calculations on Voronoi samples with different hole sizes and used a strain mapping procedure to extract the strain field around the hole. Finally, we compared the discrete results with the analytical solutions.

The grid size in the strain mapping procedure needed to obtain accurate strain fields scales with the hole size. As a result, the grid size becomes smaller than the cell size for small holes. A direct consequence of this is that many more samples are needed to obtain smooth average fields in the region near the hole. Nevertheless, except for a region very close to the traction free hole boundary where discrete effects prevail, we have been able to obtain a good convergence for each r_0. The discrete results have been found to compare equally well with the strain divergence as the couple stress theory.

Our results agree with the experiments of Dillard *et al.* [2006], in the sense that the strain concentration around a hole reduces for hole sizes comparable to the cell size. In the experiments, Dillard and co-workers used the same strain mapping parameters for their strain mapping procedure for both large and small holes, which, as they also state, might have masked possible strain concentrations in the case of small holes. Nevertheless, they observed that the final crack leading to the fracture of the samples initiated at the hole for large hole radii (for which they captured a clear strain concentration), whereas this was not the case for samples with a small hole radius (for which they could not detect any strain concentration).

Appendix: Hole problem for the strain gradient theory

Mindlin [1964] has shown that any solution of Equation (5.1) can be written in terms of a vector function $\boldsymbol{B}$ and a scalar function B_0 as

$$\boldsymbol{u} = \boldsymbol{B} - l_2^2 \nabla\nabla\bullet\boldsymbol{B} - \frac{1}{2}(\delta - l_1^2\nabla^2)\nabla[\boldsymbol{r}\bullet(1 - l_2^2\nabla^2)\boldsymbol{B} + B_0] = 0, \tag{A1}$$

with

$$\delta = (\lambda + \mu)/(\lambda + 2\mu), \tag{A2}$$

where $\boldsymbol{r}$ is the position vector, and $\boldsymbol{B}$ and B_0 are the solutions of

$$(1 - l_2^2\nabla^2)\nabla^2\,\boldsymbol{B} = 0 \;\text{ and }\; (1 - l_1^2\nabla^2)\nabla^2 B_0 = 0, \tag{A3}$$

respectively, with ∇^2 the Laplacian operator defined in cylindrical coordinates (r,θ,z) as

$$\begin{gathered}\nabla^2 f = f_{,rr} + \frac{1}{r}f_{,r} + \frac{1}{r^2}f_{,\theta\theta} + f_{,zz}, \\ \nabla^2\,\boldsymbol{v} = \begin{bmatrix} v_{r,rr} + \frac{1}{r^2}v_{r,\theta\theta} + v_{r,zz} + \frac{1}{r}v_{r,r} - \frac{2}{r^2}v_{\theta,\theta} - \frac{1}{r^2}v_r \\ v_{\theta,rr} + \frac{1}{r^2}v_{\theta,\theta\theta} + v_{\theta,zz} + \frac{1}{r}v_{\theta,r} + \frac{2}{r^2}v_{r,\theta} - \frac{1}{r^2}v_\theta \\ v_{z,rr} + \frac{1}{r^2}v_{z,\theta\theta} + v_{z,zz} + \frac{1}{r}v_{z,r} \end{bmatrix},\end{gathered} \tag{A4}$$

for a scalar function f and a vector function $\boldsymbol{v}$, respectively.

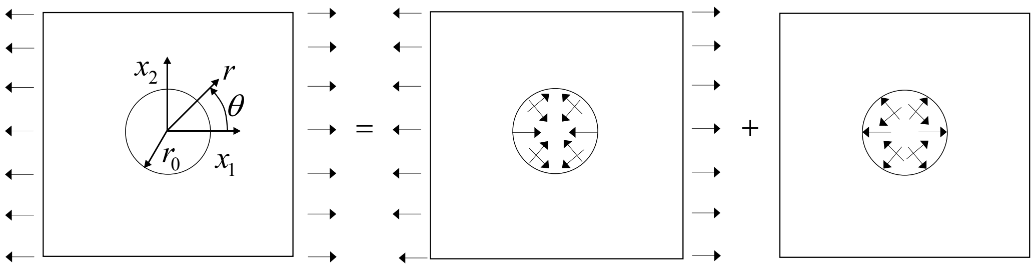

(a) (b) (c)

Figure A1: The hole problem (a) can be written as the superposition of two simpler ones: A uniaxial tension problem of the same block, but without a hole (b) and a problem where compressive tractions are applied only around the hole (c).

Figure A.1a shows the boundary conditions corresponding to the hole problem. We can write this problem as the superposition of two simpler ones: I-) A uniaxial tension problem of the same block, but without a hole (see Fig. A.1b). II-) A problem where compressive tractions are applied only around the hole (see Fig. A.1c). Note that in Fig. A.1b the uniaxial tensile tractions around the hole ensure the uniform strain/stress distribution throughout the block. We know the analytical solution for the first sub-problem; therefore we only have to solve the second sub-problem, shown in Fig. A.1c.

Eshel and Rosenfeld [1970] showed that the solution of Equations (A1-A3) can be given as

$$\begin{aligned} u_r = {} & \frac{1}{2}A_1 r_0^2 r^{-1} - \frac{1}{2}A_3 \delta r_0^2 r^{-1} - \frac{1}{2}A_5(1-\delta) r_0^2 l_1^{-1} K_1(\rho_1) \\ & + \{A_1 r_0^2[\frac{1}{2}r^{-1} + 2(l_1^2 - l_2^2) r^{-3}] - A_2 r_0 l_2 r^{-1} K_2(\rho_2) \\ & + A_4 \delta r_0^4 r^{-3} - A_6(1-\delta) r_0^2[r^{-1}K_2(\rho_1) + \frac{1}{2} l_1^{-1} K_1(\rho_1)]\}\cos(2\theta), \end{aligned} \tag{A5}$$

$$\begin{aligned} u_\theta = {} & \{A_1 r_0^2[-\frac{1}{2}(1-\delta) r^{-1} + 2(l_1^2 - l_2^2) r^{-3}] - A_2 r_0^2[l_2 r^{-1} K_2(\rho_2) \\ & + \frac{1}{2}K_1(\rho_2)] + A_4 \delta r_0^4 r^{-3} - A_6(1-\delta) r_0^2 r^{-1} K_2(\rho_1)\}\sin(2\theta), \end{aligned} \tag{A6}$$

where $\rho_1 = r/l_1$, $\rho_2 = r/l_2$, $K_i()(i=1,\ 2)$ are the modified Bessel functions of the second kind of order i and A_j $(j=0, 1, \ldots, 6)$ are dimensionless constants. Inserting (A5) and (A6) in to the boundary conditions for Fig. A.1c,

$$\begin{aligned} & t_r = \frac{1}{2}T[1+\cos(2\theta)],\ t_\theta = -\frac{1}{2}T\sin(2\theta), \\ & r_r = r_\theta = 0, \end{aligned} \tag{A7}$$

on $r = r_0$, and

$$t_r = t_\theta = r_r = r_\theta = 0, \tag{A8}$$

on $r \to \infty$, via the kinematic and constitutive relations (Equations (1.13) and (1.15)), yields a system of six linear algebraic equations:

$$\begin{aligned} & b_{11}B_1 + b_{13}B_3 + b_{15}B_5 = 0, \\ & b_{21}B_1 + b_{22}B_2 + b_{24}B_4 + b_{26}B_6 = 0, \end{aligned}$$

$$
\begin{aligned}
&b_{31}B_1 + b_{32}B_2 + b_{36}B_6 = -1,\\
&b_{41}B_1 + b_{43}B_3 + b_{45}B_5 = -\frac{1}{2},\\
&b_{51}B_1 + b_{54}B_4 + b_{56}B_6 = -\frac{3}{2},\\
&b_{61}B_1 + b_{62}B_2 + b_{66}B_6 = 1,
\end{aligned}
\tag{A9}
$$

with $B_j = A_j\mu/T$ ($j = 0, 1, \ldots, 6$) and[2]

$$
\begin{aligned}
&b_{11} = \beta_1,\ \ b_{13} = -\delta\beta_1,\ \ b_{15} = (\delta-1)\left[\frac{1}{2}\beta_1 p_1{}^2 K_2(p_1) + \frac{1}{4}p_1{}^3 K_1(p_1)\right],\\
&b_{21} = 1 - 2\delta + \beta_1\left(4\delta \oplus \frac{48}{p_1{}^2} - \frac{48}{p_2{}^2}\right) + \beta_2,\\
&b_{22} = -6\beta_1 K_3(p_2) - \left(\frac{1}{2} + \beta_1 - \frac{1}{2}\beta_2\right)p_2 K_2(p_2),\ \ b_{24} = 24\delta\beta_1,\\
&b_{26} = (\delta-1)\left[6\beta_1 p_1 K_3(p_1) + (1+\beta_1)p_1{}^2 K_2(p_1) + \frac{1}{2}p_1{}^3 K_1(p_1)\right],\\
&b_{31} = \frac{2\delta - 2\beta_2(2-\delta)}{p_1{}^2} - \frac{4(1-\delta)}{p_2{}^2} - \delta,\\
&b_{32} = \left(\frac{1-\beta_2}{p_1{}^2} - \frac{2(1-\delta)}{p_2{}^2}\right)p_2 K_2(p_2) + \delta K_1(p_2),\\
&b_{36} = (1-\delta)(1+\beta_2)K_2(p_1),\ \ b_{41} = -1,\ \ b_{43} = \delta,\\
&b_{45} = -\delta p_1 K_1(p_1),\ \ b_{51} = -\frac{6}{k_1{}^2}(1+\beta_2) - 3\delta,\ \ b_{54} = -6\delta,\\
&b_{56} = (3 + 3\beta_2 - 6\delta)K_2(p_1),\ \ b_{61} = \delta,\ \ b_{62} = -K_1(p_2),\\
&b_{66} = (1-\delta)p_1 K_1(p_1),
\end{aligned}
\tag{A10}
$$

with β_1, β_2, p_1 and p_2 defined in Equation (5.3). By solving for $B_1 \ldots, B_6$ the solution for the problem in Fig. A.1c is complete. The strain distribution can easily be obtained by adding the displacements of the two problems using the kinematic relations.

---

[2] Note that the encircled plus sign in the second line of Equation (A10) is missing in the solution of Eshel and Rosenfeld [1970]; we repeated the analysis and showed that it was a typographical error.

6 Discussion

In this chapter, we discuss our overall results and connect them to the goal of this thesis. We distinguish stiffening and weakening size effects in cellular solids and comment on the predictive power of the generalized continuum theories that we analyzed. Finally, we conclude the thesis by addressing the limitations of the generalized continuum theories and give recommendations for improvement.

In the introduction of this thesis, we stated our goal as follows:
1) To explore the physical mechanisms that are responsible for the size-dependent elastic behaviour of cellular solids by using a discrete microstructural model.
2) To assess the capability of generalized continuum theories to capture size effects through a careful comparison with the discrete simulations.

To establish these goals, we first reviewed the deformation mechanisms of regular and irregular two-dimensional cellular solids in chapter 2. We performed simple shear, uniaxial compression and pure bending tests on discrete samples with the regular and irregular microstructures. For all of the microstructures tested, we detected two kinds of size effects: i) The macroscopic shear stiffness increases with decreasing sample size. ii) The macroscopic (uniaxial) compressive and bending stiffness decrease with decreasing sample size. The first, stiffening under simple shear, is associated with the strong boundary layers that form adjacent to the top and bottom boundaries, to which the cell walls are perfectly bonded. The smaller the sample size, the larger the area fraction of the strong boundary layers and thus the macroscopic shear stiffness. The second kind of size effect, weakening in the compressive and bending stiffness, on the other hand, is a result of weak boundary layers that form adjacent to the traction free edges, where the cells are much more compliant compared to the bulk.

Stiffness can be defined as the resistance of an elastic body to deformation by an applied traction. In the classical continuum theory, three displacement degrees of freedom are used to quantify the change in the position of a material point and deformation is expressed in terms of the symmetric part of the displacement gradients. For most (i.e. dense) materials, classical continuum theory suffices to accurately describe the elastic deformation, since most sample sizes and loading wavelengths are much larger than the characteristic material length scales (e.g. atoms, grains). However, in cellular solids, where the cell size sets the material length, this no longer holds. Consequently, higher-order deformation modes (whose effect was negligible in dense materials) become important at the macroscopic scale and should be accounted for. The generalized continuum theories studied here use additional degrees of freedom and/or additional deformation modes to add higher-order terms to the internal strain energy density. If in a boundary value problem these higher order terms are triggered, the overall response will be stiffer compared to the classical theory. The simple shear problem is such a case, where gradients in shear strain (or rotation) develop near the sample edges resulting in strong boundary layers and an overall stiffening compared to classical theory. The size effects of the second kind, or free edge effects leading to weakening, are different in character from the first kind. They are not associated with an additional deformation mode that is absent in the classical continuum theory, but arise due to the fact that near the traction free edges the cells cannot transfer the forces as efficient as in the core, resulting in a layer of reduced material stiffness. The generalized continuum theories mentioned in this thesis (see Table 1.1) cannot capture these free edge effects.

In chapter 3 we analyzed the micropolar theory, featuring extra degrees of freedom, the microrotations, and the associated higher-order deformations, the microrotation gradients. We derived the analytical solutions of the simple shear and pure bending problems. By comparing the discrete and analytical results for the simple shear problem in terms of the macroscopic shear stiffness, we fitted the coupling factor m and the characteristic length l_c. It turned out that for the best fit, the microrotations should be constrained to be equal to the macrorotations ($m \rightarrow \infty$), so that the micropolar theory reduces to the couple stress theory, featuring one additional material parameter, l_c, that was found to be on the order of the cell size for the microstructures analyzed. The corresponding local response, i.e. the macrorotation and shear strain fields through the thickness of the samples, was found to be in excellent agreement with the discrete fields. For the pure bending problem, however, the analytical solution predicted an increasing bending stiffness with decreasing sample thickness, which is opposite to the weakening observed for the discrete analyses. The reason for this is that rotation gradients develop in both the simple shear problem and the pure bending problem. In the simple shear problem, due to the symmetries, the rotation gradients through the thickness account for the gradient in shear strain, which is responsible for the extra energy consumed. Thus, only the rotation gradients in shear trigger a higher-order response in cellular solids, while the rotation gradients in bending do not. In the well-known Euler-Bernoulli beam theory, the normal stress gradients through the thickness are replaced by a bending moment and its constitutive relation to the rotation gradient (curvature). In micropolar theory, however, both the (classical) stress gradients and (higher order) bending moments are present, resulting in double counting in case of bending of small samples.

Another way of extending the classical continuum theory is to associate energy not only to strain, but also to its gradients (see Table 1.1). Among these higher-grade theories, Toupin-Mindlin's strain gradient theory is most often encountered in the literature. It has inspired many scientists to develop higher-grade theories to capture size effects in the mechanical behaviour, both for elasticity (e.g. Lam *et al.* [2003]) and for plasticity (e.g. Aifantis [1987], Fleck and Hutchinson [1993, 1997, 2001]). Toupin-Mindlin's strain gradient theory, however, is based on third order tensors (the strain gradients and the conjugate double stresses) and requires five additional material constants to be defined for linear elastic, centro-symmetric isotropic materials. Therefore, to give a complete and unique experimental delineation of strain gradient behaviour is a formidable task. A better strategy is to take into account only that part of the strain gradient that actually coincides with the extra deformation measure(s) related to the observed size effects. For this purpose, we developed a continuum theory that assigns energy to the divergence of strain, which coincides with the shear strain gradient in the case of the simple shear problem. This theory is based on vectors (the strain divergence and conjugate higher-order stress) and consequently requires only one additional constant for isotropic materials. We showed that this strain divergence theory is able to capture the stiffening under simple shear with decreasing sample size as accurate as the couple stress theory (in fact, both solutions coincide, see chapter 4). For the case of pure bending, however, as a result of satisfying both the classical and additional higher-order boundary conditions, the transverse strains (ε_{22} in chapter 4) turn out to be non-linear, in contrast to the classical solution, and this results in an increasing bending stiffness with decreasing specimen thickness.

We also briefly explored the role of the five constants of the full strain gradient theory in the shear and bending problems. The analytical solution for the simple shear problem for the full strain gradient theory (see e.g. Kouznetsova [2002]) can be shown to depend only on the second characteristic length, $l_2 = (a_3 + 2a_4 + a_5)/2\mu$. At least one of the constants a_3, a_4, a_5 should be non-zero to exactly capture the shear stiffening. When a_5 is the only non-zero constant, however, the non-negativeness of the strain energy density is not satisfied. When a_3 is the only non-zero constant, the strain gradient theory falls back to the strain divergence theory. When a_4 is the only non-zero constant, we can choose it to be equal to l_c^{SD}/μ to ensure an excellent fit to the discrete results in shear (see chapter 4). However, by substituting this in the pure bending solution for the strain gradient theory (see the Appendix of chapter 4) it follows that the stiffening is larger compared to the strain divergence solution, both for isotropic and transverse isotropic solids.

Finally, in chapter 5 we analyzed the effects of a circular cylindrical hole in a field of uniaxial tension on the strain distribution. It was observed that the discrete strain fields remain largely unaffected for hole radii larger than approximately three cell sizes. For smaller hole radii the strain gradients around the hole considerably reduce. By comparing the discrete results with the couple stress and strain divergence solutions, it followed that they are both able to capture the effect of the hole size, except for a region very close to the hole boundary, where discrete effects prefail. Outside this regime the discrete strain distribution is successfully captured by these two theories, whereas micropolar continuum theory with a small coupling factor *m* is shown to be less accurate.

Table 6.1 summarizes the performance of the generalized continuum theories analyzed in this thesis. The micropolar theory with a small coupling factor *m* is not able to accurately capture the size-dependent response in simple shear and for the hole problem, whereas the couple stress and strain divergence theories perform much better and equally well. It should be emphasized that in the (planar) problems analyzed here, both theories feature only one additional higher-order constant (the characteristic length l_c). By fitting this constant to the overall discrete response in shear, it is shown that the discrete strain fields in shear and around the hole can be well captured by these theories. For uniaxial loading the discrete calculations predict a size-independent response when free-edge effects are disregarded, while also in a state of pure bending no higher-order modes are triggered in the cellular structures. The continuum theories (obviously) show a size-independent response under uniaxial loading, due to the absence of gradients. For pure bending, however, stiffening is predicted with decreasing sample size for all theories, in contrast to the discrete calculations. Note that the discrete structures analyzed here have an in-plane Poisson's ratio $\nu_p = 0.94$, close to the limit of incompressibility, for which the couple stress and strain divergence theories are almost identical for all the boundary value problems analyzed. Real metal foams, however, are isotropic with a much lower Poisson's ratio, around $\nu \approx 0.3$ (see Ashby *et al*. [2000]). For such low Poisson's ratios, the two solutions for the hole problem are very different, while stiffening under pure bending is negligible for the strain divergence theory, whereas it increases even more for the couple stress theory.

Table 6.1
The performance of the generalized continuum theories analyzed in this thesis.

	Micropolar theory (with a small *m*)	Couple stress theory	Strain divergence theory
Simple shear	–	+	+
Hole problem	–	+	+
Uniaxial loading	+	+	+
Pure bending	–	–	–

The best one can expect from the generalized continuum theories studied in this thesis is to give a size-independent response for cases in which weakening size effects originate due to traction free edges. To capture weakening in a continuum setting, several routes can be followed. Brezny and Green [1990] accounted for weakening in bending by using a composite model with boundary layers having a lover stiffness than the bulk (see also Andrews *et al*. [2001]). Lakes [1995] used a non-local continuum theory which takes into account long range interactions of material points. Finally, one could use a generalized continuum theory that can account for the presence of surface stresses (see e.g. Gurtin and Murdoch [1975]). This theory has been successfully applied to predict weakening size effects in tension and bending of single crystals at the nanoscale (see e.g. Miller and Shenoy [2000]).

References

Adachi, T., Tomita, Y. and Tanaka, M. [1998], "*Computational simulation of deformation behaviour of 2D-lattice continuum*", Int. J. Mech. Sci. 40, 857-866.

Aero, E. L. and Kuvshinskii, E. V. [1961], "*Fundemental equations of the theory of elastic media with rotationally interacting particles*", Soviet Physics Solid State 2, 1272-1281.

Aifantis, E. [1987], "*The physics of plastic deformation*", Int. J. Plasticity 3, 211-248.

Anderson, W. B. and Lakes, R. S. [1994], "*Size effects due to Cosserat elasticity and surface damage in closed-cell polymethacrylimide foam*", J. Mat. Sci 29, 6413-6419.

Anderson, W. B., Chen, C. P. and Lakes, R. S. [1994], "*Experimental study of size effects and surface damage of polymethacrylimide closed-cell foam*", Cellular Polymers 13, 1-15.

Andrews, E., Sanders, W, Gibson, L.J [1999], "*Compressive and tensile behaviour of aluminum foams*", Mater. Sci. Eng. A 270, 113-124.

Andrews, E.W., Gioux, G., Onck, P., Gibson, L.J [2001], "*Size effects in ductile cellular solids. II. Experimental results*", Int. J. Mech. Sci. 43, 701-713.

Antoniou, A., Onck, P. R. and Bastawros, A. F. [2004], "*Experimental analysis of compressive notch strengthening in closed-cell aluminum alloy foam*", Acta Mater. 52, 2377-2386.

Ashby, M. F., Evans, A., Fleck, A. N., Gibson, L. J., Hutchinson, J. W., Wadley, H. N. G.[2000], " *Metal Foams: A Design Guide*", Butterworth-Heinemann, Oxford.

Aşkar, A., and Çakmak, A. S. [1968], "*A structural model of a micropolar continuum*", Int. J. Engrg. Sci. 6, 583-589.

Banks, C. B. and Sokolowski, M. [1968], "*On certain two-dimensional applications of the couple stress theory*", Int. J. Solids Structures 4, 15-29.

Bart-Smith, H., Bastawros, A. F., Mumm, D. R., Evans, A. G., Sypeck, D. J., Wadley, H. N. G. [1998], "*Compressive deformation and yielding mechanisms in cellular A1 alloys determined using X-ray tomography and surface strain mapping*", Acta Mater. 46, 3583-3592.

Bastawros, A. F., Bart-Smith, H., Evans, A.G. [1999], "*Experimental analysis of deformation mechanisms in a closed cell aluminium foam*", J. Mech. Phys. Solids 48, 301-322.

Bazant, Z. P. and Christensen, M. [1972], "*Analogy between micropolar continuum and grid frameworks under initial stress*", Int. J. Solids Structures 8, 327-346.

Brezny, R. and Green, D. J. [1990], "*Characterization of edge effects in cellular materials*", J. Mat. Sci. 25, 4571-4578.

Chen, C. and Fleck, N. A. [2002], "*Size effects in the constrained deformation of metallic foams*", J. Mech. Phys. Solids 50, 955-977.

Chen, C., Lu, T. J., Fleck, N. A. [1999], "*Effect of imperfections on the yielding of two-dimensional foams*", J. Mech. Phys. Solids 47, 2235-2272.

Chen, J.Y., Huang, Y., Ortiz, M. [1998], "*Fracture analysis of cellular materials: a strain gradient model*", J. Mech. Phys. Solids 46, 789-828.

Christensen, R. M. [1995], "*The hierarchy of microstructures for low density materials*", Z. Angew. Math. Phys. 46, 506-521.

Cosserat, E. and Cosserat, F. [1909], "*Theorie des Corps Deformables*", Hermann, Paris

De Boor, R [1998], "*Theory of porous media – Past and present*", Z. Angew. Math. Mech. 78, 441-446.

Delaunay, B. [1934], "*Sur la sphère vide*", Izvestia Akademii Nauk SSSR, Otdelenie Matematicheskikh i Estestvennykh Nauk 7, 793-800.

Dendievel, R., Forest, S., Canova, G. [1998], "*An estimation of overall properties of heterogeneous Cosserat materials*", J. Phys. IV (Proceedings) 8, 111-118.

Deshpande, V. S. and Fleck, N. A. [2000], "*Isotropic constitutive models for metallic foams*", J. Mech. Phys. Solids 48, 1253-1283.

Deshpande, V. S., Ashby, M. F. and Fleck, N. A. [2001a], "*Foam topology bending versus stretching dominated architectures*", Acta Mater. 49, 1035-1040.

Deshpande, V. S., Ashby, M. F. and Fleck, N. A. [2001b], "*Effective properties of the octet-truss lattice material*", J. Mech. Phys. Solids 49, 1747-1769.

Diebels, S. and Steeb, H. [2002], "*The size effect in foams and its theoretical and numerical investigation*", Proc. R. Soc. Lond. A 458, 2869-2883.

Dillard, T., Forest, S., Ienny, P. [2006] "*Micromorphic continuum modelling of deformation and fracture behaviour of nickel foams*", Eur. J. Mech. A/Solids 25, 526-549.

Doyoyo, M and Wierzbicki, T [2003], "E*xperimental studies on the yield behaviour of ductile and brittle aluminum foams*", Int. J. Plasticity 19, 1195-1214.

Ellis, R. W. and Smith, C. W. [1967], "*A thin plate analysis and experimental evaluation of couple stress effects*", Exp. Mech. 7, 372-380.

Engel, G., Garikipati, K., Hughes, T. J. R., Larson, M. G., Mazzei, L., Taylor, R. L. [2002], "*Continuous/discontinuous finite element approximations of fourth-order elliptic problems in structural and continuum mechanics with applications to thin beams and plates, and strain gradient elasticity*", Comput. Methods Appl. Mech. Engrg. 191, 3669-3750.

Eringen, A. C. [1962], "*Nonlinear theory of continuous media*", McGraw-Hill, New York.

Eringen, A. C. [1965], "*Theory of micropolar elasticity*", Proc. 9'th Midwestern Mech. Conf., 23-40.

Eringen, A. C. [1966], "*Linear theory of micropolar elasticity*", J. Math. Mech. 15, 909-923.

Eringen, A. C. [1968], “*Theory of micropolar elasticity*”, in: “*Fracture: An advanced treatise*”, Vol. II: Mathematical fundamentals, Ed.: Liebowitz, H., Academic Press, New York and London.

Eringen, A. C. [1971], “*Micropolar elastic solids with stretch*”, in: “*Prof Dr. Mustafa Inan Anisina*”, Ari Kitabevi Matbaasi, Istanbul.

Eringen, A. C. [1990], “*Theory of thermo microstretch elastic solids*”, Int. J. Engng. Sci. 28, 1291-1301.

Eringen, A. C. [1999], “*Microcontinuum Field Theories I: Foundations and Solids*”. Springer-Verlag, New York.

Eringen, A. C. and Şuhubi, E. S. [1964], “*Nonlinear theory of simple micro-elastic solids*” Int. J. Engng. Sci. 2, 189-203.

Eshel, N. N. and Rosenfeld, G. [1970], “*Effects of strain-gradient on the stress concentration at a cylindrical hole in a field of uniaxial tension*”, J. Eng. Math. 4, 97-111.

Fazekas, A., Dendievel, R., Salvo, L., Brechet, Y. [2002], “*Effect of microstructural topology upon the stiffness and strength of 2D cellular structures*”, Int. J. Mech. Sci. 44, 2047-2066.

Fleck, N. A. and Hutchinson, J. W. [1993], “*A phenomenological theory for strain gradient effects in plasticity*”, J. Mech. Phys. Solids 41, 1825-1857.

Fleck, N. A. and Hutchinson, J. W. [1997], “*Strain gradient plasticity*”, Adv. Appl. Mech. 33, 295-361.

Fleck, N. A. and Hutchinson, J. W. [2001], “*A reformulation of strain gradient plasticity*”, J. Mech. Phys. Solids 49, 2245-2271.

Fleck, N. A., Olurin, O. B., Chen, C., Ashby, M. F. [2001], “*The effect of hole size upon the strength of metallic and polymeric foams*”, J. Mech. Phys. Solids 49, 2015-2030.

Forest, S. and Sievert, R. [2006], “*Nonlinear microstrain theories*”, Int. J. Solids Structures, in press.

Gauthier, R. D. [1982], "*Experimental investigation on micropolar media*," in: *Mechanics of Micropolar Media*", Ed.: Brulin, O. and Hsieh, R.K.T (CISM Lecture Notes) World Scientific, Singapore.

Gauthier, R. D. and Jahsman, W. E. [1975], "*A quest for micropolar elastic constants*", J. Appl. Mech. 42, 369-374.

Gibson, L. G. and Ashby, M. F. [1997], "*Cellular solids: structure and properties*", 2'nd edition, Cambridge University Press, Cambridge.

Gibson, L. J., Ashby, M. F., Schajer, G. S., Robertson, C. I. [1982], "*The mechanics of two-dimensional cellular solids*", Proc. R. Soc. Lond. A 382, 25-42

Gioux, G., McCormack, T. M., Gibson, L. J. [2000], "*Failure of aliminum foams under multiaxial loads*", Int. J. Mech. Sci. 42, 1097-1117.

Green, A. E. and Rivlin, R. S. [1964], "*Simple force and stress multipoles*", Arch. Rat. Mech. Anal. 16, 325-353.

Grenestedt, J. L. [1997], "*Effective yield behavior of some models for 'perfect' cellular solids*", CUED Report, Cambridge University, Cambridge.

Grenestedt, J.L. [1998], "*Influence of wavy Imperfections in cell walls on elastic stiffness of cellular solids*", J. Mech. Phys. Solids 46, 29-50

Grenestedt, J. L. [1999], "*Effective elastic behavior of some models for 'perfect' cellular solids*", Int. J. Solids Structures 36, 1471-1501.

Grioli, G. [1960], "*Elasticita asimmetrica*", Ann. di. Mat. Pura ed appl., Ser. IV 50, 389-417.

Gurtin, M. E. and Murdoch, A. [1975], "*A continuum theory of elastic material surfaces*", Arch. Rat. Mech. Anal. 57, 291-323.

Hartranft, R. J. and Sih, G. C. [1965], "*The effect of couple-stresses on the stress concentration of a circular inclusion*", J. Appl. Mech. 32, 429-431.

Hibbitt, Karlsson and Sorensen [2001], "*Abaqus standard user manual*", U.S.A.

Kesler, O and Gibson, L. J. [2002], "*Size effects in the metallic foam core sandwich beams*", Mat. Sci. Eng. A326, 228-234.

Koiter, W. T. [1964], "*Couple stress in the theory of elasticity* I, II", Proc. Kon. Nederl. Akad. Wetensch. B 67, 17-44.

Kouznetsova, V. G. [2002], "*Computational homogenization for the multi-scale analysis of multi-phase materials*", PhD Thesis, Technische Universiteit Eindhoven, Eindhoven.

Lakes, R. S. [1983], "*Size effects and micromechanics of a porous solid*", J. Mat. Sci. 18, 2572-2580.

Lakes, R. S. [1985] "*A pathological situation in micropolar elasticity*", J. Appl. Mech. 52, 234-235.

Lakes, R. S. [1986], "*Experimental microelasticity of two porous solids*", Int. J. Solids Structures 22, 55-63.

Lakes, R. S. [1995], "*Experimental methods for study of Cosserat elastic solids and other generalized elastic continua*", in: "*Continuum models for materials with micro-structure*", Ed.: Mühlhaus, H., J. Wiley, New York.

Lam, D. C. C., Yang, F., Chong, A. C. M., Wang, J., Tong, P. [2003], "*Experiments and theory in strain gradient elasticity*", J. Mech. Phys. Solids 51, 1477-1508.

Malvern, L. E. [1969], "*Introduction to the mechanics of a continuous medium*", Prentice-Hall: Upper Saddle River, NJ, USA.

Miller, R. E. and Shenoy V. B. [2000], "*Size-dependent elastic properties of nanosized structural elements*", Nanotechnology 11, 139-147.

Mindlin, R.D. [1963], "*Influence of couple stress on stress concentrations*", Experimental Mechanics 3, 1-7.

Mindlin, R.D. [1964], "*Microstructure in linear elasticity*", Arch. Rat. Mech. Anal. 16, 51-78.

Mindlin, R.D. [1965], "*Second gradient of strain and surface tension in linear elasticity*", Int. J. Solids Structures 1, 417-438.

Mindlin, R.D. and Eshel, N. N. [1968], "*On first strain-gradient theories in linear elasticity*" Int. J. Solids Structures 4,109-124.

Mindlin, R.D. and Tiersten, H. F. [1962], "*Effects of couple stresses in linear elasticity*", Arch. Rat. Mech. Anal. 11, 415-448.

Mora, R. and Waas, A. M. [2000], "*Measurement of the Cosserat constant of circular-cell polycarbonate foam*", Phil. Mag. A 80, 1699-1713.

Nowacki, W. [1986], "*Theory of Asymmetric Elasticity*", Pergamon Press,Oxford.

Onck, P. R. [2002], "*Cosserat modeling of cellular solids*", C. R. Mechanique 330, 717-722.

Onck, P. R., Andrews, E., Gibson, L.J [2001], "*Size effects in ductile cellular solids. Part I: modeling*", Int. J. Mech. Sci. 43, 681-699.

Ostoja-Starzewski, M., Sheng, P. Y., Alzebdeh, K. [1996], "*Spring network models in elasticity and fracture of composites and polycrystals*", Computational Materials Science 7, 82-93.

Padovani, C. [2002], "*Strong ellipticity of transversely isotropic elasticity tensors*", Meccanica 37, 515-525.

Paul, A., Seshacharyulu, T., Ramamurty, U. [1999], "*Tensile strength of a closed-cell Al foam in the presence of notches and holes*", Scripta Mater. 40, 808-814.

Pradel, F. and Sab, K. [1998], "*Cosserat modelling of elastic periodic lattice structures*", C. R. Acad. Sci., Serie II B, 326, 699-704.

Rajagopal, E. S. [1960], "*The existence of interracial couples in infinitesimal elasticity*", Ann. der Physik 6, 192-201.

Schijve, J. [1966], "*Note on couple stresses*", J. Mech. Phys. Solids 14, 113-120.

Shu, J. Y., King, W. E. and Fleck, N. A. [1999], "*Finite elements for materials with strain gradient effects*", Int. J. Numer. Meth. Engng. 44, 373-391.

Silva, M. J., Wilson, C. H. and Gibson, L. J. [1995], "*The effects of non-periodic microstructure on the elastic properties of two-dimensional cellular solids*", Int. J. Mech. Sci. 37, 1161-1177.

Simone, A. E. and Gibson, L. J. [1998a], "*Effects of solid distribution on the stiffness and strength of metallic foams*", Acta Mater. 46, 2139-2150.

Simone, A. E. and Gibson, L. J. [1998b], "*Aluminum foams produced by liquid-state processes*", Acta Mater. 46, 3109-3123.

Sugimura, Y., Meyer, J., He, M. Y., Bart-Smith, H., Grenestedt, J. and Evans, A. G. [1997], "*On the mechanical performance of closed cell Al alloy foams*", Acta Mater. 45, 5245-5259.

Tekoğlu, C. and Onck, P. R. [2003a], "*A comparison of discrete and Cosserat continuum analyses for cellular materials*", Proc. Int. Conf. Cellular Metals and Metal Foaming Technology, 23rd -25th June 2003, Ed.: J. Banhart, N. A. Fleck, A. Mortensen, Verl. MIT Publ., Berlin.

Tekoğlu, C. and Onck, P. R. [2003b], "*Identification of Cosserat constant for cellular materials*", Proc. 9th Int. Conf. Mechanical Behaviour of Materials (ICM9), Geneva, Switzerland [CD_ROM].

Tekoğlu, C. and Onck, P. R.[2005], "*Size effects in the mechanical behavior of cellular materials*", J. Mat. Sci. 40, 5911-5917.

Timoshenko, S. P. and Goodier, J. N. [1970], "*Theory of elasticity*", 3'rd edition, McGraw-Hill, New York.

Toupin, R. A. [1962], "*Elastic materials with couple-stresses*", Arch. Rat. Mech. Anal. 11, 385-414.

Toupin, R. A. [1964], "*Theories of elasticity with couple-stress*", Arch. Rat. Mech. Anal. 17, 85-112.

Triantafyllidis, N. and Schraad, W. [1998], "*Onset of failure in aluminum honeycombs under general in-plane loading*", J. Mech. Phys. Solids 46, 1089-1124.

Truesdell, C. A. and Toupin, R. A. [1960], "*The classical field theories*", Encyclopedia of Physics, III/1, Springer, Berlin.

Van der Burg, M. V. D., Shulmeister, V., Van der Giessen, E., Marissen, R. [1997], "*On the linear elastic properties of regular and random open-cell foam models*", J. Cellular Plastics 33, 31-54.

Voronoi, M. G. [1908], "*Nouvelles applications des parametres continus a la theorie des formes quadratiques*", J. Reine Angew. Math. 134,198-287.

Wang, X. and Stronge, W.J. [1999], "*Micropolar theory for two-dimensional stresses in elastic honeycomb*", Proc. R. Soc. Lond. A 455, 2091, 2116.

Warren, W. E. and Byskov, E. [1997], "*Micropolar and nonlocal effects in spatially periodic, two-dimensional structures*", Report R 37, Technical University of Denmark.

Warren, W. E. and Byskov, E. [2002], "*Three-Fold Symmetry Restrictions on Two-. Dimensional Micropolar Materials*", European J. Mech. A/Solids 21, 779–792.

Weitsman, Y. [1965], "*Couple stress effects on stress concentration around a cylindrical inclusion in a field of uniaxial tension*", J. Appl. Mech. 2, 424-428.

Yang, J. F. C. and Lakes, R. S. [1981], "*Transient study of couple stress in compact bone: torsion*", J. Biomech. Eng. 103, 275-279.

Zhang, X. and Sharma, P. [2005], "*Inclusions and inhomogeneities in strain gradient elasticity with couple stresses and related problems*" Int. J. Solids Structures 42, 3833–3851.

Zhu, H. X., Hobdell, J. R. and Windle, A. H [2000], "*Effects of cell irregularity on the elastic properties of open-cell foams*", Acta mater. 48, 4893-4900.

Zhu, H. X., Thorpe, S. M. and Windle, A. H. [2001a], "*The geometrical properties of irregular two-dimensional Voronoi tessellations*", Phil. Mag. A 81, 2765-2783.

Zhu, H. X., Hobdell, J. R., Windle, A. H [2001b], "*Effects of cell irregularity on the elastic properties of 2D Voronoi honeycombs*", J. Mech. Phys. Solids 49, 857-870.

Zienkiewicz, O. C. and Taylor, R. L. [2000], "*The Finite Element Method*" Vol. 1: "*The Basis*", 5'th edition, Butterworth-Heinemann, Oxford.

Acknowledgements

I am most grateful to my supervisor Patrick Onck, for his persistent guidance, patience and encouragement during these years. Thank you Patrick; for always being there for scientific and other problems.

I would also like to thank to Erik van der Giessen for his consistent interest in the project and invaluable remarks he made during our group (micromechanics of materials, Groningen) discussions. Thank you as well, all group members, for a friendly working atmosphere.

I would also like to acknowledge the Reading Committee members, Professors Marc Geers, Fred van Keulen and Samuel Forest for their useful comments.

Last, but definitely not least, I would like to thank to my family and my friends for their love and support.

Cihan Tekoğlu